THE UNIVERSITY
of ADELAIDE

ROBUST ACTUATOR CONTROLLER FOR ACTIVE-TRUSS-BASED MORPHING WING

BY

DIFAN TANG

A THESIS SUBMITTED IN FULFILMENT OF THE REQUIREMENT
FOR THE DEGREE OF MASTER OF ENGINEERING SCIENCE

AT

SCHOOL OF MECHANICAL ENGINEERING
THE UNIVERSITY OF ADELAIDE

NOVEMBER 2012

Contents

Abstract

The active-truss-based morphing wing (ATBMW) is a new type of smart structure, which is more efficient than airfoils with conventional control surfaces. However, the sophisticated ATBMW framework and large numbers of actuators make it difficult to obtain the overall structural dynamics for controller design and inconvenient to tune actuators on board. Our research therefore aims to develop an actuator-level control scheme to simplify the process of controller implementation on ATBMWs so that the above problems regarding controller design and on-board tuning can be bypassed.

The proposed control scheme is based on the concept of unknown-input estimation and compensation in a servomechanism. A new unknown-input estimator (UIE) is developed and integrated with a Linear-Quadratic-Gaussian (LQG) controller to provide enhanced compensation of uncertainties. By doing so, the resultant controller can be designed and tuned simply using the dynamics of the actuator, without the necessity to know the dynamics of the entire wing structure. Existing techniques for estimating unknown inputs to a system require at least one or more of the following: detailed knowledge on unknown inputs, derivatives of measured outputs, inversion of plant dynamics, constrained state observer design, parameter optimisation (global optimum not guaranteed), or complicated designs. The new UIE developed in this thesis is exempted from the aforementioned limitations and features a simple structure and straightforward design.

To validate the proposed UIE-integrated LQG controller, an ATBMW prototype with 5 linear actuators is built. For comparison, a PID controller is introduced in both simulations and experiments. Both types of controllers are designed using two sets of models obtained via system identification: one set represents actuator dynamics only, while the other set includes wing structural dynamics.

In simulation study, system sensitivity and stability robustness are firstly investigated against parameters associated with the UIE component, with guidelines for designing the proposed UIE-integrated LQG controller validated. The mechanism of unknown-input compensation is then demonstrated by dividing unknown inputs into exogenous disturbances and internal uncertainties and examining the two situations separately.

Compared with a standard LQG controller, the UIE-integrated LQG controller shows enhanced capability in rejecting unknown inputs. Lastly, the UIE-integrated LQG controller is implemented on all the 5 actuators in the presence of only internal uncertainties, and compared with the PID controller. Superior performance of the UIE-integrated LQG controller over the PID algorithm is observed in simulations.

In experimental study, wind tunnel tests were conducted to further validate the efficacy of the UIE-integrated LQG controller under both aerodynamic loads and modelling errors. The performance of the UIE-integrated LQG controller designed according to actuator dynamics is closely comparable to that of its congener based on wing structural dynamics, and both outperform the PID controller.

In conclusion, the new UIE is capable of effective estimation of unknown inputs. The UIE-integrated LQG controller has an enhanced capacity to compensate a wide class of unknown inputs including exogenous disturbances and internal uncertainties, and meanwhile the ease of design is maintained. The most significant merit of applying the proposed controller on an ATBMW is that the implementation of actuator controllers is considerably simplified despite the complexity of the ATBMW framework. The controller can be based on actuator dynamics only, and can be tuned on individual actuators before the actuators are assembled on the wing. Therefore, the process of controller implementation is free from structural coupling constraints, and there is no need to obtain wing structural dynamics for controller design and to further tune actuators on board.

Beyond the merits mentioned above, the proposed controller has broader significance in the following two aspects. Firstly, it provides a unified solution to simplifying actuator controller implementation on ATBMWs despite the variations and complexity of ATBMW structures, and is thus significant to successful realisations of a wide range of promising ATBMW concepts; Secondly, the enhanced capacity of disturbance rejection is crucial to aerodynamic improvements achieved by ATBMWs as it ensures reliable performance of wing morphing in the presence of unmeasured and unpredictable exogenous loads.

Declarations

I certify that this work contains no material which has been accepted for the award of any other degree or diploma in any university or other tertiary institution and, to the best of my knowledge and belief, contains no material previously published or written by another person, except where due reference has been made in the text. In addition, I certify that no part of this work will, in the future, be used in a submission for any other degree or diploma in any university or other tertiary institution without the prior approval of the University of Adelaide and where applicable, any partner institution responsible for the joint-award of this degree.

I give consent to this copy of my thesis, when deposited in the University Library, being made available for loan and photocopying, subject to the provisions of the Copyright Act 1968.

I also give permission for the digital version of my thesis to be made available on the web, via the University's digital research repository, the Library catalogue and also through web search engines, unless permission has been granted by the University to restrict access for a period of time.

DIFAN TANG Date

Acknowledgement

I wish to give my sincere gratitude to my supervisors Dr Lei Chen and Associate Professor Eric Hu, for their support, guidance and assistance, from general aspects of project management to specific technical details.

I would also like to thank the staff in the mechanical and electronic workshops at the School of Mechanical Engineering, the University of Adelaide, for building the active-truss-based morphing wing prototype as well as providing handy helps and advice throughout the project. In particular, my thanks go to Dr Michael Riese, Mr Richard Patemen, Mr Silvio De Ieso, and Mr Philip Schmidt.

An additional mention goes to Mr Jing Han NG, Mr Pee Ter SEET, Mr Teng Chern ONG, and Mr Adrian Tat Chuan CHIAM, who contributed to the project in wing prototype detailing. Special appreciation is given to Dr Kristy Hansen, for her advice and help in setting up the wind tunnel.

Last but not least, I wish to acknowledge my great debt to my parents, Mr Canming Tang and Mrs Wen Wen, as well as my wife Wei Wei, for their consistent support and encouragement along my journey of study.

List of Tables

List of Figures

List of Acronyms

ATBMW	active-truss-based morphing wing
DOB	disturbance observer
LQ	linear-quadratic
LQG	Linear-Quadratic-Gaussian
MIMO	Multi-Input Multi-Output
PID	proportional-integral-derivative
PIO	proportional-integral observer
SISO	Single-Input Single-Output
SMA	shape memory alloy
UIDO	unknown-input-decoupled observer
UIE	unknown-input estimator
UIO	unknown-input observer

Nomenclature

Latin Letters	Definition	Unit
a	Average cross section area of a strut	m^2
$\boldsymbol{A}$	System matrix (continuous-time domain)	
a_w	Planform area of an airfoil	m^2
b	Coefficient (general)	
$\boldsymbol{B}$	Input matrix (continuous-time domain)	
c	Coefficient (general)	
$\boldsymbol{C}$	Output matrix (continuous-time domain)	
C_L	Lift coefficient	
d	Unknown/disturbance input (general)	
$\boldsymbol{D}$	Direct transmission term (continuous-time domain)	
d_e	Unknown/disturbance input (equivalent)	
e	Error	
E	Young's modulus	N/m^2
f	Force (in local Cartesian coordinate system)	N
F	Force (in global Cartesian coordinate system)	N
F_L	Lift force	N
g	Order of derivatives	
G	Transfer function (general)	
H	Transfer function (feedback controller)	
i	The i^{th} quantity	
$\boldsymbol{I}$	Identity matrix	
j	Imaginary operator	
J	Performance index	
k	The k^{th} quantity	
K	Controller gain (scalar)	
$\boldsymbol{K}$	Controller gain (matrix)	

Latin Letters	Definition	Unit
l	Length of a strut	m
$\boldsymbol{L}$	State observer gain matrix	
m	Denominator order of a transfer function	
M	Transfer function (un-modelled dynamics)	
n	Number (general)	
N	Filter coefficient (for the derivative term of PID)	
p	Numerator order of a transfer function	
P	Transfer function (actual plant)	
P_n	Transfer function (nominal plant)	
q	Nodal displacement along the axial direction of a strut	m
$\boldsymbol{Q}$	Weighting matrix	
r	Reference input	
R	Weighing scalar	
$\boldsymbol{R}$	Weighing matrix	
s	Complex variable	
S	Sensitivity function	
t	Time (general)	s
$\boldsymbol{T}$	Transformation matrix	
t_s	Sampling interval	s
u	Control input	
U	Nodal displacement (in global Cartesian coordinate system)	m
V	Volume of a strut	m^3
v_a	Air velocity	m/s
w	Process noise	
$\boldsymbol{W}$	General matrix	
x	System state	
y	System output	
z	Variable of z-transform	
$\boldsymbol{Z}$	General matrix	

Greek Letters	Definition	Unit
α	Deviation	
β	Stability robustness index	
γ	General scalar	
$\boldsymbol{\Gamma}$	Stiffness matrix (in global Cartesian coordinate system)	N/m
δ	Impulse function	
Δ	Ratio of tracking deviation	%
ε	Strain	
$\boldsymbol{\zeta}$	General matrix	
η	System state (intermediate variable)	
θ	Angle	rad
$\boldsymbol{\Theta}$	Transformation matrix	
$\boldsymbol{\kappa}$	Stiffness matrix (in local Cartesian coordinate system)	N/m
κ	Generalised stiffness of a single strut	N/m
$\boldsymbol{\mu}$	Matrix of nonlinear functions	
ξ	Residual unknown input/disturbance	
ρ	Density of air	kg/m^3
σ	Stress	N/m^2
τ	Time constant	s
υ	Residuals	
$\boldsymbol{\Phi}$	General Matrix	
$\boldsymbol{\psi}$	Transformation matrix	
ω	Frequency	rad/s
ω_c	Cutoff frequency of a low-pass filter	rad/s

Superscripts	Definition	Unit
(i)	The i^{th} quantity	
(k)	The k^{th} quantity	
(e)	The e^{th} element	

Subscripts	Definition	Unit
0	Before change (initial state)	
a	Actuator related	
act	Actual	
c	Nominal controller related	
d	Unknown input/disturbance related	
D	Derivative	
dac	Disturbance-accommodating-controller	
des	Desired	
e	External	
f	Filter related	
i	The i^{th} quantity	
I	Integral	
k	The k^{th} quantity	
L	State observer related	
P	Proportional	
t	After change (final state)	
v	Intermediate variable related	
w	Internal model related	
z	Discrete-time domain related	

Chapter 1

INTRODUCTION

In this chapter, key concepts involved in our research are introduced and discussed in form of literature review. First, the active-truss-based morphing wing (ATBMW) is introduced in Section 1.1, with one of the major problems that concerns ATBMW applications in practice pointed out – the difficulties in actuator controller implementation on ATBMWs of a complicated structure. A possible solution is proposed accordingly at the end of the section. More details regarding the solution, which is the unknown-input estimation and its integration into a control system, are given in Section 1.2, and expectations on potential improvements to be made over currently available schemes for the unknown-input estimation are posed. Major issues to be considered in this research are summarised in Section 1.3, and the aim and objectives of the work documented herein are outlined in Section 1.4.

1.1 Active-Truss-Based Morphing Wing

During flight, the profile variation of aircraft wings not only controls the aircraft attitude (Barnard and Philpott, 2003, Anderson, 2008) but also contributes to aerodynamic improvements under different conditions, such as life/drag ratio optimisation (Gilbert, 1981, Bolonkin and Gilyard, 1999, Spillman, 1992), flow separation alleviation (Kota et al., 2003), gust load alleviation (Gilbert, 1981, Kota et al., 2003, Hetrick et al., 2007), and parasitic drag reduction (Gilbert, 1981). For example, a reduction in fuel consumption is a most direct benefit from aerodynamics improvements (Kota et al., 2003, Butt, 2005, Moorhouse et al., 2006). However,

limited aerodynamic improvements can be made on conventional airfoils because lumped and heavy mechanical mechanisms are required to drive control surfaces (e.g. flaps, slats, and ailerons) which in the meantime are separate or segmented components that result in unsmooth airfoil profile as a whole (Cole, 1981). In addition, the degrees of freedom in terms of shape change on conventional airfoils are restricted by the existing mechanism of control surfaces.

As one of the various types in the morphing wing technology, the active-truss-based morphing wing (ATBMW) is believed to have better aerodynamic performance over those with conventional control surfaces commonly seen on modern aircraft (Austin et al., 1994). An ATBMW realises smooth and flexible profile variation (shape morphing) through truss structures with embedded actuators as active elements.

A truss is a type of structure commonly applied in architecture and structural engineering. Straight members (e.g. struts) are basic elements in a truss and are mutually connected at each end (known as joint or node) to form one or more triangular units that construct the entire truss structure. In a planar truss all the elements and nodes lie within the same plane, while a space truss is formed when elements and nodes extend into three dimensions. A truss is statically determinate according to Maxwell's theory (Maxwell, 1864). When the length of all struts is given, the shape of the truss is known. Accordingly, a truss is also kinematically determinate if one or more elements vary in length. By replacing fixed-length elements in a truss with substitutes that can contract and extend, an active truss is formed, which is flexible in shape and meanwhile retains the merits of a static truss in terms of structural integrity and strength.

Therefore, altering the length of active truss struts can change the shape of an ATBMW while the overall structural integrity and strength are maintained (Austin et al., 1994, Ramrakhyani et al., 2005, Baker and Friswell, 2009). Various advanced actuators such as miniature linear actuators, Shape Memory Alloys (SMA), magnetostrictive materials, and piezoelectric actuators can be used to replace conventional hydraulic motors for a more compact and lighter structure (Sofla et al., 2009), so an ATBMW can be more efficient. Figure 1.1 illustrates an aircraft wing rib constructed from active trusses, the camber of which increases from zero to 10%

of chord with the maximum camber at 40% of chord. It can be seen from the figure that the length of liner actuators are changed in order to accomplish the deformation.

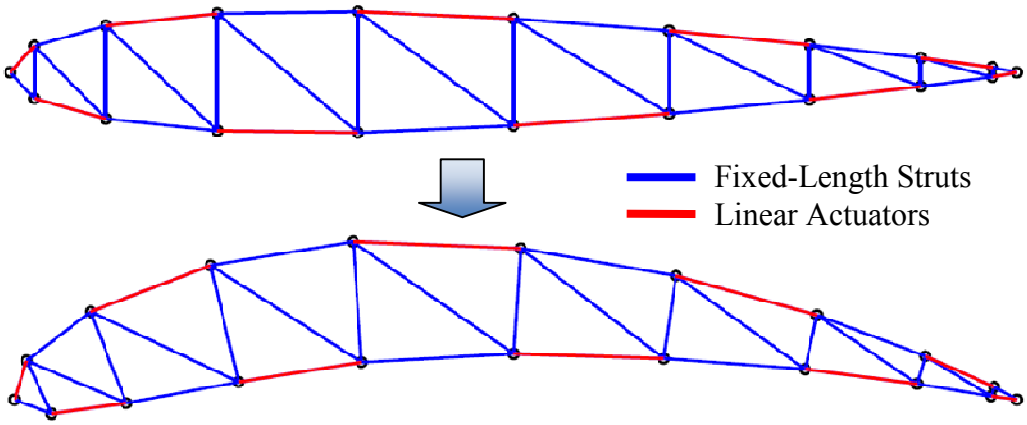

Figure 1.1: A typical example of the ATBMW

In an early research conducted by Austin et al. (1994), a wing rib assembled from planar active trusses is investigated, which is capable of small shape changes in the section between the leading and trailing edges (Figure 1.2 (a)) to improve aircraft performance during transonic cruise. Magnetostrictive materials that can vary in length in magnetic fields are proposed as active truss elements though mechanical ball-screw actuators (Figure 1.2 (b)) are actually used in experiments. Figure 1.2 (c) illustrates four possible modes of shape morphing that can be achieved.

Unlike the concept of Austin et al. (1994), repeated cellular trusses instead of separate ribs are used to construct the overall wing in the work of Ramrakhyani et al. (2005) (see Figure 1.3 (a) and (b) on page 5), which is capable of a wider range of shape morphing including span-wise deformation, for example, wing tip bending as shown in Figure 1.3 (c).

Focusing on camber control via trailing edge bending, Baker and Friswell (2009) put more efforts on optimising the location and corresponding extension of active elements for a particular wing profile to change to, where a wing rib with planar trusses is analysed. In Figure 1.4 (on page 6), length variation of each active element is illustrated in colour. As can be seen, a finer truss with more active struts offers a smoother profile.

(a) Schematic of the experimental ATBMW rib

(b) Arrangement of actuators and sensors on the experimental ATBMW rib

(c) Modes of shape morphing

Figure 1.2: An experimental ATBMW rib constructed by Austin et al. (1994)

In addition to the aforementioned ATBMW concepts, there are also other active truss structures that have the potential for aircraft wing applications (Hutchinson et al., 2003, Lucato et al., 2004, Sofla et al., 2009). However, as shown in Figures 1.1 to 1.4, ATBMWs generally need more actuators to achieve better shape morphing, and adjacent actuators may be mechanically coupled and mutually constrained. The interactions among actuators can cause considerable difficulties in acquiring an

(a) Section view of the structure

(b) Isometric view of the structure

(c) Isometric view with wing tip bended down

Figure 1.3: A conceptual ATBMW formed by repeated cellular trusses (Ramrakhyani et al., 2005)

accurate dynamic model of the entire structure and in performing on-board tuning of actuators. In addition, the large quantity of actuators required on ATBMWs with finer control surfaces and more degrees-of-freedom for shape morphing makes the aforementioned two tasks even more difficult. A satisfactory solution to this problem, although of vital importance to successful realisations of the promising ATBMW concepts, nevertheless has received little research attention.

In order to solve the problem without the necessity to modify the mechanical structure, the focus of our research is placed on improving the actuator controller. If all necessary and crucial procedures involved in controller implementation can be

accomplished on individual actuators outside the wing structure prior to the assembly of the wing, then the problem associated with interactions in a complex structure can be bypassed. That is, if the controller can be based on actuator dynamics only, tuned, and tested on individual actuators before the actuators are assembled on the wing, and remain robust when actuators are in place, then the entire controller implementation process (design, tuning, and testing) is free from structural coupling constraints. In this case, there is no need to use a precise overall wing model for controllers or to further tune actuators on board. To achieve this, it is proposed to integrate a scheme for unknown-input estimation into a conventional (nominal) controller (e.g. Linear-Quadratic-Gaussian controller) for actuator motion control. The unknown-input estimation scheme can estimate and subsequently compensate effects from most uncertainties, so that the nominal controller remains unaffected in the presence of these uncertainties. With enhanced tolerance to uncertainties, such a compound controller can be designed simply according to actuator dynamics, since un-modelled dynamics from the wing structure and unmeasured loads from the working environment can be handled accordingly by the unknown-input estimation scheme.

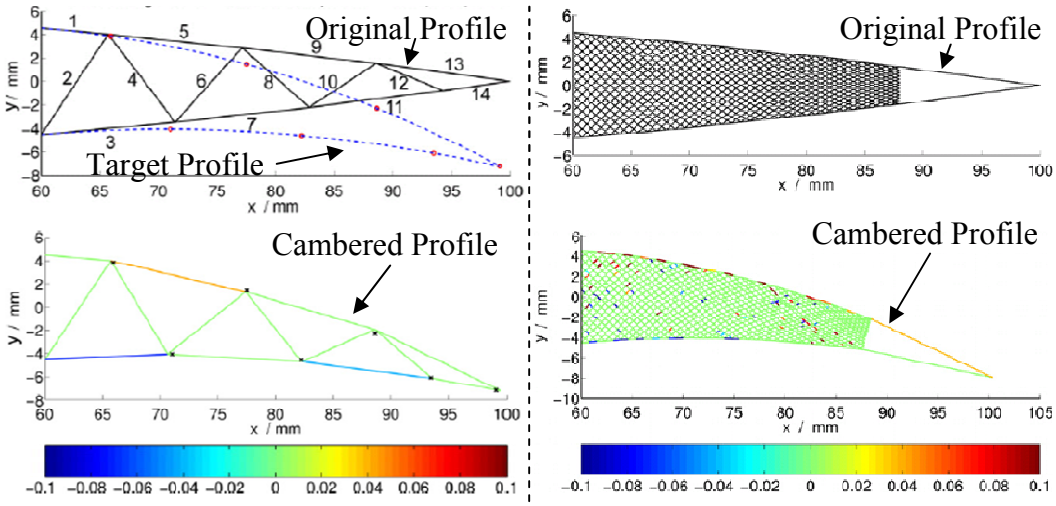

(a) ATBMW rib trailing edge formed by 14 elements with 3 actuators

(b) ATBMW rib trailing edge formed by 1752 elements with 88 actuators

Figure 1.4: Simulation of ATBMW trailing edge shape morphing (Baker and Friswell, 2009)

1.2 Unknown-Inputs Estimation

In reality, a control system is always subjected to uncertainties including un-modelled nonlinearities and quantities that in some cases are unmeasurable or inconvenient to measure such as parameter variation and unknown inputs. Disturbances from external excitations are typical unknown inputs. The continuously changing payload is regarded as an unknown input as well when it is not measured. Actuator controllers designed under ideal conditions or specific assumptions may fail to work or have poor performance if these uncertainties are not taken into account in the design process. To attenuate influences from uncertainties, various methods can be used. In addition to some commonly applied techniques such as H_∞ robust control (McFarlane and Glover, 1988, Doyle et al., 1989, Dietz and Scherer, 2010) and adaptive intelligent control (Dadone et al., 2003, Mohammadzaheri and Chen, 2010a, Mohammadzaheri and Chen, 2010b), the method of unknown-input estimation or prediction appears to be an attractive solution which enables better tolerance to uncertainties, as demonstrated by various industrial applications. It treats most uncertainties as equivalent unknown inputs, estimates these unknown inputs via an observer, and subsequently constructs counteractive control efforts to cancel the effects from uncertainties. It has been shown in industrial applications where various servomechanisms are involved, that the incorporation of unknown-input estimation and compensation into existing conventional controllers offers enhanced disturbance rejection and consequently better performance robustness in terms of set-point regulation or real-time tracking. These applications include and are not limited to power converter (Sun and Gao, 2005), paper machine (Valenzuela et al., 2007), machine tools (Cheng and Peng, 2007, Huang et al., 2010, She et al., 2011), precision positioning table (Tan et al., 2003), active magnetic bearings (Schuhmann et al., 2012), robots (Umeno et al., 1993, Komada et al., 2000, Mitsantisuk et al., 2012), and computer disk drives (White et al., 2000, Lee et al., 2012). Especially in the work of Umeno et al. (1993), where unknown-input estimation is employed in the decentralised joint control system of a multi-axis robot manipulator, the controller design per se and subsequent overall control system design are significantly simplified, without the necessity to consider various kinds of dynamic forces at joints.

As introduced in the following subsections, various methods are available to design such an observer for unknown-input estimation.

1.2.1 Estimation of Partially Unknown Inputs

Though some external inputs to a system are unknown in magnitude, they may generally be identifiable as a combination of a series of harmonics, corresponding characteristics of which can be extracted from data acquired in either experiments or practical applications. In this case, these inputs are regarded as partially unknown.

(1) Extended State Observer

By augmenting a Luenberger state observer (Luenberger, 1964) to include both models of the plant and the partially unknown inputs, an extended state observer is formed, which is capable of estimating states of not only the plant but also unknown inputs. The basic concept of an extended observer in a linear regulator is illustrated in Figure 1.5. $\hat{\boldsymbol{x}}(t)$ in the figure is the vector of estimated plant states. The resultant control effort is $\boldsymbol{u}(t) = \boldsymbol{u}_c(t) - \boldsymbol{u}_d(t)$, where $\boldsymbol{u}_c(t)$ is the normal control effort from the nominal controller for plant regulation while $\boldsymbol{u}_d(t)$ is obtained from the estimate of $\boldsymbol{d}(t)$. In this way, dominant unknown external inputs can be cancelled accordingly.

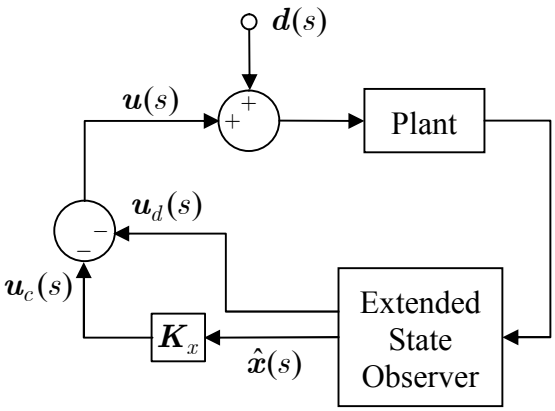

Figure 1.5: Basic concept of an extended state observer

In the work of Johnson (1971), the method of constructing an extended observer is based on the following plant model:

$$\begin{cases} \dot{\boldsymbol{x}}(t) = \boldsymbol{A}\boldsymbol{x}(t) + \boldsymbol{B}\boldsymbol{u}(t) + \boldsymbol{B}_d\boldsymbol{d}(t) \\ \boldsymbol{y}(t) = \boldsymbol{C}\boldsymbol{x}(t) \end{cases}, \tag{1.1}$$

where $\boldsymbol{A}$, $\boldsymbol{B}$, $\boldsymbol{B}_d$, and $\boldsymbol{C}$ are known system matrixes, $\boldsymbol{x}(t)$ is the plant state vector, $\boldsymbol{y}(t)$ is the vector of measured plant outputs, vector $\boldsymbol{u}(t)$ contains control inputs, and vector $\boldsymbol{d}(t)$ represents partially unknown inputs.

The model of $\boldsymbol{d}(t)$ is further described by a group of differential equations

$$\begin{cases} \dot{\boldsymbol{x}}_d(t) = \boldsymbol{A}_d(t)\boldsymbol{x}_d(t) + \boldsymbol{\delta}(t) \\ \boldsymbol{d}(t) = \boldsymbol{C}_d(t)\boldsymbol{x}_d(t) \end{cases}, \tag{1.2}$$

where $\boldsymbol{x}_d(t)$ is the state vector of the unknown inputs; $\boldsymbol{\delta}(t) = [\delta_1(t), \delta_2(t), \cdots, \delta_n(t)]^T$ contains isolated impulses $\delta_n(t)$ of random intensity and occurrence; $\boldsymbol{A}_d(t)$ and $\boldsymbol{C}_d(t)$ are matrixes selected by the designer.

A so-called "disturbance accommodating controller" is then constructed by integrating the model of $\boldsymbol{d}(t)$ into the state observer. By appropriate linear transformations, the overall controller with the extended state observer based on the scheme in Figure 1.5 is presented in a specific structure described by matrixes $\boldsymbol{A}_{dac}$, $\boldsymbol{B}_{dac}$, $\boldsymbol{B}_y$, and $\boldsymbol{C}_{dac}$, as shown in Figure 1.6. Feasible implementations of the estimation scheme in servomechanisms are also developed in a similar way.

Different from Johnson's approach, Davison (1972) introduces the model of partially unknown inputs by assuming that the unknown inputs are directly imposed on every system state as in

$$\begin{cases} \dot{\boldsymbol{x}}(t) = \boldsymbol{A}\boldsymbol{x}(t) + \boldsymbol{B}\boldsymbol{u}(t) + \boldsymbol{d}(t) \\ \boldsymbol{y}(t) = \boldsymbol{C}\boldsymbol{x}(t) \end{cases}. \tag{1.3}$$

Accordingly, the vector $\boldsymbol{d}(t) \in \mathbb{R}^{n_x \times 1}$ has each of its components described in a different form:

$$d_k^{(g)}(t) + b_g d_k^{(g-1)}(t) + \cdots + b_2 d_k^{'}(t) + b_1 d_k(t) = 0, \qquad (k = 1,2,\cdots,n_x), \quad (1.4)$$

where $d_k^{(g)}(t)$ is the g^{th}-order derivative of $d_k(t)$, the initial value of which is unknown; n_x denotes the number of plant states; Coefficients $(b_1, b_2, \cdots, b_g)$ of the polynomial are to be decided by the designer.

The representation in Eq (1.4) is essentially the same as that in Eq (1.2) by manipulating Eq (1.4) into a first-order differential equation with variables in matrix form, as commented by Johnson (1972).

Under some different assumptions, a controller that enables robust reference tracking and disturbance rejection is then developed on the basis of the model in Eq (1.4) with full-state feedback. In a later study, Davison (1975) generalises his approach to the construction of an extended state observer, by which both plant states and the external partially unknown inputs are estimated simultaneously.

Figure 1.6: Optimal linear regulator with disturbance accommodating controller (Johnson, 1971)

Literally, the models in Eqs (1.2) and (1.4) are capable of reconstructing the external signals of interest as long as these signals have characteristics that conform to a linear combination of the fundamental solutions of a finite-dimensional time-varying (or time-invariant) linear differential equation. And it is claimed that a vast majority of external inputs involved in control problems in practice fall into the range covered by models of this type (Johnson, 1971, Johnson, 1972, Davison, 1972). However, there is a most important prerequisite that characteristics of these inputs such as the mean, covariance, power spectral density, and other statistical properties must be known, which can only be obtained from data in either practice or experiments. This is inconvenient, time-consuming, and costly in most situations, and the consistency of data acquired is not guaranteed in every occasion. As a result, determinate characteristics of the external inputs cannot always be found, especially when the external inputs are completely random. Moreover, the inclusion of a model of exogenous signals increases the dimension of the observer at the same time, especially when the signals are complicated and need a higher-order model, which is undesired for the sake of computation speed.

An application example regarding the extended state observer can be found in the work of Ohishi et al. (1987), where a minimum-order discrete observer is developed and used for a position servo system. For simplicity and fast estimation speed, unknown external loads are treated as constants, the representation of which then becomes a subset of the models in Eqs (1.2) and (1.4) with an order of one. The resulting controller could effectively reject constant disturbances and maintain system tracking precision even when only a proportional (P) controller is applied as the nominal controller. However, degraded performance occurs when some system parameters vary with time, such as armature resistance and motor torque constant, both assumed to be constants in controller design. The variation of these parameters induces nonlinearities into the system, resulting in equivalent disturbing loads superimposed on existing constant external loads. As a consequence, the total load exerted on the system is not constant but time-varying, which is then beyond the scope of the constant disturbance model. Increasing the order of the model of unknown inputs would help to cope with a wider range of disturbance but in the

meantime slows down the estimation performance due to the requirement on longer sampling delay when digitally implemented, as acknowledged by Ohishi et al. (1987).

(2) Internal Model Principle

On the basis of similar techniques for modelling partially unknown inputs, the Internal Model Principle proposes to place the model of external inputs separately in the feedback path, apart from the state observer, individually predicting exogenous signals according to plant outputs (Francis and Wonham, 1975). Corresponding stability analysis and control system design are further generalised to multi-input multi-output (MIMO) systems by Hara et al. (1988), with a modified control scheme proposed.

Despite some successful industrial applications utilizing the Internal Model Principle, limitations remain, similar to those of an extended state observer, that only repetitive external disturbances can be effectively modelled and rejected whereas other types of signals not described by the model cannot be coped with well.

1.2.2 Estimation of Completely Unknown Inputs

When external inputs are completely unknown, that is, not only random in magnitudes, but also have undetermined characteristics, then it is impossible to retrieve dominant patterns of these inputs via field or experiment data, and hence not feasible to estimate them via the model in form of a linear differential equation as mentioned in Section 1.2.1. To deal with completely unknown inputs, following methods apply.

(1) Estimation Function with Unknown-Input-Decoupled Observer

Instead of using a model based on a priori assumptions or empirical knowledge, the estimation of completely unknown inputs is possible by means of combining a so-called unknown-input-decoupled observer (UIDO) (Wang et al., 1975, Yang and Wilde, 1988, Hou and Muller, 1994, Hou and Patton, 1998) with an additional function or function group (Park and Stein, 1988, Hou and Muller, 1992). The former

is used to observe plant states while the latter is for computing the approximate magnitude of unknown inputs.

The UIDO, also known as unknown-input observer (UIO) in some literature (Kudva et al., 1980, Guan and Saif, 1991, Darouach et al., 1994), does not actually estimate unknown external inputs but remains an observer for plant states estimation. The major difference between a UIDO and a Luenberger state observer is that the latter requires all system inputs to be known while the former can work under conditions subjected to unknown external inputs. As literally indicated, the UIDO bases its principle on decoupling the unmeasurable inputs and corresponding system dynamics from the state observer so that only the known system variables such as measured system outputs and control inputs are used for states estimation. In other words, the effects from unknown inputs on system states estimation are isolated.

The estimation of unknown inputs is accomplished by an additional estimation function, using plant information obtained from both the UIDO and measurements. In the work of Hou and Muller (1992), the estimate of unknown inputs $\hat{\boldsymbol{d}}(t)$ for a linear time-invariant system is given by:

$$\hat{\boldsymbol{d}}(t) = \boldsymbol{\zeta}_1 \dot{\boldsymbol{y}}(t) + \boldsymbol{\zeta}_2 \boldsymbol{y}(t) + \boldsymbol{\zeta}_3 \hat{\boldsymbol{x}}(t) + \boldsymbol{\zeta}_4 \boldsymbol{u}(t), \tag{1.5}$$

where matrixes $\boldsymbol{\zeta}_1$, $\boldsymbol{\zeta}_2$, $\boldsymbol{\zeta}_3$, and $\boldsymbol{\zeta}_4$ are derived from known system characteristics, and estimated plant states $\hat{\boldsymbol{x}}(t)$ are obtained from the UIDO.

As can be seen in Eq (1.5), the derivative of $\boldsymbol{y}(t)$, namely $\dot{\boldsymbol{y}}(t)$, is needed, which makes the estimation sensitive to noises. The necessity to differentiate measured outputs is also one of the limitations in the approach of an earlier study by Park and Stein (1988).

(2) Unknown-Input Estimation Function with Ordinary State Observer

Without decoupling unknown inputs, an ordinary state observer can still work properly in the case that the unknown inputs are cancelled by corresponding control

inputs. Similarly, an estimation function is needed in addition to the ordinary state observer so as to predict unknown inputs.

The method of Corless and Tu (1998) does not differentiate the measured outputs, with the outputs of the state observer and unknown-input estimation function given by:

$$\begin{cases} \dot{\hat{\boldsymbol{x}}}(t) = \boldsymbol{A}\hat{\boldsymbol{x}}(t) + \boldsymbol{B}\hat{\boldsymbol{d}}(t) + \boldsymbol{L}[\boldsymbol{C}\hat{\boldsymbol{x}}(t) - \boldsymbol{y}(t)], \hat{\boldsymbol{x}}(t_0) = \hat{\boldsymbol{x}}_0 \\ \hat{\boldsymbol{d}}(t) = \boldsymbol{d}_0[t, \hat{\boldsymbol{x}}(t)] - \gamma\boldsymbol{\zeta}[\boldsymbol{C}\hat{\boldsymbol{x}}(t) - \boldsymbol{y}(t)] \end{cases}, \tag{1.6}$$

where $\boldsymbol{L}$ is the state observer gain matrix to design; $\hat{\boldsymbol{x}}_0$ is an arbitrary initial value of the state estimate $\hat{\boldsymbol{x}}(t)$; $\boldsymbol{d}_0[t, \hat{\boldsymbol{x}}(t)]$ is an initial estimation of $\hat{\boldsymbol{d}}(t)$; The scalar γ and matrix $\boldsymbol{\zeta}$ need to be selected by the designer.

The function $\hat{\boldsymbol{d}}(t)$ uses a two-term expression, with one being an initial estimation, and the other being a real-time correction. It is claimed that any desired degree of accuracy on the estimation of both plant states and unknown inputs can be achieved by appropriate selection of γ. However, the initial estimate $\boldsymbol{d}_0[t, \hat{\boldsymbol{x}}(t)]$ is restricted in a particular form, and does not suit any other systems with dynamics that cannot be described in this special form. Furthermore, it is required that the number of unknown inputs to be estimated must not be larger than that of available measurements, and therefore a new problem presents when the estimation scheme is to be applied in an existing state-space based control system where unknown inputs enter the system at channels different from control inputs. No applicable solution is implied subject to the assumptions on rank conditions to be satisfied.

Similar to the study of Corless and Tu (1998), the two-term expression to reconstruct unknown inputs without the necessity to differentiate measured outputs is also adopted in the approach of Liu and Peng (2000), while additional nonlinear dynamics $\boldsymbol{\mu}[\boldsymbol{u}(t), \boldsymbol{x}(t)]$ in the system are considered. The state observer is given by:

$$\dot{\hat{\boldsymbol{x}}}(t) = \boldsymbol{A}\hat{\boldsymbol{x}}(t) + \boldsymbol{\mu}[\boldsymbol{u}(t), \boldsymbol{x}(t)] + \boldsymbol{B}\hat{\boldsymbol{d}}(t) + \boldsymbol{K}_L[\boldsymbol{x}(t) - \hat{\boldsymbol{x}}(t)], \tag{1.7}$$

where $\boldsymbol{K}_L$ is the observer gain matrix.

Accordingly, the estimate of unknown inputs is obtained via:

$$\begin{cases} \hat{\boldsymbol{d}}(t) = \hat{\boldsymbol{d}}_0(t) - \boldsymbol{K}_0[\hat{\boldsymbol{x}}(t) - \boldsymbol{x}(t)] \\ \dot{\hat{\boldsymbol{d}}}_0(t) = -\boldsymbol{B}^T\boldsymbol{\zeta}[\hat{\boldsymbol{x}}(t) - \boldsymbol{x}(t)] \\ \boldsymbol{K}_0(\boldsymbol{A} - \boldsymbol{K}_L) + \boldsymbol{K}_0\boldsymbol{B}\boldsymbol{K}_0 + \boldsymbol{B}^T\boldsymbol{\zeta} = 0 \end{cases}, \tag{1.8}$$

where $\hat{\boldsymbol{d}}_0(t)$ is an initial estimate for $\hat{\boldsymbol{d}}(t)$, $\boldsymbol{K}_0$ is the correction gain matrix for a more accurate estimation, and matrix $\boldsymbol{\zeta}$ is an intermediate variable.

The solution of the correction gain is guaranteed in single-input single-output (SISO) cases and could be found symbolically for low-order MIMO systems, but becomes difficult to obtain when the number of unknown inputs increases. In addition, it is the estimated plant states $\hat{\boldsymbol{x}}(t)$ and actual plant states $\boldsymbol{x}(t)$ that are simultaneously used in the correction term. This is impractical in reality as the measured outputs $\boldsymbol{y}(t)$ are not necessarily the same as $\boldsymbol{x}(t)$. If $\boldsymbol{y}(t)$ are different from $\boldsymbol{x}(t)$, then a mathematical transformation must be performed, otherwise the correction gain matrix $\boldsymbol{K}_0$ should be modified. However, neither the transformation of states nor the modification of $\boldsymbol{K}_0$ is addressed.

To overcome the above limitations, Liu and Peng (2002) proposes another estimation function of the form below, with a modified nonlinear dynamics considered:

$$\hat{\boldsymbol{d}}(t) = \boldsymbol{\zeta}_1\boldsymbol{y}(t) + \boldsymbol{\zeta}_2\dot{\boldsymbol{y}}(t) + \boldsymbol{\zeta}_3\hat{\boldsymbol{x}}(t) + \boldsymbol{\zeta}_4\dot{\hat{\boldsymbol{x}}}(t) + \boldsymbol{\zeta}_5\boldsymbol{\mu}[\boldsymbol{u}(t), \boldsymbol{y}(t)], \tag{1.9}$$

where matrixes $\boldsymbol{\zeta}_1$, $\boldsymbol{\zeta}_2$, $\boldsymbol{\zeta}_3$, $\boldsymbol{\zeta}_4$, and $\boldsymbol{\zeta}_5$ are to be designed in accordance with known system dynamics, $\boldsymbol{\mu}[\boldsymbol{u}(t), \boldsymbol{y}(t)]$ is a vector of known nonlinear functions of $\boldsymbol{u}(t)$ and $\boldsymbol{y}(t)$, and vector $\hat{\boldsymbol{x}}(t)$ is obtained from the Luenberger state observer.

However, it is necessary to differentiate the measured output $\boldsymbol{y}(t)$ so as to obtain an estimation of unknown inputs. Moreover, the constant design matrixes are to be

obtained by means of nonlinear optimisation, the optimal results of which are not guaranteed, and some empirical knowledge is required. The case becomes more complex when the number of unknown inputs increases in an MIMO system.

With the same objectives that only the measured outputs (but not their derivatives) are used for plant states and unknown-input estimation, an estimation scheme based on two separate order-reduced observers is proposed by Xiong and Saif (2003). It is claimed that the proposed estimator requires less restrictive conditions, and suits some non-minimum phase systems as well. The major drawback is that the complexity of parameter selection in design significantly increases for the sake of less restrictive conditions on unknown inputs.

In a two-term structure but featuring a low-pass filter based high-gain approach, the method of She et al. (2008) is more straightforward in design, with a simpler estimation algorithm. On the basis of constructing the equivalents of unknown inputs at control input channels, the scheme focuses on effectively counteracting undesirable effects from unknown inputs rather than a direct estimation on magnitudes of unknown inputs. Therefore in this case the number of unknown inputs does not necessarily need to be equal to or less than measured outputs and could be at any channels different from control inputs. The design is simple and the designers only need to specify the ordinary state observer gain and the filter coefficient for the first-order low-pass filter. The problem is that the function for unknown-input estimation is dependent on the gain of the ordinary state observer, imposing constraints on the state observer design, though a separation theorem is claimed to hold for the design of both. In other words, specifications for unknown-input estimation have some influence on the design of the state observer.

(3) Disturbance Observer

As a counterpart of designs in state space, the Disturbance Observer (DOB) synthesized in frequency domain is a generalisation of the extended state observer according to the analysis of Schrijver and van Dijk (2002), which however, does not require a model of unknown inputs. To properly estimate unknown inputs, the DOB relies on a low-pass filter and the inversion of plant dynamics. Its basic principle is

illustrated in Figure 1.7, where $P(s)$ represents actual plant dynamics, $P_n^{-1}(s)$ is the inverse of the nominal model of the plant, and $G_f(s)$ is a low-pass filter of unity DC gain.

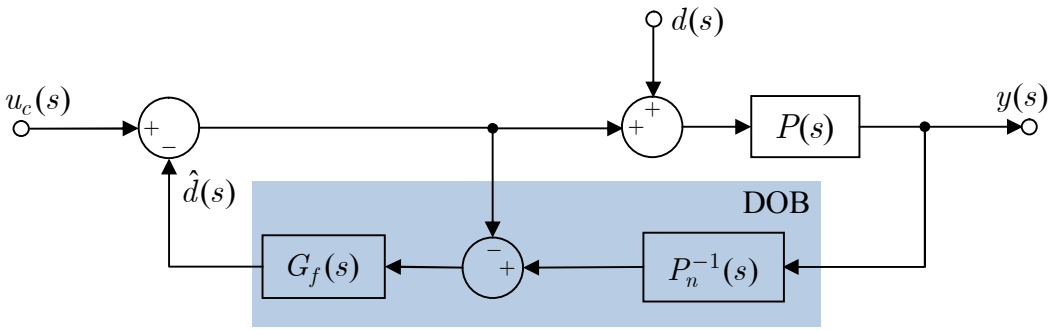

Figure 1.7: Basic concept of a continuous-time DOB for SISO systems

The low-pass filter $G_f(s)$ plays an important role in the DOB in terms of determining the robustness of DOB and performance of unknown-input suppression. Unlike the low-pass filter mentioned in the study of She et al. (2008), the design of $G_f(s)$ in a DOB appears to be a more sophisticated process, as $G_f(s)$ must be carefully designed so as to maintain system stability (Ohnishi, 1987). A general rule is that zeros of $G_f(s)$ and $1-G_f(s)$ should be able to cancel out those unstable poles of the plant, and the order of $G_f(s)$ must be larger than that of the plant. A Butterworth filter is used by Umeno and Hori (1991) for $G_f(s)$, while H_∞ norm optimisation is tried in a later study (Umeno et al., 1993) to determine coefficients of a parameterized $G_f(s)$ of a more general form. To overcome problems posed by significant time delay in a plant, the work of Kempf and Kobayashi (1999) adapts the DOB accordingly by means of discrete-time design techniques. The influence of DOB order on system robustness and stability is studied by Komada et al. (2000) through investigating the order of $G_f(s)$, nominal plant model, and disturbance model. Generally, no disturbance model is required in DOB, but Komada et al. (2000) uses disturbance models (step, ramp, and parabolic functions) as an aid to specify an appropriate order of $G_f(s)$ and corresponding coefficients of numerator and

denominator polynomials. It is found that increasing the order of $G_f(s)$ yields more choices for the nominalisation of plant dynamics, meanwhile induces increased phase lag. Though it is claimed that a proper selection of polynomial coefficients of $G_f(s)$ would improve system robustness, no guidelines are given. The robustness of a DOB is further investigated by Choi et al. (2003) with regards to the relative degree, numerator order and denominator order of $G_f(s)$, but only the guidelines for a second-order system is specifically suggested.

As an alternative to solving for plant dynamics inversion, the methodology proposed by Du et al. (2010) for discrete-time DOB modifies the term of inversed dynamics into two new terms $\zeta_1(z)$ and $\zeta_2(z)$ that can be readily obtained from the numerator and denominator polynomials of the nominal plant model transfer function in the z-plane (Figure 1.8). Similarly, the low-pass filter is specified by means of H_∞ optimisation. It appears to be a simpler design method than those requiring an inversion of plant dynamics, but empirical knowledge regarding characteristics of unknown inputs is necessary in order to specify appropriate weightings for the optimisation.

Figure 1.8: A discrete-time DOB for SISO systems (Du et al., 2010)

It is worth notice that the aforementioned studies (Ohnishi, 1987, Umeno and Hori, 1991, Umeno et al., 1993, Kempf and Kobayashi, 1999, Komada et al., 2000, Choi et al., 2003, Du et al., 2010) are limited to applications in SISO systems. Plant inversion brings some difficulties for the DOB to be employed in MIMO systems

since an inverse cannot always be found. Though Du et al. (2010) avoid the necessity of solving for the inverse of plant dynamics, corresponding method is developed on an SISO basis.

The generalisation of the DOB to MIMO cases in the study of Shahruz (2009) bypasses plant inversion and adopts parameterized controller design through an optimisation process (Figure 1.9). The relation between measured outputs $\boldsymbol{y}(s)$ and unknown inputs $\boldsymbol{d}(s)$ in a regulator problem is derived as:

$$\boldsymbol{y}(s) = \left[\boldsymbol{I}_{n_y} - \boldsymbol{P}_n(s)\boldsymbol{\zeta}(s)\right]\left\{\boldsymbol{I}_{n_y} + [\boldsymbol{P}(s) - \boldsymbol{P}_n(s)]\boldsymbol{\zeta}(s)\right\}^{-1}\boldsymbol{P}(s)\boldsymbol{d}(s)\,, \qquad (1.10)$$

where $\boldsymbol{I}_{n_y}$ is an identity matrix of dimension $n_y \times n_y$, with n_y denoting the number of measured outputs; $\boldsymbol{P}(s)$ and $\boldsymbol{P}_n(s)$ are transfer matrix of the actual plant and nominal plant, respectively; $\boldsymbol{\zeta}(s)$ is a transfer matrix to design.

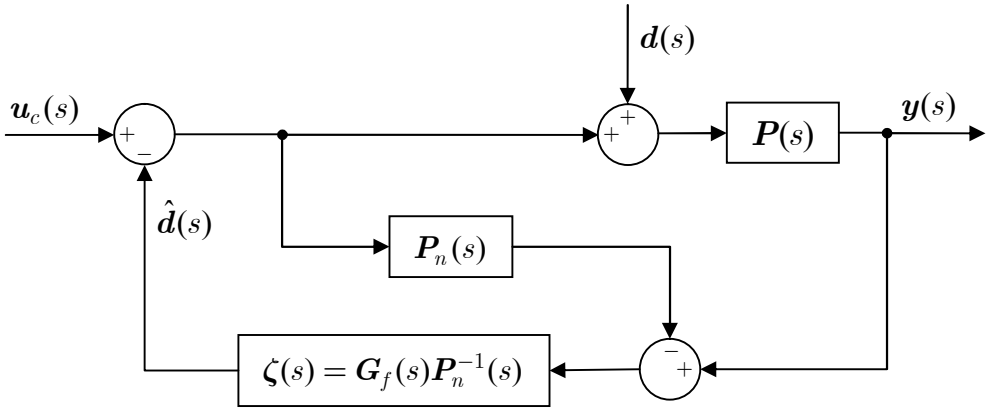

Figure 1.9: A continuous-time DOB for MIMO systems (Shahruz, 2009)

Assuming $\boldsymbol{P}_n(s) = \boldsymbol{P}(s)$ yields

$$\boldsymbol{y}(s) = [\boldsymbol{P}_n(s) - \boldsymbol{P}_n(s)\boldsymbol{\zeta}(s)\boldsymbol{P}_n(s)]\boldsymbol{d}(s)\,. \qquad (1.11)$$

As can be seen from Eqs (1.10) and (1.11) as well as Figure 1.9, the problem of designing an MIMO low-pass filter $\boldsymbol{G}_f(s)$ and finding plant inversion reduces to selecting only one term $\boldsymbol{\zeta}(s)$, which is actually another representation of the

combination of the two important elements in an DOB: the low-pass filter $\boldsymbol{G}_f(s)$ and inversed plant dynamics $\boldsymbol{P}_n^{-1}(s)$. Instead of solving for $\boldsymbol{G}_f(s)$ and $\boldsymbol{P}_n^{-1}(s)$, the proposed method parameterizes $\boldsymbol{\zeta}(s)$ by assigning a fixed-order transfer function to every element of $\boldsymbol{\zeta}(s)$, and then select the gain, numerator polynomial coefficients and denominator polynomial coefficients of each transfer function. The design is conducted via an optimisation algorithm working on H_∞ cost functions. It is suggested that transfer functions of higher order yields better results in unknown-input estimation, and the optimisation procedure can start from low-order transfer functions and gradually increase the order until satisfactory result is achieved. It is a time-consuming and tedious process, and empirical knowledge is needed to specify initial values of optimisation parameters. Given the fact that whether a global optimum can be found largely depends on the selection of these initial values, a trail-and-error process is normally required, and a global optimum is not guaranteed.

(4) Discrete-time Observer

As can be seen in aforementioned schemes, discrete-time design techniques are useful in solving some particular problems involved in unknown-input estimation (Ohishi et al., 1987, Kempf and Kobayashi, 1999, Du et al., 2010). There are also some discrete-time design techniques that do not fall into the categories depicted and has respective special features (She et al., 2005, Chang, 2006, Lee et al., 2012).

In the study of She et al. (2005), a geometry-based method is employed to construct a curvature model for unknown-input estimation. The resulting low-order nonlinear expression for predicting unknown inputs has a relatively simple structure, with the sampling period and a nominal state-space model of the plant as dominant parameters, and there are not any further design efforts such as selection of some parameters that vary with plant dynamics. After the unknown-input estimation scheme is integrated into an existing controller, the stability of the overall system is not affected while disturbances to the system are attenuated. The limitations are: Firstly, the estimation accuracy is primarily determined by the sampling rate and cannot be adjusted at a fixed sampling rate; Secondly, it is the states of the plant (of

controllability canonical form) but not system outputs that need to be fed back to the disturbance observer, which is impractical in cases where these states are unmeasurable. A possible solution to the latter could be using a state observer, the implementation of which and corresponding influence on unknown-input estimation dynamics is nonetheless not documented.

A so-called proportional integral observer (PIO) for discrete-time implementation is proposed by Chang (2006). As indicated literally, the PIO has a similar structure to an ordinary state observer but has an additional integral term for unknown-input estimation:

$$\begin{cases} \hat{\boldsymbol{x}}(k+1) = \boldsymbol{A}_z\hat{\boldsymbol{x}}(k) + \boldsymbol{B}_{z1}\boldsymbol{u}(k) + \boldsymbol{L}_{z1}[\boldsymbol{y}(k) - \hat{\boldsymbol{y}}(k)] + \boldsymbol{B}_{z2}\hat{\boldsymbol{d}}(k) \\ \hat{\boldsymbol{d}}(k+1) = \hat{\boldsymbol{d}}(k) + \boldsymbol{L}_{z2}[\boldsymbol{y}(k) - \hat{\boldsymbol{y}}(k)] \\ \hat{\boldsymbol{y}}(k) = \boldsymbol{C}_z\hat{\boldsymbol{x}}(k) \end{cases}, \qquad (1.12)$$

where $\boldsymbol{A}_z$, $\boldsymbol{B}_{z1}$, $\boldsymbol{B}_{z2}$, and $\boldsymbol{C}_z$ are equivalent discrete-time system matrixes; $\boldsymbol{L}_{z1}$ and $\boldsymbol{L}_{z2}$ are observer gain matrixes to design; $\boldsymbol{u}(k)$, $\hat{\boldsymbol{x}}(k)$, $\boldsymbol{y}(k)$, $\hat{\boldsymbol{y}}(k)$, and $\hat{\boldsymbol{d}}(k)$ are vectors of control inputs, estimated states, measured plant outputs, estimated plant outputs, and estimated unknown inputs in discrete-time domain, respectively.

The dynamics of system states and unknown-input estimation is given by:

$$\begin{bmatrix} \boldsymbol{e}_x(k+1) \\ \boldsymbol{e}_d(k+1) \end{bmatrix} = (\boldsymbol{\zeta}_1 - \boldsymbol{L}_z\boldsymbol{\zeta}_2)\begin{bmatrix} \boldsymbol{e}_x(k) \\ \boldsymbol{e}_d(k) \end{bmatrix} + O(t_s^2), \qquad (1.13)$$

where $\boldsymbol{e}_x(k) = \boldsymbol{x}(k) - \hat{\boldsymbol{x}}(k)$, $\boldsymbol{e}_d(k) = \boldsymbol{d}(k) - \hat{\boldsymbol{d}}(k)$, $\boldsymbol{\zeta}_1 = \begin{bmatrix} \boldsymbol{A}_z & \boldsymbol{B}_{z2} \\ \boldsymbol{0} & \boldsymbol{I} \end{bmatrix}$, $\boldsymbol{\zeta}_2 = [\boldsymbol{C}_z \quad 0]$, $\boldsymbol{L}_z = \begin{bmatrix} \boldsymbol{L}_{z1}^T & \boldsymbol{L}_{z2}^T \end{bmatrix}^T$, and t_s is the sampling period.

For $k \to \infty$, we can have $\boldsymbol{x}(k) \to \hat{\boldsymbol{x}}(k)$ and $\hat{\boldsymbol{d}}(k) \to \boldsymbol{d}(k)$, with estimation error bounded within $O(t_s^2)$. However, in order to achieve the estimation precision as claimed, the PIO relies on the smoothness of unknown inputs. Moreover, the integral action may cause undesired response during the transient phase of estimation, such as

increased estimation overshoot, subsequent resonance and longer settling time, which substantially degrade the estimation accuracy, due to reduced damping at a higher estimation gain.

A different formulation for predicting unknown inputs is proposed in the study of Lee et al. (2012) using the following structure without an integral action:

$$\begin{aligned} \overline{\boldsymbol{\eta}}(k+1) &= \overline{\boldsymbol{A}}_z \overline{\boldsymbol{\eta}}(k) - \overline{\boldsymbol{B}}_{z1} \boldsymbol{u}_c(k) \\ \hat{\boldsymbol{\eta}}(k) &= \overline{\boldsymbol{\eta}}(k) - \boldsymbol{B}_{z2}^{\dagger} \hat{\boldsymbol{x}}(k) \\ \hat{\boldsymbol{d}}(k) &= \boldsymbol{K}_d \hat{\boldsymbol{\eta}}(k) \end{aligned} \quad , \tag{1.14}$$

where vector $\overline{\boldsymbol{\eta}}(k)$ contains projected plant states in a subspace with corresponding estimates denoted by $\hat{\boldsymbol{\eta}}(k)$; $\overline{\boldsymbol{A}}_z$ and $\overline{\boldsymbol{B}}_{z1}$ are plant system matrix and control input matrix projected in a subspace, respectively; $\boldsymbol{B}_{z2}^{\dagger}$ is a generalised inverse of the distribution matrix of unknown inputs; $\boldsymbol{K}_d$ is a gain matrix to design.

Unlike the approach of She et al. (2005), estimated states and actual measurements are used together for unknown-input estimation, which appears to be more practical and feasible in cases where not all states are available from measurement. As shown in Eq (1.14), no integral action is needed for the estimation of unknown inputs and hence better transient estimation response is obtained with less estimation delay compared with DOBs, improving the transient response of the overall system in the presence of unknown inputs. However, a prerequisite remains, that the magnitude of unknown inputs at adjacent two sampling time should not vary drastically, and it becomes trickier to solve for $\boldsymbol{K}_d$, for which iterative trail-and-error procedures based on H_∞ optimisation is required.

1.3 Problems to be Addressed

To sum up, problems to be addressed within the scope of the research work documented herein are as follows.

(1) The interaction among mechanically coupled and mutually constrained active structural elements on ATBMWs poses considerable difficulties in acquiring an accurate dynamic model of the entire structure for controller design and inconveniences in performing on-board tuning of controllers. In addition, the large quantity of actuators used on the ATBMWs with finer control surfaces and more degrees-of-freedom for shape morphing makes the aforementioned two tasks even more difficult. A solution is thus needed so that reliable actuator controller designs can be obtained without the necessity to refer to the overall structural dynamics and without the need for on-board tuning.

(2) A possible solution to the problem above is to integrate an additional component for unknown-input estimation into an existing servomechanism. Existing techniques in literature for estimating unknown inputs are subjected to one or more of the following requirements:

- Detailed knowledge regarding unknown inputs
- Derivatives of measured outputs
- Inversion of plant dynamics
- Coupled and thus constrained state observer design
- Parameter optimisation (global optimum not guaranteed)
- Numerous parameter matrixes with sophisticated design rules

All the above inevitably leads to either complicated designs or simpler forms but with limited design freedom. For ATBMWs with an enormous amount of actuators, a simple scheme for unknown-input estimation is preferred, which is also expected to have sufficient design freedom in the meantime.

In other words, the above two problems are both about a major concern with regard to the realisation of ATBMWs in practice: the implementation of actuator controller needs to be simplified to cope with the difficulties and inconveniences posed by the sophisticated structure of ATBMWs.

1.4 Aims and Objectives

The aim of our research is to simplify the implementation of actuator controllers on ATBMWs by means of integrating an observer for unknown-input estimation into an existing servo controller. Objectives include:

(1) Design and build an ATBMW prototype that can change its camber in real time with the capacity of large-displacement shape morphing.
(2) Develop an actuator-level control scheme with an integrated unknown-input estimation component.

    An alternative approach for unknown-input estimation featuring a simple structure and straightforward design method is expected. To be specific, the new approach does not require detailed knowledge regarding unknown inputs, derivatives of measured outputs, and inversion of plant dynamics; does not restrict state observer design; and does not involve complicated parameter optimisation where a global optimum is not guaranteed.
(3) Validate the proposed approach of unknown-input estimation and the simplified scheme for actuator controller implementation via numerical simulations and experiments.

To avoid confusion with the concepts of UIO and UIDO which only estimate plant states, we use the term 'unknown-input estimator' (UIE) for the proposed approach of unknown-input estimation.

The remaining chapters in the thesis are organised as follows. Details of the ATBMW prototype are given in Chapter 2. A UIE-integrated LQG control scheme is then proposed and analysed in Chapter 3. Simulation studies on the unknown-input estimation of the proposed UIE and on actuator trajectory tracking using the UIE-integrated controller are presented in Chapter 4. Experiments in a wind tunnel are summarised and discussed in Chapter 5. Conclusions are drawn in Chapter 6.

Chapter 2

ACTIVE-TRUSS-BASED MORPHING WING

For the purpose of providing an experimental platform, an ATBMW prototype is built, with details given in this chapter. In order to determine the most appropriate length of each actuator for a given wing shape, the relation between actuator length and overall wing profile needs to be found, which is dealt with in Section 2.1. The structure and specifications of the ATBMW prototype as well as corresponding modelling based on system identification are described in Section 2.2.

2.1 Actuator Length Determination for Desired Wing Profile

As introduced in Section 1.1, a truss is statically and kinematically determinate according to Maxwell's theory (Maxwell, 1864). By replacing some or all of the elements in a truss with active members that can change their lengths, the overall shape of the structure can be changed. And more importantly, the shape morphing is determinate if the length of all elements is known. The relation between the length of actuators and corresponding truss topology (or in other words, the mapping from given variation in length of actuators to the only possible resultant nodal displacements) can be determined via finite element formulation (Austin et al., 1994, Baker and Friswell, 2009), based on a linear displacement model (Rao, 2004).

Derivations herein are for planar trusses, with the following assumptions:

- Struts are pin-jointed, centre lines of joining members intersecting at a common point, and therefore there is no bending on struts.

- All loads are applied at joints. This is to ensure that the struts are all two-force members.
- The weight of struts is negligible compared to applied loads.
- All struts are linearly elastic and subjected to infinitely small displacements (linear deformation assumption).

Neglecting the dynamic terms in the equation of motion of the overall truss yields the following static deformation relation in a global coordinate system:

$$\boldsymbol{\Gamma U} = \boldsymbol{F}_e + \boldsymbol{F}_a, \tag{2.1}$$

where $\boldsymbol{\Gamma}$ is the system stiffness matrix, $\boldsymbol{U}$ is the vector of nodal displacements, $\boldsymbol{F}_e$ is the vector of aerodynamic loads, and $\boldsymbol{F}_a$ is the vector of actuator forces.

As can be seen in Eq (2.1), actuator forces are treated as external forces exerted on nodes other than internal forces from struts. By doing so, the statically determinate structure becomes a mechanism when an actuator is in action, which is equivalent to removing the active strut from the structure (Austin et al., 1994) meanwhile applying a pair of counter-direction forces of the same magnitude on corresponding nodes along the original strut centre line. In order to maintain the structure integrity for easy implementation of the finite element method, active members in the truss are regarded as uniform struts as fixed-length ones. It is worth mentioning that the term "fixed-length" herein does not imply a rigid body but only means constant length (no length variation) in a macro scale relative to the length change of active elements. That is, a fixed-length strut may be subjected to strain under external loads, but has no strain if the external loads are equivalents of actuator forces. Given the foregoing facts and assumptions, $\boldsymbol{F}_a$ are virtual actuator forces of greater magnitude than actually required, with a virtual component for realizing the expected strain of the active element treated as a uniform elastic strut.

The strain ε and stress σ of strut e in axial direction (see Figure 2.1) are:

$$\varepsilon = \frac{q_k - q_i}{l} = \boldsymbol{\Psi q}^{(e)}, \tag{2.2}$$

$$\sigma = E\varepsilon\,, \tag{2.3}$$

where l and E are the length and Young's modulus of the strut, $\boldsymbol{\Psi} = \begin{bmatrix} -\frac{1}{l} & \frac{1}{l} \end{bmatrix}$ denotes the shape function, and $\boldsymbol{q}^{(e)} = [\,q_i \quad q_k\,]^T$ denotes the axial displacement of nodes i and k.

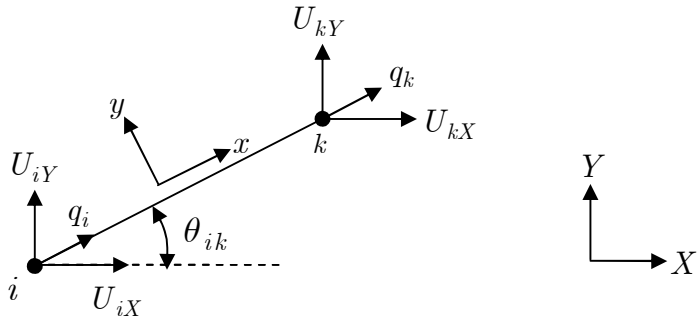

Figure 2.1: A strut in plane with local and global Cartesian coordinate systems

The stiffness matrix $\boldsymbol{\kappa}^{(e)}$ of the strut in the local coordinate system is then given by

$$\boldsymbol{\kappa}^{(e)} = \iiint_{V^{(e)}} E\boldsymbol{\Psi}^T\boldsymbol{\Psi}dV = \kappa\begin{bmatrix} 1 & -1 \\ -1 & 1 \end{bmatrix} = \frac{aE}{l}\begin{bmatrix} 1 & -1 \\ -1 & 1 \end{bmatrix}, \tag{2.4}$$

where κ, a, and V are generalised stiffness, average cross section area, and volume of the strut, respectively.

For any strut in the truss, nodal displacements $\boldsymbol{U}^{(e)}$ in the global coordinate system can be transformed into nodal displacements $\boldsymbol{q}^{(e)}$ in the local coordinate system by:

$$\boldsymbol{q}^{(e)} = \boldsymbol{\Theta}\boldsymbol{U}^{(e)}, \tag{2.5}$$

where

$$\boldsymbol{\Theta} = \begin{bmatrix} \cos\theta_{ik} & \sin\theta_{ik} & 0 & 0 \\ 0 & 0 & \cos\theta_{ik} & \sin\theta_{ik} \end{bmatrix},$$

and

$$\boldsymbol{U}^{(e)} = \begin{Bmatrix} U_{iX} \\ U_{iY} \\ U_{kX} \\ U_{kY} \end{Bmatrix}.$$

As a result, the strut stiffness matrix in the global coordinate system is

$$\begin{aligned} \boldsymbol{\Gamma}^{(e)} &= \boldsymbol{\Theta}^T \boldsymbol{\kappa}^{(e)} \boldsymbol{\Theta} \\ &= \frac{aE}{l} \begin{bmatrix} \cos^2\theta & \cos\theta\sin\theta & -\cos^2\theta & -\cos\theta\sin\theta \\ \cos\theta\sin\theta & \sin^2\theta & -\cos\theta\sin\theta & -\sin^2\theta \\ -\cos^2\theta & -\cos\theta\sin\theta & \cos^2\theta & \cos\theta\sin\theta \\ -\cos\theta\sin\theta & -\sin^2\theta & \cos\theta\sin\theta & \sin^2\theta \end{bmatrix}. \end{aligned} \tag{2.6}$$

Denote the total number of struts and nodal degrees of freedom in the truss (including the boundary and restrained degrees of freedom) by n_s and n_n, respectively. And let $\underline{\boldsymbol{\Gamma}}^{(e)}$ denote the result of expanding $\boldsymbol{\Gamma}^{(e)}$ to the dimension of $n_n \times n_n$ in the global coordinate system. Assembling strut stiffness matrices in the global coordinate system yields the overall structure stiffness matrix

$$\underset{n_n \times n_n}{\boldsymbol{\Gamma}} = \sum_{e=1}^{n_s} \underset{n_n \times n_n}{\underline{\boldsymbol{\Gamma}}^{(e)}}. \tag{2.7}$$

The actuator embedded in a strut exerts axial thrust or tension of magnitude $f_a^{(e)}$ to the nodes at both ends, corresponding to the force pair $f_{ai}^{(e)}$ and $f_{ak}^{(e)}$ of opposite directions (see Figure 2.2):

$$f_{ak}^{(e)} = f_a^{(e)}, \tag{2.8}$$

$$f_{ai}^{(e)} = -f_{ak}^{(e)} = -f_a^{(e)}. \tag{2.9}$$

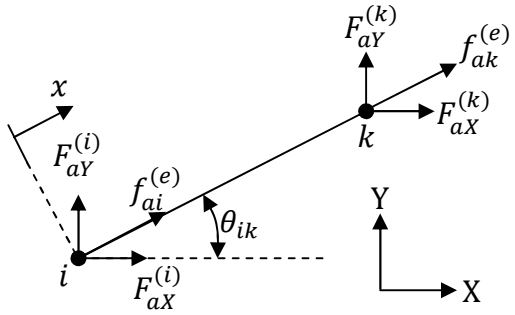

Figure 2.2: Actuator force and its discomposed components in global coordinates

Discomposed actuating forces $\boldsymbol{F}_a^{(e)}$ in the global coordinate system can be computed according to

$$\begin{cases} F_{aX}^{(i)} = f_a^{(i)} \cos\theta_{ik} = -f_a^{(e)} \cos\theta_{ik} \\ F_{aY}^{(i)} = f_a^{(i)} \sin\theta_{ik} = -f_a^{(e)} \sin\theta_{ik} \\ F_{aX}^{(k)} = f_a^{(k)} \cos\theta_{ik} = f_a^{(e)} \cos\theta_{ik} \\ F_{aY}^{(k)} = f_a^{(k)} \sin\theta_{ik} = f_a^{(e)} \sin\theta_{ik} \end{cases}, \tag{2.10}$$

or in matrix form

$$\boldsymbol{F}_a^{(e)} = \boldsymbol{T}_a^{(e)} f_a^{(e)}, \tag{2.11}$$

with

$$\boldsymbol{F}_a^{(e)} = \begin{Bmatrix} F_{aX}^{(i)} \\ F_{aY}^{(i)} \\ F_{aX}^{(k)} \\ F_{aY}^{(k)} \end{Bmatrix} \text{ and } \boldsymbol{T}_a^{(e)} = \begin{Bmatrix} -\cos\theta_{ik} \\ -\sin\theta_{ik} \\ \cos\theta_{ik} \\ \sin\theta_{ik} \end{Bmatrix}.$$

To transform the total actuator force vector $\boldsymbol{f}_a$ (of dimension $n_{fa} \times 1$) into corresponding global coordinate representation $\boldsymbol{F}_a$ (of dimension $2n_{Fa} \times 1$), we first expand vector $\boldsymbol{T}_a^{(e)}$ to an augmented matrix of dimension $n_{Fa} \times n_{fa}$, namely $\underline{\boldsymbol{T}}_a^{(e)}$, and then use the following relation:

$$\underset{n_{Fa}\times 1}{\boldsymbol{F}_a} = \underset{n_{Fa}\times n_{fa}}{\boldsymbol{T}_a}\ \underset{n_{fa}\times 1}{\boldsymbol{f}_a}\ , \tag{2.12}$$

where

$$\underset{n_{Fa}\times n_{fa}}{\boldsymbol{T}_a} = \sum_{e=1}^{n_{fa}} \underset{n_{Fa}\times n_{fa}}{\underline{\boldsymbol{T}}_a^{(e)}}\ ,\ \boldsymbol{F}_a = \begin{Bmatrix} F_{aX}^{(1)} \\ F_{aY}^{(1)} \\ \vdots \\ F_{aX}^{(n_{Fa})} \\ F_{aY}^{(n_{Fa})} \end{Bmatrix}, \text{and } \boldsymbol{f}_a = \begin{Bmatrix} f_a^{(1)} \\ f_a^{(2)} \\ \vdots \\ f_a^{(n_{fa})} \end{Bmatrix}.$$

Substitute Eq (2.12) into (2.1), then

$$\boldsymbol{\Gamma U} = \boldsymbol{F}_e + \boldsymbol{T}_a \boldsymbol{f}_a . \tag{2.13}$$

Denote the length variation of actuators by vector $\boldsymbol{q}$. As virtual work is conserved, we have

$$\boldsymbol{q} = \boldsymbol{T}_a^T \boldsymbol{U} . \tag{2.14}$$

From Eqs (2.13) and (2.14),

$$\boldsymbol{q} = \boldsymbol{T}_a^T \boldsymbol{\Gamma}^{-1} \boldsymbol{T}_a \boldsymbol{f}_a + \boldsymbol{T}_a^T \boldsymbol{\Gamma}^{-1} \boldsymbol{F}_e , \tag{2.15}$$

and hence

$$\boldsymbol{f}_a = \left(\boldsymbol{T}_a^T \boldsymbol{\Gamma}^{-1} \boldsymbol{T}_a \right)^{-1} \left(\boldsymbol{q} - \boldsymbol{T}_a^T \boldsymbol{\Gamma}^{-1} \boldsymbol{F}_e \right). \tag{2.16}$$

Substituting Eq (2.16) into (2.1) yields

$$\boldsymbol{U} = \boldsymbol{\vartheta q} + \left(\boldsymbol{I} - \boldsymbol{\vartheta T}_a^T \right) \boldsymbol{\Gamma}^{-1} \boldsymbol{F}_e , \tag{2.17}$$

where $\boldsymbol{I}$ is an identity matrix and $\boldsymbol{\vartheta} = \boldsymbol{\Gamma}^{-1} \boldsymbol{T}_a \left(\boldsymbol{T}_a^T \boldsymbol{\Gamma}^{-1} \boldsymbol{T}_a \right)^{-1}$.

Given desired nodal displacements $\boldsymbol{U}_{des}$, a possible solution for the extension of actuators, $\boldsymbol{q}_{des}$, can be calculated from

$$\boldsymbol{q}_{des} = \boldsymbol{\vartheta}^{\dagger}\left[\boldsymbol{U}_{des} - \left(\boldsymbol{I} - \boldsymbol{\vartheta}\boldsymbol{T}_a^T\right)\boldsymbol{\Gamma}^{-1}\boldsymbol{F}_e\right], \tag{2.18}$$

where $\boldsymbol{\vartheta}^{\dagger}$ is the Moore–Penrose pseudoinverse of $\boldsymbol{\vartheta}$.

Three cases apply to $\boldsymbol{\vartheta}$ according to different configuration of the active truss:

(a) $\boldsymbol{\vartheta}$ is square and nonsingular: the degrees-of-freedom (DOF) of the active truss (the number of nodal displacements) is equal to the quantity of active elements (actuators)
(b) $\boldsymbol{\vartheta}$ has more rows than columns and is not of full rank: more active elements are available than the total DOF of the active truss
(c) $\boldsymbol{\vartheta}$ is rank deficient: the total DOF of the active truss is larger than the number of active elements

Case (a) yields a unique mapping from $\boldsymbol{U}_{des}$ to $\boldsymbol{q}_{des}$. That is, any specified shape profile can be achieved exactly given that $\boldsymbol{q}_{des}$ is within the available stroke of actuators. Case (b) is an overdetermined least squares problem with infinite solutions $\boldsymbol{q}_{des}$ for $\boldsymbol{U}_{des}$, and exact shape morphing is guaranteed theoretically. The Moore–Penrose pseudoinverse of $\boldsymbol{\vartheta}$ gives a solution which minimises $\|\boldsymbol{q}_{des}\|_2$, the Euclidean length of vector $\boldsymbol{q}_{des}$, resulting evenly minimised length variation of actuators. Case (c) also has infinite solutions of $\boldsymbol{q}_{des}$ but with residuals due to insufficient actuator quantity to match desired nodal displacements. A solution with the smallest residuals $\boldsymbol{\upsilon}$ is obtained by performing the Moore–Penrose pseudoinverse of $\boldsymbol{\vartheta}$ which produces the least shape matching error.

Recalling the assumption for finite element formulation that the length variation of active element is limited to an infinitely small scale, Eq (2.18) would become invalid when large-scale shape change is required, such as camber varying from zero to 10% of chord. Significant error in $\boldsymbol{q}_{des}$ results due to the position/time-dependent variation

of the global stiffness matrix $\boldsymbol{\Gamma}$. Nonlinear finite element analysis method for large displacement problems (Wriggers, 2008) could be one of the possible solutions whereas increased complexity results. In order to continue using Eq (2.18) for large displacement situations, we discard the solution of $\boldsymbol{q}_{des}$ since it is invalid when using Eq (2.18) for large displacements. Instead, we make use of corresponding residuals $\boldsymbol{\upsilon}$ to calculate the actual nodal displacements $\boldsymbol{U}_{act}$ by $\boldsymbol{U}_{act} = \boldsymbol{U}_{des} - \boldsymbol{\upsilon}$. Given the original nodal coordinates $\boldsymbol{h}_0$, we then know the new nodal coordinates $\boldsymbol{h}_t = \boldsymbol{h}_0 + \boldsymbol{U}_{act}$. Finally, the actual extension needed for each actuator can be computed from the new coordinates of nodes.

Under large displacements, elastic deformation of fixed-length struts caused by external forces other than actuator forces can be neglected, and thus the $\boldsymbol{F}_e$ in Eq (2.1) can be set to zero, and Eq (2.18) reduces to

$$\boldsymbol{q}_{des} = \left[\boldsymbol{\Gamma}^{-1}\boldsymbol{T}_a \left(\boldsymbol{T}_a^T \boldsymbol{\Gamma}^{-1} \boldsymbol{T}_a \right)^{-1} \right]^{\dagger} \boldsymbol{U}_{des} . \tag{2.19}$$

It is worth mentioning that though the global structure stiffness matrix $\boldsymbol{\Gamma}$ appears in the foregoing derivations, it does not matter how closely it matches the actual situation, and can be selected casually or in a way that benefits subsequent computation for $\boldsymbol{q}_{des}$. Firstly, external forces $\boldsymbol{F}_e$ can be eliminated from computation in large displacement problems, where there is no need to consider the deformation in the presence of $\boldsymbol{F}_e$; Secondly, the extension of actuators are treated as virtual elastic deformation of uniform struts, with actuator forces $\boldsymbol{F}_a$ being virtual as well, and therefore it is not necessary to have exact properties of the overall strut embedded with an actuator.

The real-time optimisation of wing profile, which is tricky when there are multiple parameters defining the wing shape (Boria et al., 2009), is another subject involved in morphing wing technology research and development but not our focus at current stage, and thus not discussed herein.

2.2 ATBMW Prototype and Modelling

For experiment purpose, an ATBMW prototype is designed and built (see Figure 2.3). To achieve large-scale shape morphing, each actuator is expected to have a stroke generally longer than that of magnetostrictive and piezoelectric materials. A quick response is required, so SMA materials are not preferred. A feasible choice is to use ball-screw type linear miniature actuators, which are compact in size, light in weight, long in stroke, rigid in both axial directions, and have large force output. The structural section view of the ATBMW prototype is shown in Figure 2.3 (a), where nodes are denoted by numbers while struts are labelled with letters. Any strut can be active, but in this prototype only struts B, L, M, N, and O are each embedded with a

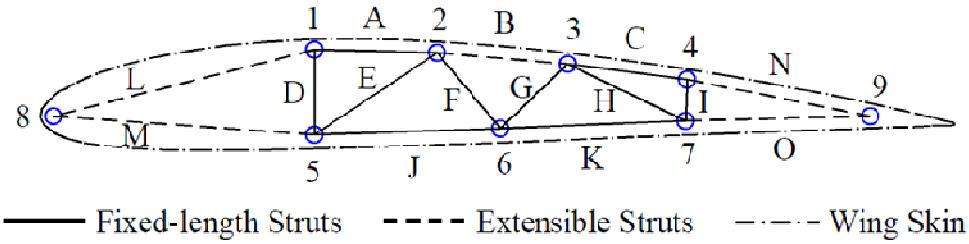

(a) Schematic of the structural configuration

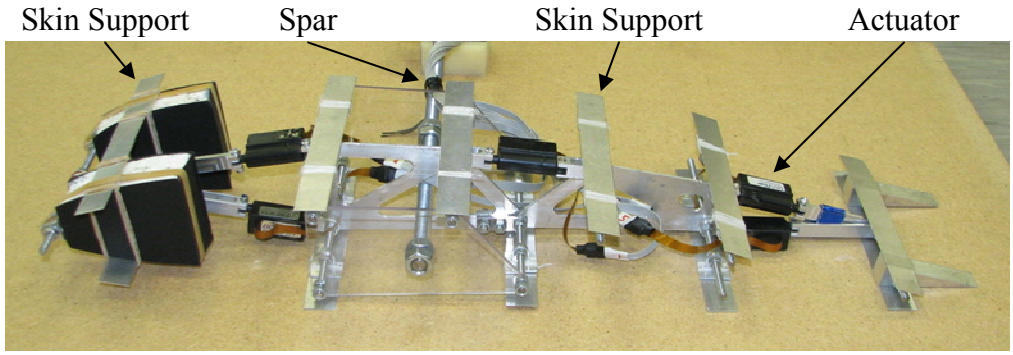

(b) Framework assembly

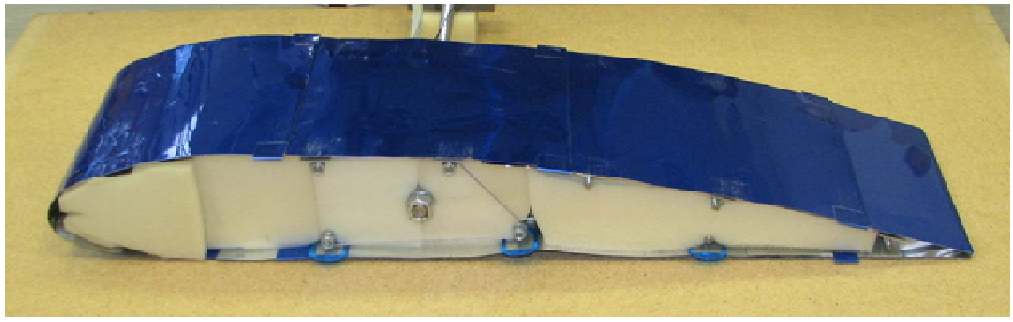

(c) Assembly with sliding aluminium skin

Figure 2.3: ATBMW prototype

Firgelli® PQ12 miniature linear actuator (see Table A.2 in Appendix A for detailed specifications). Nodes 1, 2, 5, and 6 are fixed so that the framework can be fixed to the spar (Figure 2.3 (b)). Wing skin is composed of layers of sliding aluminium sheets of 0.1mm thick (Figure 2.3 (c)). The whole wing section has a chord length of 591mm at zero camber, a maximum thickness of 71mm at 30% of chord from the leading edge, and a span of 150mm.

As mentioned in Section 1.3, it is expected that the structural dynamics of the entire prototype are not required for controller design in our approach, and a linear model considering only actuator dynamics is preferred. For investigation and comparison, models in both cases were acquired via system identification, with voltage (V) as the input and displacement/extension (mm) as the output. The iterative prediction-error minimisation method (Ljung, 1999) is used to estimate the black-box state-space model in the form of

$$\begin{cases} \boldsymbol{x}(t+t_s) = \boldsymbol{A}\boldsymbol{x}(t) + \boldsymbol{B}\boldsymbol{u}(t) + \boldsymbol{K}\boldsymbol{e}(t) \\ \boldsymbol{y}(t) = \boldsymbol{C}\boldsymbol{x}(t) + \boldsymbol{D}\boldsymbol{u}(t) + \boldsymbol{e}(t) \end{cases} \tag{2.20}$$

where $\boldsymbol{A}$, $\boldsymbol{B}$, $\boldsymbol{C}$, and $\boldsymbol{D}$ are system matrixes of appropriate dimensions; $\boldsymbol{x}(t)$, $\boldsymbol{y}(t)$, and $\boldsymbol{u}(t)$ are vectors of system state, measured output, and control input, respectively; Vector $\boldsymbol{e}(t)$ is the difference between the measured output and the predicted output of the model; $\boldsymbol{K}$ is the estimation gain matrix, and t_s is the sampling interval.

Models in Category I represent the dynamics of individual actuators (see Table 2.1) while those in Category II describe the wing structural dynamics distributed at individual actuators (see Table 2.2). The inertia loads, frictions in joints, and resistant forces from the sliding skin, as part of the dynamics of the entire wing, are all taken into account in Category II models. It is worth notice that in practice actuator dynamics are readily available whereas the dynamics of the entire wing structure are much more difficult to obtain. The prototype used in our research is primarily designed to validate the efficacy of the proposed control scheme, but not to investigate aerodynamics improvements, and therefore has a relatively simple

structure. For better aerodynamic performance, a more sophisticated framework is required, which can pose considerable difficulties in modelling through practically available methods.

Table 2.1: Models of Category I – actuator dynamics

	A	***B***	***C***	***D***
Actuator B	$\begin{bmatrix} 0 & 1 \\ 0.0006 & -14.7487 \end{bmatrix}$	$\begin{bmatrix} 0.0988 \\ 11.3646 \end{bmatrix}$	$\begin{bmatrix} 1 & 0 \end{bmatrix}$	0
Actuator L	$\begin{bmatrix} 0 & 1 \\ 0.0251 & -24.8484 \end{bmatrix}$	$\begin{bmatrix} 0.0356 \\ 25.2746 \end{bmatrix}$	$\begin{bmatrix} 1 & 0 \end{bmatrix}$	0
Actuator M	$\begin{bmatrix} 0 & 1 \\ 0.0455 & -23.6463 \end{bmatrix}$	$\begin{bmatrix} 0.0318 \\ 19.1095 \end{bmatrix}$	$\begin{bmatrix} 1 & 0 \end{bmatrix}$	0
Actuator N	$\begin{bmatrix} 0 & 1 \\ 0.4543 & -27.9472 \end{bmatrix}$	$\begin{bmatrix} 0.1379 \\ 23.3941 \end{bmatrix}$	$\begin{bmatrix} 1 & 0 \end{bmatrix}$	0
Actuator O	$\begin{bmatrix} 0 & 1 \\ 0.3867 & -16.9865 \end{bmatrix}$	$\begin{bmatrix} 0.2169 \\ 11.3852 \end{bmatrix}$	$\begin{bmatrix} 1 & 0 \end{bmatrix}$	0

Table 2.2: Models of Category II – wing structural dynamics distributed at individual actuators

	A	***B***	***C***	***D***
Actuator B	$\begin{bmatrix} 0 & 1 \\ 5.4929 & -59.6060 \end{bmatrix}$	$\begin{bmatrix} 0.1125 \\ 26.6999 \end{bmatrix}$	$\begin{bmatrix} 1 & 0 \end{bmatrix}$	0
Actuator L	$\begin{bmatrix} 0 & 1 \\ 3.3391 & -56.1780 \end{bmatrix}$	$\begin{bmatrix} -0.0479 \\ 47.0825 \end{bmatrix}$	$\begin{bmatrix} 1 & 0 \end{bmatrix}$	0
Actuator M	$\begin{bmatrix} 0 & 1 \\ 2.3486 & -40.2661 \end{bmatrix}$	$\begin{bmatrix} 0.0074 \\ 31.5277 \end{bmatrix}$	$\begin{bmatrix} 1 & 0 \end{bmatrix}$	0
Actuator N	$\begin{bmatrix} 0 & 1 \\ 0.3665 & -39.3369 \end{bmatrix}$	$\begin{bmatrix} 0.0044 \\ 24.3969 \end{bmatrix}$	$\begin{bmatrix} 1 & 0 \end{bmatrix}$	0
Actuator O	$\begin{bmatrix} 0 & 1 \\ 0.1480 & -19.3256 \end{bmatrix}$	$\begin{bmatrix} 0.2002 \\ 8.5483 \end{bmatrix}$	$\begin{bmatrix} 1 & 0 \end{bmatrix}$	0

Models identified are based on the time-domain data collected under settings as follows:

- Sampling Period: 10s
- Sampling Interval: 50ms

- Input Voltage: Rectangular pulse (7V peak amplitude; 10s period; 50% duty cycle; 0° phase shift)

The identified system models are linear and time-invariant, which are expected for ease in controller design using well-established methods. Modelling errors inevitably exist due to nonlinearities and uncertainties that present in an actual system (see Table 2.3). For example, it has been observed that nonlinear behaviours become obvious when the linear actuator operates at a relatively low voltage (e.g. lower than 3V). Furthermore, the actuator may exhibit different characteristics due to wear after a long-term use. Therefore, when only the actuator dynamics are used for controller design, the controller on an ATBMW is expected to cope with not only un-modelled wing structural dynamics and exogenous disturbances (e.g. unmeasured aerodynamic loads) but also modelling errors of actuator dynamics per se.

Table 2.3: Fits of identified models to acquired data

	Actuator B	Actuator L	Actuator M	Actuator N	Actuator O
Category I	98.18%	98.68%	98.06%	97.28%	96.75%
Category II	97.57%	98.79%	98.51%	98.46%	97.62%

Chapter 3

UIE-INTEGRATED LQG CONTROLLER

In order to simplify the implementation of actuator controllers on ATBMWs, a standard Linear-Quadratic-Gaussian (LQG) controller integrated with a new unknown-input estimator (UIE), namely, UIE-integrated LQG controller, is proposed for actuator-level control. The control problem is first clarified and stated in Section 3.1, with assumptions given. The construction of the proposed UIE-integrated LQG controller follows in Section 3.2. Finally, closed-loop analysis is presented in Section 3.3, with the mechanism of unknown-input estimation and compensation discussed, closed-loop stability confirmed, and rules for parameter selection suggested.

3.1 Problem Statements and Assumptions

The actuator-level control is discussed herein. It is a tracking problem in which the extension (axial displacement of the moving rod) of each actuator should follow the reference length specified in real time. An individual controller is proposed for each actuator, and only the extension of actuators is measured and fed back, the control problem thus is reduced to an SISO case.

The general plant model to be considered is given by

$$\begin{cases} \dot{\boldsymbol{x}}(t) = \boldsymbol{A}\boldsymbol{x}(t) + \boldsymbol{B}u(t) + \boldsymbol{B}_d\boldsymbol{d}(t) \\ y(t) = \boldsymbol{C}\boldsymbol{x}(t) \end{cases}, \tag{3.1}$$

where $u(t) \in \mathbb{R}$ is the control input; $y(t) \in \mathbb{R}$ is the measured output; $\boldsymbol{x}(t) \in \mathbb{R}^{n_x}$ is the vector of system states; $\boldsymbol{d}(t) \in \mathbb{R}^{n_d}$ describes uncertainties that the system is subject to, including uncertain, nonlinear, time-varying, and state-dependent terms, and is regarded as a vector of unknown inputs; $\boldsymbol{A} \in \mathbb{R}^{n_x \times n_x}$ is the system matrix; $\boldsymbol{C} \in \mathbb{R}^{1 \times n_x}$ is the output matrix; $\boldsymbol{B} \in \mathbb{R}^{n_x \times 1}$ is the control input matrix; $\boldsymbol{B}_d \in \mathbb{R}^{n_x \times n_d}$ is the distribution matrix of external unknown inputs; Quantities of states and unknown inputs are denoted by n_x and n_d, respectively.

The following assumptions are made:

- *Assumption 1:* $(\boldsymbol{A}, \boldsymbol{B})$ is controllable.
- *Assumption 2:* $(\boldsymbol{C}, \boldsymbol{A})$ is observable.
- *Assumption 3:* $(\boldsymbol{A}, \boldsymbol{B}, \boldsymbol{C})$ is a minimum phase system.

Note that $\boldsymbol{B}_d$ can be either known or unknown, with no rank conditions required, and there is no restriction on the number of external unknown inputs in the vector $\boldsymbol{d}(t)$. This means there can be more unknown inputs than the control inputs and the measured outputs (in our case, there are multiple unknown inputs but only one control input and one measured output). In addition, the unknown inputs may enter the system through channels different from the control input channel. When both $\boldsymbol{B}_d$ and n_d are unknown, it is difficult or even impossible to exactly predict components of $\boldsymbol{d}(t)$. Since the estimation of unknown exogenous inputs in most servo systems are for subsequent disturbance cancelation to maintain stable performance, it is possible to assume the existence of equivalent unknown inputs of the same number as control inputs which also enter the controlled plant through control input channels $\boldsymbol{B}$. This treatment is a practical and common technique in DOB as can be seen in Section 1.2.2 and the conditions for the existence of equivalent unknown inputs are theoretically discussed in the study of She et al. (2008).

According to She et al. (2008), an equivalent input exists for the unknown inputs $\boldsymbol{d}(t)$ in system (3.1) under *Assumptions 1* to *3*. Denote the equivalent unknown input by $d_e(t)$, then system (3.1) can be expressed as

$$\begin{cases} \dot{\boldsymbol{x}}(t) = \boldsymbol{A}\boldsymbol{x}(t) + \boldsymbol{B}[u(t) + d_e(t)] \\ y(t) = \boldsymbol{C}\boldsymbol{x}(t) \end{cases}. \tag{3.2}$$

Now we are able to use system (3.2) as an equivalent of (3.1), and the control problem at this point is how to estimate $d_e(t)$ to cancel $d(t)$ so that robust and improved tracking performance can be achieved on a standard state variable feedback controller.

3.2 Controller Structure

3.2.1 Overview

Our proposed controller is based on the LQG algorithm with a feed-forward proportional term as well as an integral term in the feedback path for reference tracking. The estimation of unknown inputs is integrated into the feedback loop in the form of the UIE for unknown-input compensation (see Figure 3.1).

The inclusion of the UIE is the core component that distinguishes our proposed controller from standard LQG controllers. It enables effective estimation and cancelation of unknown inputs, while only needs the measured output from the sensor and estimated output from the state observer as its inputs. Therefore, no changes are imposed on the standard LQG controller structure, which further eases the overall design process.

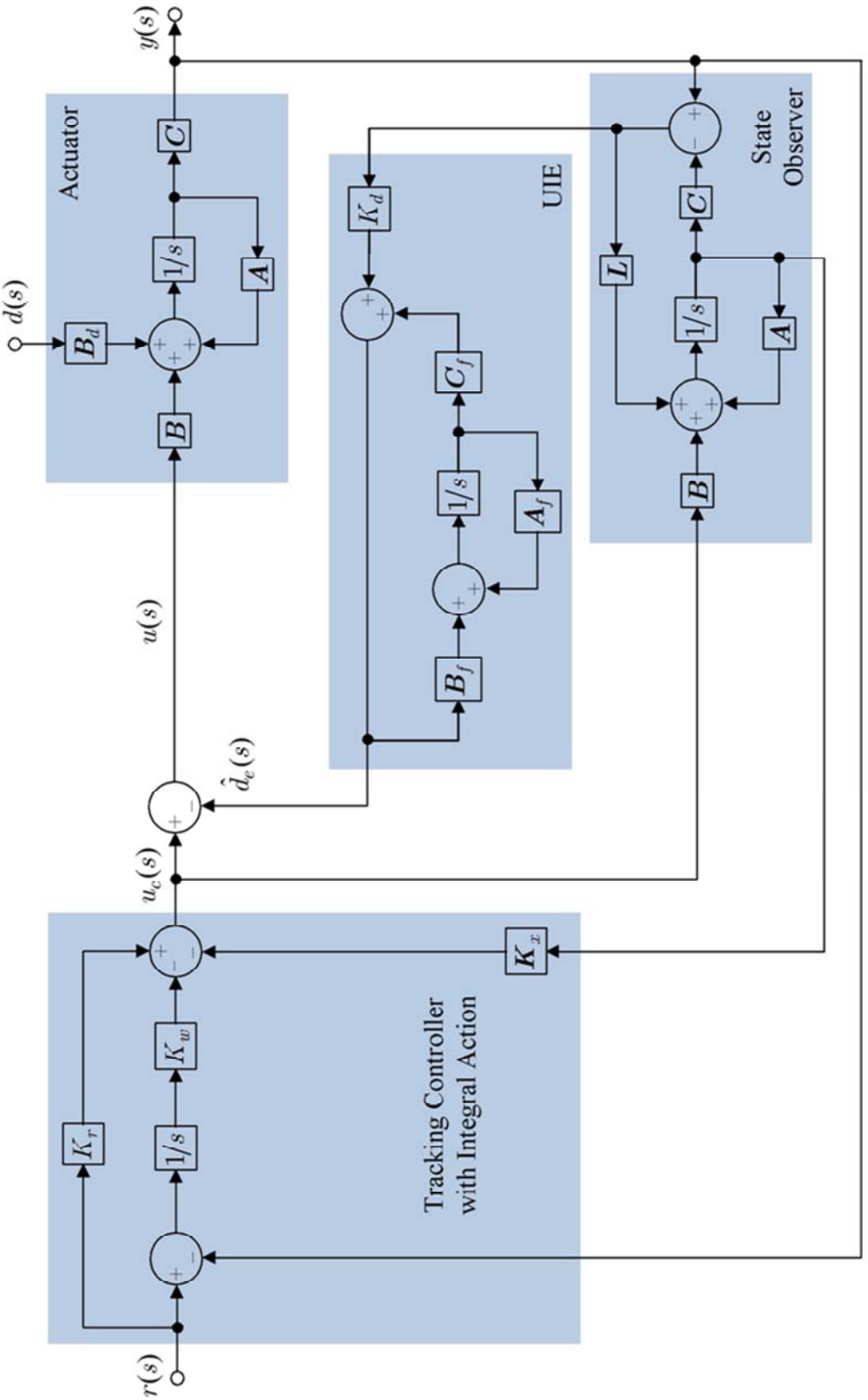

Figure 3.1: Schematic of the UIE-integrated LQG controller

3.2.2 Unknown-Input Estimator

In order to cancel the effects from unknown inputs $\boldsymbol{d}(t)$, or equivalently, $d_e(t)$, the control input $u(t)$ is defined as

$$u(t) = u_c(t) - \hat{d}_e(t), \tag{3.3}$$

where $u_c(t)$ is the normal control effort from the LQG algorithm to realise specified actuator motion when there are no disturbing inputs $\boldsymbol{d}(t)$, and $\hat{d}_e(t)$ is an estimate of the equivalent unknown input.

Now we construct $\hat{d}_e(t)$ in the following form:

$$\hat{d}_e(t) = \hat{d}_{ev}(t) + K_d\,[\,y(t) - \hat{y}(t)\,], \tag{3.4}$$

where $\hat{d}_{ev}(t)$ is an initial estimate of the equivalent unknown input, K_d is an estimation gain, and $\hat{y}(t)$ is an estimate of the plant output.

The initial estimate $\hat{d}_{ev}(t)$ is obtained and updated in real time via a low-pass filter $(\boldsymbol{A}_f, \boldsymbol{B}_f, \boldsymbol{C}_f)$ with $\hat{d}_e(t)$ as the input:

$$\begin{cases} \dot{\boldsymbol{x}}_f(t) = \boldsymbol{A}_f \boldsymbol{x}_f(t) + \boldsymbol{B}_f \hat{d}_e(t) \\ \hat{d}_{ev}(t) = \boldsymbol{C}_f \boldsymbol{x}_f(t) \end{cases}, \tag{3.5}$$

where $\boldsymbol{A}_f \in \mathbb{R}^{n_f \times n_f}$, $\boldsymbol{B}_f \in \mathbb{R}^{n_f \times 1}$, and $\boldsymbol{C}_f \in \mathbb{R}^{1 \times n_f}$ are system matrixes of the low-pass filter, while n_f denotes the quantity of filter states.

To be specific, $\left|\boldsymbol{C}_f(s\boldsymbol{I}_{n_f} - \boldsymbol{A}_f)^{-1}\boldsymbol{B}_f\right| = \left|G_f(j\omega)\right| \approx 1$ and meanwhile $\left|G_f(j\omega)\right| < 1$ for $\omega \in [\,0, \omega_c\,]$, where G_f and ω_c are the transfer function and cutoff frequency of the low-pass filter, respectively.

To obtain the estimated plant output $\hat{y}(t)$, a state observer that takes $d_e(t)$ into account is needed and constructed as

$$\begin{cases} \dot{\hat{\boldsymbol{x}}}(t) = \boldsymbol{A}\hat{\boldsymbol{x}}(t) + \boldsymbol{B}[u(t) + \hat{d}_e(t)] + \boldsymbol{L}[y(t) - \hat{y}(t)] \\ \hat{y}(t) = \boldsymbol{C}\hat{\boldsymbol{x}}(t) \end{cases}, \tag{3.6}$$

where $\boldsymbol{L} \in \mathbb{R}^{n_x \times 1}$ is the estimation gain matrix of the state observer.

Substituting $u(t)$ in (3.6) yields:

$$\begin{cases} \dot{\hat{\boldsymbol{x}}}(t) = \boldsymbol{A}\hat{\boldsymbol{x}}(t) + \boldsymbol{B}u_c(t) + \boldsymbol{L}[y(t) - \hat{y}(t)] \\ \hat{y}(t) = \boldsymbol{C}\hat{\boldsymbol{x}}(t) \end{cases}. \tag{3.7}$$

Apparently, Eq (3.7) is a standard form of the state observer in the LQG controller. Hence, the estimated output from the state observer of the LQG controller can be directly used as the input of the UIE. In summary, Eqs (3.4) and (3.5) form the proposed UIE.

3.2.3 LQG Controller

The inclusion of a UIE in an existing LQG controller results in the control effort given by Eq (3.3). Assume that unknown inputs are ideally cancelled by $\hat{d}_e(t)$, then standard LQG design procedures can be followed (Burl, 1998, Franklin et al., 2010).

As can be seen in Figure 3.1, an internal model of first order (integral action) rather than higher order is included for reference tracking. Generally, for situations where reference trajectories are known beforehand and have fixed patterns, an accurate representation of these trajectories using the internal model of an appropriate order can enable robust tracking. When optimal wing profiles are not predetermined offline but updated online according to the real-time variation of aerodynamic conditions, using a higher-order internal model is not recommended though, in consideration of the complexity to model patterns of wing profile variation. This is because aerodynamic conditions as well as corresponding optimal or suboptimal wing profiles are subject to substantially random variations. Even though flight data can be

acquired for further analysis, the consistency of every flight is not guaranteed. As a simple and straightforward solution, the combination of a feed-forward proportional term and a 1st-order internal model (integral term), which has better trajectory following capability than merely an integral action, is recommended in this case.

For convenience in the close-loop analysis in the next section, the 1st-order internal model is not formulated following the normal convention (Francis and Wonham, 1975), but derived on the integral action base.

Denote the target length of an actuator by $r(t)$ and let $\dot{x}_w(t) = r(t) - y(t)$, then

$$\dot{x}_w(t) = r(t) - C\boldsymbol{x}(t), \tag{3.8}$$

and the augmented system based on (3.2) with states in error space is

$$\begin{bmatrix} \dot{\boldsymbol{x}}(t) \\ \dot{x}_w(t) \end{bmatrix} = \begin{bmatrix} \boldsymbol{A} & 0 \\ -\boldsymbol{C} & 0 \end{bmatrix} \begin{bmatrix} \boldsymbol{x}(t) \\ x_w(t) \end{bmatrix} + \begin{bmatrix} \boldsymbol{B} \\ 0 \end{bmatrix} u_c(t) + \begin{bmatrix} \boldsymbol{0} \\ r(t) \end{bmatrix}, \tag{3.9}$$

or in a compact form

$$\dot{\boldsymbol{\eta}}(t) = \tilde{\boldsymbol{A}}\boldsymbol{\eta}(t) + \tilde{\boldsymbol{B}}u_c(t) + \tilde{\boldsymbol{r}}(t), \tag{3.10}$$

where $\boldsymbol{\eta}(t) = \begin{bmatrix} \boldsymbol{x}(t) \\ x_w(t) \end{bmatrix}$, $\tilde{\boldsymbol{A}} = \begin{bmatrix} \boldsymbol{A} & 0 \\ -\boldsymbol{C} & 0 \end{bmatrix}$, $\tilde{\boldsymbol{B}} = \begin{bmatrix} \boldsymbol{B} \\ 0 \end{bmatrix}$, and $\tilde{\boldsymbol{r}}(t) = \begin{bmatrix} \boldsymbol{0} \\ r(t) \end{bmatrix}$.

Define a performance index as

$$J = \int_0^\infty \left[\boldsymbol{\eta}^T(t)\boldsymbol{Q}_\eta\boldsymbol{\eta}(t) + R_\eta u_c^2(t) \right] dt, \tag{3.11}$$

where $\boldsymbol{Q}_\eta = \begin{bmatrix} \boldsymbol{C^T}Q_y\boldsymbol{C} & 0 \\ 0 & Q_w \end{bmatrix}$ with Q_y and Q_w being weightings for the tracking error and its integral, and R_η is the weighting for the control input.

Given the feedback

$$u_c(t) = -\tilde{\boldsymbol{K}}\boldsymbol{\eta}(t) + K_r r(t)\,, \tag{3.12}$$

the index in Eq (3.11) is minimised when $\tilde{\boldsymbol{K}} = R_\eta^{-1}\tilde{\boldsymbol{B}}^T\tilde{\boldsymbol{\Phi}}$, with $\tilde{\boldsymbol{\Phi}}$ as the solution to the algebraic Riccati equation

$$\tilde{\boldsymbol{A}}^T\tilde{\boldsymbol{\Phi}} + \tilde{\boldsymbol{\Phi}}\tilde{\boldsymbol{A}} - \tilde{\boldsymbol{\Phi}}\tilde{\boldsymbol{B}}R_\eta^{-1}\tilde{\boldsymbol{B}}^T\tilde{\boldsymbol{\Phi}} + \tilde{\boldsymbol{Q}}_\eta = 0\,,$$

with

$$K_r = \left[\, Z_2 - \boldsymbol{W}_1\boldsymbol{C}^T Q_y \,\right], \tag{3.13}$$

where

$$\boldsymbol{W} = R_\eta^{-1}\tilde{\boldsymbol{B}}^T\left[\left(\tilde{\boldsymbol{A}} - \tilde{\boldsymbol{B}}\tilde{\boldsymbol{K}}\right)^T\right]^{-1} = [\,\boldsymbol{W}_1 \mid W_2\,],$$
$$\boldsymbol{Z} = R_\eta^{-1}\tilde{\boldsymbol{B}}^T\left[\left(\tilde{\boldsymbol{A}} - \tilde{\boldsymbol{B}}\tilde{\boldsymbol{K}}\right)^T\right]^{-1}\tilde{\boldsymbol{\Phi}} = [\,\boldsymbol{Z}_1 \mid Z_2\,].$$

Let $\tilde{\boldsymbol{K}} = [\,\boldsymbol{K}_x \quad K_w\,]$, then from Eq (3.12),

$$u_c(t) = -\boldsymbol{K}_x\boldsymbol{x}(t) - K_w x_w(t) + K_r r(t)\,. \tag{3.14}$$

Now replace $\boldsymbol{x}(t)$ by an estimate $\hat{\boldsymbol{x}}(t)$ obtained from a linear-quadratic optimal state observer

$$\begin{cases} \dot{\hat{\boldsymbol{x}}}(t) = A\hat{\boldsymbol{x}}(t) + \boldsymbol{B}\boldsymbol{u}_c(t) + \boldsymbol{L}[\,y(t) - \hat{y}(t)\,] \\ \hat{y}(t) = \boldsymbol{C}\hat{\boldsymbol{x}}(t) \end{cases}, \tag{3.15}$$

then

$$u_c(t) = -\boldsymbol{K}_x\hat{\boldsymbol{x}}(t) - K_w x_w(t) + K_r r(t)\,, \tag{3.16}$$

where $\boldsymbol{K}_x$, K_w, and K_r are gains for proportional state feedback, 1st-order internal model, and feed-forward proportional term, respectively.

3.3 Closed-Loop Analysis

3.3.1 Estimation and Suppression of Unknown Inputs

Since we are able to use system (3.2) as an equivalent of (3.1), the mechanism of estimating and suppressing unknown inputs can be revealed by the relation between the equivalent unknown input $d_e(t)$ and the system output $y(t)$ in system (3.2).

From Figure 3.1 and according to system (3.2),

$$y(s) = P_n(s)[u(s) + d_e(s)], \tag{3.17}$$

where $P_n(s)$ represents the nominal plant model.

Define $G_w(s)$ as the transfer function of the integral action in the 1st-order internal model and rewrite Eq (3.16) in frequency domain as

$$u_c(s) = -\boldsymbol{K}_{\boldsymbol{x}}\hat{\boldsymbol{x}}(s) - K_w G_w(s)[r(s) - y(s)] + K_r r(s). \tag{3.18}$$

Substitute $u_c(s)$ in (3.7), and define $\boldsymbol{G}_{yx}(s)$ as the transfer matrix from $y(s)$ to $\hat{\boldsymbol{x}}(s)$. When $r(s) = 0$, then:

$$\begin{aligned} \hat{\boldsymbol{x}}(s) &= \left(s\boldsymbol{I}_{n_x} - \boldsymbol{A} + \boldsymbol{B}\boldsymbol{K}_x + \boldsymbol{L}\boldsymbol{C}\right)^{-1}[\boldsymbol{B}K_w G_w(s) + \boldsymbol{L}]y(s) \\ &= \boldsymbol{G}_{yx}(s)y(s) \end{aligned}, \tag{3.19}$$

From Eqs (3.4) and (3.5), we have:

$$\hat{d}_{ev}(s) = \boldsymbol{C}_f(s\boldsymbol{I}_{n_f} - \boldsymbol{A}_f)^{-1}\boldsymbol{B}_f\hat{d}_e(s) = G_f(s)\hat{d}_e(s), \tag{3.20}$$

$$\begin{aligned}\hat{d}_e(s) &= \left[1 - G_f(s)\right]^{-1} K_d \left[y(s) - \hat{y}(s)\right] \\ &= G_{yd}(s)\left[y(s) - \hat{y}(s)\right]\end{aligned}, \tag{3.21}$$

where $G_{yd}(s)$ is the transfer function from $\left[y(s) - \hat{y}(s)\right]$ to $\hat{d}_e(s)$.

According to Eqs (3.3), (3.17) to (3.19), and (3.21), the closed-loop system with $d_e(s)$ as the input is

$$y(s) = P_n(s)\left[1 + H(s)P_n(s)\right]^{-1} d_e(s), \tag{3.22}$$

where $H(s) = \boldsymbol{K}_x \boldsymbol{G}_{yx}(s) - K_w G_w(s) + G_{yd}(s)\left[1 - \boldsymbol{C}\boldsymbol{G}_{yx}(s)\right]$.

As a result, the sensitivity of the closed-loop system is

$$S(s) = \frac{1}{1 + H(s)P_n(s)}. \tag{3.23}$$

Equations (3.22) and (3.23) indicate that, for a given $P_n(s)$ and an existing properly designed LQG controller, having $H(s)$ large enough over the range of frequencies which characterise the unknown inputs such that $H(s)P_n(s) \gg 1$ can further reduce the system sensitivity. A much smaller system sensitivity can significantly improve the suppression of the effects from unknown inputs, and this can be achieved by an appropriate design of $G_{yd}(s)$. In other words, if a $G_{yd}(s)$ exists so that $H(s)$ is sufficiently large, an estimate of adequate accuracy on the equivalent unknown input is then obtained, and the feedback of this estimate into the system counteracts the actual unknown inputs, alleviating disturbances.

Since $\left|G_f(j\omega)\right| \approx 1$ and $\left|G_f(j\omega)\right| < 1$ for $\omega \in [0, \omega_c]$, then we have a large $\left|G_{yd}(j\omega)\right|$, and thus a large $\left|H(j\omega)\right|$ for frequencies within $(0, \omega_c)$. As a result, $y(t) \approx 0$ when $t \to \infty$. This means, though $\left\|S(j\omega)\right\|_\infty$ cannot be minimised ideally for $\omega \in [0, \infty)$, the introduction of a low-pass filter suffices when the frequency of unknown inputs to be suppressed is below ω_c.

To avoid confusion, we especially defined $\Delta y(s)$ as the error between the disturbed output and undisturbed output. That is, $y(t) \approx 0$ in Eq (3.22) means $\Delta y(s) \approx 0$ which, from the point of view of an open-loop system, is equivalently to $\Delta y(s) = P_n(s)\left[d_e(s) - \hat{d}_e(s)\right] \approx 0$, leading to $\hat{d}_e(s) \approx d_e(s)$.

The mechanism of estimating and rejecting unknown inputs can be further explained by isolating the UIE and the state observer from the controller, as shown in Figure 3.2.

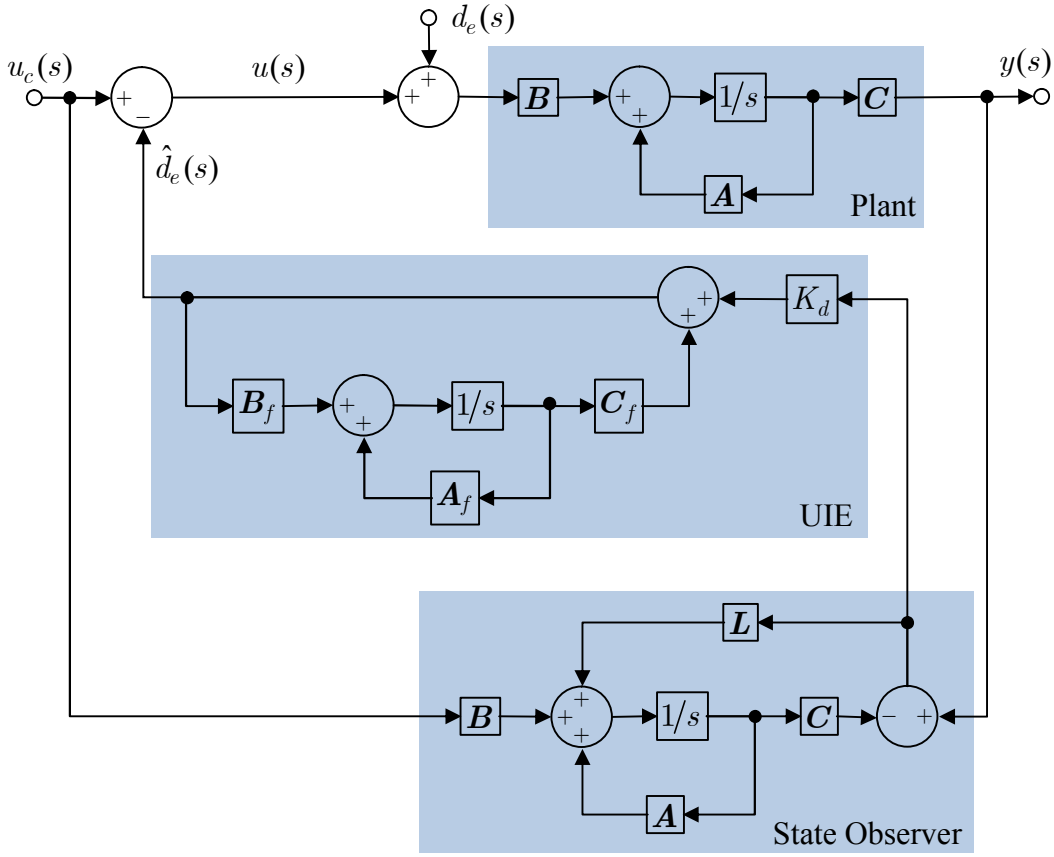

Figure 3.2: Schematic of the proposed UIE isolated from the controller

Let $u_c(t) = 0$, then $u(t) = -\hat{d}_e(t)$. From Eq (3.7),

$$\hat{y}(s) = \boldsymbol{C}(s\boldsymbol{I}_{n_x} - \boldsymbol{A} + \boldsymbol{LC})^{-1}\boldsymbol{L}y(s) = G_{yy}(s)y(s), \tag{3.24}$$

and according to Eqs (3.3), (3.17), (3.21), and (3.24),

$$\begin{aligned} y(s) &= P_n(s)\left\{1 + G_{yd}(s)\left[1 - G_{yy}(s)\right]P_n(s)\right\}^{-1} d_e(s) \\ &= H_d(s) d_e(s) \end{aligned}, \tag{3.25}$$

where $G_{yy}(s)$ and $H_d(s)$ are the transfer function of corresponding input-output pairs, respectively.

Equation (3.25) indicates that minimising $\|H_d(s)\|_\infty$ can effectively suppress the effects from unknown inputs, which can be achieved by manipulating $G_{yd}(s)$. In other words, if a proper $G_{yd}(s)$ exists so that $\|H_d(s)\|_\infty$ is sufficiently small, then $y(s) \approx 0$ for $t \to \infty$. Clearly, $y(s) = P_n(s)\left[d_e(s) - \hat{d}_e(s)\right]$ in this isolated form in Figure 3.2, and it is manifest that $\hat{d}_e(s) \approx d_e(s)$ at steady state.

3.3.2 Controller Stability

With an UIE integrated, the following theorem holds for the stability of the overall controller.

Theorem: If system (3.1) with any initial condition $\boldsymbol{x}(t_0)$ under *Assumptions 1* to *3* is stabilised by the control input in Eq (3.14) with full-state feedback (no state observer and no UIE) when $\boldsymbol{d}(t) = 0$, then system (3.1) remains stable with the control law in Eq (3.3) when subjected to any unknown inputs $\boldsymbol{d}(t) \in \mathbb{R}^{n_d}$ of frequencies over the range of $\Omega \in [0, \omega_c]$ including un-modelled dynamics $M(s)$, given that the following conditions are satisfied:

(a) $\left|G_f(j\omega)\right| \approx 1$ and $\left|G_f(j\omega)\right| < 1$ for $\omega \in [0, \omega_c]$.

(b) $\boldsymbol{L} \in \mathbb{R}^{n_x \times 1}$ and $K_d \in \mathbb{R}^+$ are selected such that $(\boldsymbol{A} - \boldsymbol{LC} - \boldsymbol{B}K_d\boldsymbol{C})$ is stable, and

$$\left|M(j\omega)\right| < \left|1 + \frac{1}{H(j\omega)P_n(j\omega)}\right|, \ \forall \omega \in [0, +\infty).$$

Proof: As discussed in Section 3.1, an equivalent unknown input exists for system (3.1), and therefore system (3.2) is used in the proof.

According to Eqs (3.2) to (3.5),

$$\begin{aligned}\dot{\boldsymbol{x}}(t) &= \boldsymbol{A}\boldsymbol{x}(t) + \boldsymbol{B}u_c(t) + \boldsymbol{B}\left[d_e(t) - \hat{d}_e(t)\right] \\ &= \boldsymbol{A}\boldsymbol{x}(t) + \boldsymbol{B}u_c(t) - \boldsymbol{B}\hat{d}_{ev}(t) - \boldsymbol{B}K_d\left[y(t) - \hat{y}(t)\right] + \boldsymbol{B}d_e(t) \\ &= \boldsymbol{A}\boldsymbol{x}(t) + \boldsymbol{B}u_c(t) - \boldsymbol{B}\boldsymbol{C}_f\boldsymbol{x}_f(t) - \boldsymbol{B}K_d\boldsymbol{C}\left[\boldsymbol{x}(t) - \hat{\boldsymbol{x}}(t)\right] + \boldsymbol{B}d_e(t).\end{aligned} \tag{3.26}$$

Subtract Eq (3.7) from (3.26), and let $\boldsymbol{e}_x(t) = \boldsymbol{x}(t) - \hat{\boldsymbol{x}}(t)$, then

$$\dot{\boldsymbol{e}}_x(t) = (\boldsymbol{A} - \boldsymbol{L}\boldsymbol{C} - \boldsymbol{B}K_d\boldsymbol{C})\boldsymbol{e}_x(t) - \boldsymbol{B}\boldsymbol{C}_f\boldsymbol{x}_f(t) + \boldsymbol{B}d_e(t). \tag{3.27}$$

Substituting Eq (3.16) for $u_c(t)$ in Eq (3.26) with $\hat{\boldsymbol{x}}(t) = \boldsymbol{x}(t) - \boldsymbol{e}_x(t)$ yields

$$\begin{aligned}\dot{\boldsymbol{x}}(t) = (\boldsymbol{A} - \boldsymbol{B}\boldsymbol{K}_x)\boldsymbol{x}(t) - \boldsymbol{B}K_w x_w(t) + (\boldsymbol{B}\boldsymbol{K}_x - \boldsymbol{B}K_d\boldsymbol{C})\boldsymbol{e}_x \\ - \boldsymbol{B}\boldsymbol{C}_f\boldsymbol{x}_f(t) + \boldsymbol{B}K_r r(t) + \boldsymbol{B}d_e(t).\end{aligned} \tag{3.28}$$

From Eqs (3.4) and (3.5),

$$\begin{aligned}\dot{\boldsymbol{x}}_f(t) &= \boldsymbol{A}_f\boldsymbol{x}_f(t) + \boldsymbol{B}_f\left\{\hat{d}_{ev} + K_d\left[y(t) - \hat{y}(t)\right]\right\} \\ &= (\boldsymbol{A}_f + \boldsymbol{B}_f\boldsymbol{C}_f)\boldsymbol{x}_f(t) + \boldsymbol{B}_f K_d\boldsymbol{C}\boldsymbol{e}_x(t)\end{aligned}. \tag{3.29}$$

Write Eqs (3.8), (3.27), (3.28), and (3.29) in matrix form, then

$$\begin{bmatrix}\dot{\boldsymbol{x}}(t) \\ \dot{x}_w(t) \\ \dot{\boldsymbol{e}}_x(t) \\ \dot{\boldsymbol{x}}_f(t)\end{bmatrix} = \begin{bmatrix}\boldsymbol{A} - \boldsymbol{B}\boldsymbol{K}_x & -\boldsymbol{B}K_w & \boldsymbol{B}\boldsymbol{K}_x - \boldsymbol{B}K_d\boldsymbol{C} & -\boldsymbol{B}\boldsymbol{C}_f \\ -\boldsymbol{C} & 0 & 0 & 0 \\ 0 & 0 & \boldsymbol{A} - \boldsymbol{L}\boldsymbol{C} - \boldsymbol{B}K_d\boldsymbol{C} & -\boldsymbol{B}\boldsymbol{C}_f \\ 0 & 0 & \boldsymbol{B}_f K_d\boldsymbol{C} & \boldsymbol{A}_f + \boldsymbol{B}_f\boldsymbol{C}_f\end{bmatrix}\begin{bmatrix}\boldsymbol{x}(t) \\ x_w(t) \\ \boldsymbol{e}_x(t) \\ \boldsymbol{x}_f(t)\end{bmatrix} + \begin{bmatrix}\boldsymbol{B}K_r \\ 1 \\ 0 \\ 0\end{bmatrix} r(t) + \begin{bmatrix}\boldsymbol{B} \\ 0 \\ \boldsymbol{B} \\ 0\end{bmatrix} d_e(t). \tag{3.30}$$

With appropriate matrix partitioning, it is clear that the characteristic equation associated with Eq (3.30) is

$$
\begin{aligned}
&\det\left[\begin{array}{cc|cc} s\boldsymbol{I}-(\boldsymbol{A}-\boldsymbol{B}\boldsymbol{K}_x) & \boldsymbol{B}K_w & -(\boldsymbol{B}\boldsymbol{K}_x-\boldsymbol{B}K_d\boldsymbol{C}) & \boldsymbol{B}\boldsymbol{C}_f \\ \boldsymbol{C} & s & 0 & 0 \\ \hline 0 & 0 & s\boldsymbol{I}-(\boldsymbol{A}-\boldsymbol{L}\boldsymbol{C}-\boldsymbol{B}K_d\boldsymbol{C}) & \boldsymbol{B}\boldsymbol{C}_f \\ 0 & 0 & -\boldsymbol{B}_fK_d\boldsymbol{C} & s\boldsymbol{I}-(\boldsymbol{A}_f+\boldsymbol{B}_f\boldsymbol{C}_f) \end{array}\right] \\
&= \det\left[\begin{array}{cc} s\boldsymbol{I}-(\boldsymbol{A}-\boldsymbol{B}\boldsymbol{K}_x) & \boldsymbol{B}K_w \\ \boldsymbol{C} & s \end{array}\right] \\
&\quad\cdot\det\left[\begin{array}{cc} s\boldsymbol{I}-(\boldsymbol{A}-\boldsymbol{L}\boldsymbol{C}-\boldsymbol{B}K_d\boldsymbol{C}) & \boldsymbol{B}\boldsymbol{C}_f \\ -\boldsymbol{B}_fK_d\boldsymbol{C} & s\boldsymbol{I}-(\boldsymbol{A}_f+\boldsymbol{B}_f\boldsymbol{C}_f) \end{array}\right] \\
&= \det\left[\begin{array}{cc} s\boldsymbol{I}-(\boldsymbol{A}-\boldsymbol{B}\boldsymbol{K}_x) & \boldsymbol{B}K_w \\ \boldsymbol{C} & s \end{array}\right]\cdot\det[s\boldsymbol{I}-(\boldsymbol{A}-\boldsymbol{L}\boldsymbol{C}-\boldsymbol{B}K_d\boldsymbol{C})] \\
&\quad\cdot\det\left[s\boldsymbol{I}-(\boldsymbol{A}_f+\boldsymbol{B}_f\boldsymbol{C}_f)+\boldsymbol{B}_fK_d\boldsymbol{C}[s\boldsymbol{I}-(\boldsymbol{A}-\boldsymbol{L}\boldsymbol{C}-\boldsymbol{B}K_d\boldsymbol{C})]^{-1}\boldsymbol{B}\boldsymbol{C}_f\right] \\
&= \det\left[\begin{array}{cc} s\boldsymbol{I}-(\boldsymbol{A}-\boldsymbol{B}\boldsymbol{K}_x) & \boldsymbol{B}K_w \\ \boldsymbol{C} & s \end{array}\right]\cdot\det[s\boldsymbol{I}-(\boldsymbol{A}-\boldsymbol{L}\boldsymbol{C}-\boldsymbol{B}K_d\boldsymbol{C})] \\
&\quad\cdot\det\left[s\boldsymbol{I}-\boldsymbol{A}_f-\boldsymbol{B}_f\left\{1-K_d\boldsymbol{C}[s\boldsymbol{I}-(\boldsymbol{A}-\boldsymbol{L}\boldsymbol{C}-\boldsymbol{B}K_d\boldsymbol{C})]^{-1}\boldsymbol{B}\right\}\boldsymbol{C}_f\right]=0.
\end{aligned}
\tag{3.31}
$$

If system (3.1) with any initial condition $\boldsymbol{x}(t_0)$ is stabilised by the control input in Eq (3.14) with full-state feedback (no state observer and no UIE) when $\boldsymbol{d}(t)=0$, it is a case of standard linear-quadratic control with integral action, the characteristic equation of which, according to Eq (3.9), is:

$$
\det\left[\begin{array}{cc} s\boldsymbol{I}-(\boldsymbol{A}-\boldsymbol{B}\boldsymbol{K}_x) & \boldsymbol{B}K_w \\ \boldsymbol{C} & s \end{array}\right]=0. \tag{3.32}
$$

It is evident that the roots of Eq (3.32), which lie in the left half-plane, are also part of the roots of Eq (3.31). If a proper $\boldsymbol{L}\in\mathbb{R}^{n_x\times 1}$ and $K_d\in\mathbb{R}^+$ are selected such that $(\boldsymbol{A}-\boldsymbol{L}\boldsymbol{C}-\boldsymbol{B}K_d\boldsymbol{C})$ is stable, and the low-pass filter satisfies condition (a), then all roots of Eq (3.31) are in the left half-plane. Under *Assumption 2* in Section 3.1, such an $\boldsymbol{L}$ and K_d exist.

Upon the absolute stability discussed, we need to consider the relative stability in the presence of un-modelled dynamics $M(s)$. As illustrated in Figure 3.3, the relation between the nominal plant model $P_n(s)$ and actual process $P(s)$ is given by

$$P(s) = P_n(s)[1 + M(s)]. \tag{3.33}$$

An equivalent block diagram depiction for the system in Figure 3.3 is given in Figure 3.4. According to the small-gain theorem (Vidyasagar, 1978), the closed-loop system is stable if

$$|M(j\omega)|\left|\frac{H(j\omega)P_n(j\omega)}{1 + H(j\omega)P_n(j\omega)}\right| < 1,\ \forall\omega \in [0, +\infty), \tag{3.34}$$

or equivalently,

$$|M(j\omega)| < \left|1 + \frac{1}{H(j\omega)P_n(j\omega)}\right|,\ \forall\omega \in [0, +\infty). \tag{3.35}$$

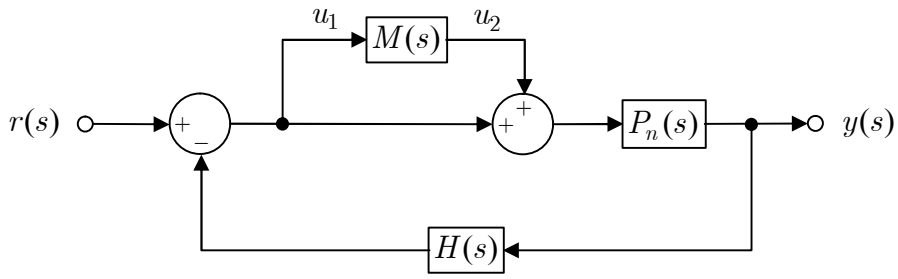

Figure 3.3: Un-modelled dynamics $M(s)$ in the closed-loop system

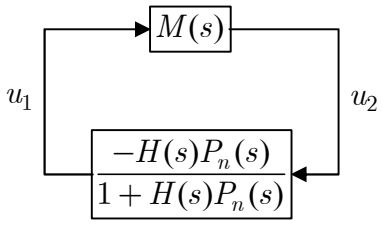

Figure 3.4: Equivalent block diagram depiction of the closed-loop system with un-modelled dynamics $M(s)$

Remark 1: As indicated by the closed-loop dynamics in Eq (3.31), the separation principle still holds for the full-state feedback design and state observer design despite the inclusion of the UIE.

Remark 2: From Eqs (3.5) and (3.27), the dynamics of state estimation are given by

$$\dot{\boldsymbol{e}}_x(t) = (\boldsymbol{A} - \boldsymbol{L}\boldsymbol{C} - \boldsymbol{B}K_d\boldsymbol{C})\boldsymbol{e}_x(t) + \boldsymbol{B}\xi(t), \tag{3.36}$$

where $\xi(t) = d_e(t) - \hat{d}_{ev}(t)$.

As shown in (3.36), state estimation of adequate accuracy is ensured by the integration of UIE, with the estimation error subjected only to the residual equivalent unknown input $\xi(t) \approx 0$ as $t \to \infty$. The advantage of integrating a UIE into an existing LQG controller is that, it enables better state estimation performance in the presence of unknown inputs that are non-Gaussian, meanwhile retains the merits of an optimal state observer in terms of sensor noise filtering.

Remark 3: Unlike the scheme in the study of She et al. (2008), some relative independence in state observer design is retained in our proposed controller though dynamics of the state observer is associated with the UIE component. Since an additional parameter K_d gives a second degree of freedom in UIE design, the performance of the UIE component is then not totally dependent on the state observer gain, thus imposing less constraint on the state observer design.

3.3.3 Controller Parameters Selection

As shown in Section 3.3.2, the design of the full-state feedback control law is independent of the UIE component and can be conducted separately prior to the UIE design according to desired performance specifications. Given that design procedures for the optimal full-state feedback control are well established in literature, corresponding details are not repeated herein. In this subsection, guidelines for selecting parameters associated with the UIE are given. These parameters include the state observer gain $\boldsymbol{L}$, the UIE gain K_d, and the low-pass filter $(\boldsymbol{A}_f, \boldsymbol{B}_f, \boldsymbol{C}_f)$ or $G_f(s)$.

(1) State observer gain $\boldsymbol{L}$ and UIE gain K_d

According to condition (b) in the *Theorem* in Section 3.3.2, both $\boldsymbol{L}$ and K_d contribute to the stability of $(\boldsymbol{A}-\boldsymbol{LC}-\boldsymbol{B}K_d\boldsymbol{C})$, so the first priority is to design $\boldsymbol{L}$ such that the state observer functions normally to provide estimated states for the linear-quadratic state feedback control. Under *Assumption 2* in Section 3.1, such an $\boldsymbol{L}$ exists.

Upon the absolute stability of $(\boldsymbol{A}-\boldsymbol{LC}-\boldsymbol{B}K_d\boldsymbol{C})$, the inequality in (3.35) needs to be satisfied in order to ensure stability robustness. Therefore, a smaller $H(s)$ is desired, with a larger gain $\boldsymbol{L}$ expected in accordance to Eq (3.19). Since the un-modelled dynamics $M(s)$ are not exactly known or even completely unknown, a safe design can be based simply on assuming $M(s)=1$. To be specific,

$$\left|1+\frac{1}{H(j\omega)P_n(j\omega)}\right|>1,\ \forall\omega\in[0,+\infty). \tag{3.37}$$

However, un-modelled dynamics in practical applications are normally much less severe, that is, $|M(j\omega)|\approx 1$ for only a limited frequency range while $|M(j\omega)|\ll 1$ elsewhere. Therefore, an index β for the stability robustness of the closed-loop system is defined as:

$$\beta=\min\left|1+\frac{1}{H(j\omega)P_n(j\omega)}\right|-1,\ \forall\omega\in[0,+\infty), \tag{3.38}$$

Different to the criterion in (3.35), it is normal to have a negative value for β due to the pessimistic assumption on $M(s)$. Thus, a negative value of β does not necessarily indicates an unstable system subjected to parameter variations in the plant. The closed-loop system is said to have better stability robustness when β is larger. As long as an $\boldsymbol{L}$ is designed to have β large enough to produce an adequate level of stability robustness that covers most possible uncertainties, the closed-loop system remains stable in spite of the un-modelled dynamics. Since an appropriate

minimum value that β is allowed to reach depends largely on real world applications and varies among cases, a specific standard is not given herein. An example of the controller design using the index β is presented in the next chapter in Section 4.1.2.

As the state observer gain plays an important role in ensuring the stability of the overall close-loop system and needs to be tuned by referring to the stability robustness index, the power spectrum of zero-mean Gaussian noise processes assumed in design may not accurately describe the noise statistics. As a result, it is more convenient and straightforward to design the state observer gain on the basis of the duality between the linear quadratic regulator (LQR) and the optimal linear filter. Assume that unknown inputs are ideally cancelled, then according to the well-established linear-quadratic optimal design method we have the corresponding dual system

$$\dot{\boldsymbol{e}}_x(t) = (\boldsymbol{A}^T - \boldsymbol{C}^T \boldsymbol{L}^T)^T \boldsymbol{e}_x(t)\,. \tag{3.39}$$

This is to select $\boldsymbol{L}^T$ that minimises the performance index

$$J_l = \int_0^\infty \left\{ \boldsymbol{e}_x^T(t) \boldsymbol{Q}_l \boldsymbol{e}_x(t) + \left[-\boldsymbol{L}^T \boldsymbol{e}_x(t) \right]^T R_l \left[-\boldsymbol{L}^T \boldsymbol{e}_x(t) \right] \right\} dt\,, \tag{3.40}$$

where $\boldsymbol{Q}_l$ is a symmetric positive-definite weighting matrix of dimensions $n_x \times n_x$ and R_l is a weighting scalar.

From Eqs (3.21) and (3.25), a higher K_d contributes to larger $G_{yd}(s)$ and consequently larger $H(s)$, and hence is favoured from the perspective of performance robustness. However, in the interests of closed-loop system stability robustness, K_d is not regarded as the main approach to reduce system sensitivity, but only used to fine tune the sensitivity achieved primarily by the low-pass filter. For an SISO case as the ATBMW application documented herein, K_d is simply a scalar and any value up to the bandwidth limited by the zeros of the plant stables $(\boldsymbol{A} - \boldsymbol{LC} - \boldsymbol{B}K_d\boldsymbol{C})$ with a properly designed $\boldsymbol{L}$. Instead of selecting K_d casually,

a systematic method based on linear-quadratic optimisation is formulated in the following, on an MIMO basis without losing generality.

According to Eq (3.36) with $\xi(t)$ neglected as $\xi(t) \to 0$ with time, we have:

$$\begin{cases} \dot{\boldsymbol{e}}_x(t) = (\boldsymbol{A} - \boldsymbol{LC})\boldsymbol{e}_x(t) + \boldsymbol{B}\boldsymbol{e}_{dv}(t) \\ \boldsymbol{e}_y(t) = \boldsymbol{C}\boldsymbol{e}_x(t) \end{cases}, \tag{3.41}$$

where

$$\begin{cases} \boldsymbol{e}_x(t) = \boldsymbol{x}(t) - \hat{\boldsymbol{x}}(t), \\ \boldsymbol{e}_y(t) = \boldsymbol{y}(t) - \hat{\boldsymbol{y}}(t), \\ \boldsymbol{e}_{dv}(t) = -\boldsymbol{K}_d\boldsymbol{C}\boldsymbol{e}_x(t). \end{cases}$$

Under *Assumption 2* in Section 3.1, the pair $(\boldsymbol{A} - \boldsymbol{LC},\ \boldsymbol{B}K_d\boldsymbol{C})$ is observable. Given the duality property, this is to select $\boldsymbol{K}_v = (\boldsymbol{B}\boldsymbol{K}_d)^T$ that minimises the performance index

$$J_d = \int_0^\infty \left\{ \boldsymbol{e}_x^T(t)\boldsymbol{Q}_d\boldsymbol{e}_x(t) + \boldsymbol{e}_{dv}^T(t)\boldsymbol{R}_d\boldsymbol{e}_{dv}(t) \right\} dt, \tag{3.42}$$

with symmetric positive-definite weighting matrixes $\boldsymbol{Q}_d$ and $\boldsymbol{R}_d$ of respective sizes $n_x \times n_x$ and $n_y \times n_y$.

As a result,

$$\boldsymbol{K}_d = \boldsymbol{B}^\dagger \boldsymbol{K}_v^T, \tag{3.43}$$

where $\boldsymbol{B}^\dagger$ is the Moore-Penrose pseudo inverse of matrix $\boldsymbol{B}$.

With the inherited merits from the state-space approach, the method particularly suits MIMO cases as the gain becomes a vector, which however, is not the focus within the scope of the project documented herein, and hence more details regarding MIMO

applications are not to be addressed. The K_d for an SISO case can be solved directly from the aforementioned approach without any difficulty.

If ω_d is supposed to be the dominant frequency component of the equivalent unknown input, the solved K_d should yield a large enough sensitivity $S(s)$ at ω_d so that $|y(j\omega_d)|$ subjected to $|d_e(j\omega_d)|$ according to Eq (3.22) is small enough to meet the design specifications. Under the circumstance that ω_d is uncertain, an upper bound of commonly encountered frequencies could be used for a safe design.

In the light of the simultaneous influence from the state observer gain and UIE gain on the overall closed-loop system stability, an iterative procedure is needed for the controller design to meet the requirements on both unknown-input rejection and stability robustness. The iteration could bring considerable work load when the same procedure is to be repeated for a large number of controllers. However, the overall process becomes much easier and more efficient when individual UIE-integrated LQG controllers for the actuators on ATBMWs are designed according to actuator dynamics only. The reason is manifest. In ideal conditions there are few variations between characteristics of same-model actuators, while the induced dynamics from adjacent structures could differ to a large extent when the actuators are on the wing. Thus, once one controller is satisfactorily designed according to actuator dynamics, the work for remaining actuators can be based on the first controller, with slight parameter adjustments or even no change.

(2) Low-pass filter $(\boldsymbol{A}_f, \boldsymbol{B}_f, \boldsymbol{C}_f)$ or $G_f(s)$

As discussed in Section 3.3.1, the low-pass filter is the primary component to yield the significantly reduced closed-loop system sensitivity. With a properly designed low-pass filter that meets condition (a) of the *Theorem* in Section 3.3.2, the overall closed-loop stability is ensured by an appropriate set of the state observer gain $\boldsymbol{L}$ and the UIE gain K_d, according to condition (b) of the *Theorem*. Therefore, on the design of the low-pass filter, the focus can be put mainly on reducing the system sensitivity.

Firstly, a first-order filter is preferred, as

$$G_f(s) = \frac{1}{\frac{1}{\omega_c}s + 1} = \frac{1}{\tau s + 1}, \tag{3.44}$$

where ω_c is the cutoff frequency and τ is the time constant.

This is because a longer delay occurs to the signal under higher-order filters due to phase shift, which slows down the UIE response and degrades the estimation performance, though a higher order gives better approximation to an ideal filter.

Secondly, the cutoff frequency ω_c is decided according to the frequency of interest associated with possible unknown inputs that the plant may encounter. It is straightforward to conclude from the characteristics of a low-pass filter that increasing ω_c can reduce the power attenuation of signals at lower frequencies and consequently enables higher accuracy in unknown-input estimation. There are not additional specific restrictions regarding the selection of ω_c as long as it could cover the natural frequency of the majority of unwanted unknown inputs meanwhile meeting normal requirements in practical filter design from a cost-effective point of view.

An exact knowledge regarding unknown inputs are normally unknown, it is thus a significant merit of the proposed UIE that selecting only one parameter, ω_c, can effectively treat a wide range of unknown inputs in a unified way instead of determining the natural frequency of every possible unknown input individually.

Finally, the corresponding state-space representation $(\boldsymbol{A}_f, \boldsymbol{B}_f, \boldsymbol{C}_f)$ can be obtained via a proper transform from $G_f(s)$, and it does not matter which representation is used for an SISO case. With regard to MIMO cases, using the state-space representation is much more convenient, which however, is out of the current scope of this project, and is recommended for future work.

Chapter 4

SIMULATIONS

In Section 3.3.3, guidelines for designing the proposed UIE-integrated LQG controller are recommended. Simulations in Section 4.1 of this chapter provide illustration and validation of the guidelines.

As mentioned in Section 1.2, the term 'unknown inputs' used herein is referred to as a broader expression that includes both exogenous disturbances (e.g. unmeasured loads) and internal uncertainties (e.g. un-modelled system dynamics). For better understanding of the mechanism of unknown-input estimation and compensation, in Section 4.2 we present the simulations in two parts. Firstly exogenous unknown inputs are simulated as an equivalent quantity at the control input and hence we can see how close the estimate matches the equivalent unknown input. Next, exogenous disturbances are removed from the system while modelling errors are added, so that the compensation effort can then be reflected by the difference between the control signals before and after the introduction of modelling errors.

Finally in Section 4.3, an investigation into using only actuator dynamics for the actuator controller design for the ATBMW prototype is presented.

4.1 Influence of UIE-related Parameters

To verify the rules stated in Section 3.3.3 for designing the proposed UIE-integrated LQG controller, the parameters related to the UIE are investigated individually in simulations. Though the state observer is not included in the UIE structure, it has

substantial influence on UIE performance and affects the overall system sensitivity and stability robustness, and hence its gain is regarded as UIE-related and examined as well.

Simulation scenarios in this section are based upon actuator B, and corresponding model in Category I (actuator dynamics) is used for controller design. Parameters of the full-state feedback control law are consistent throughout all these scenarios, while UIE parameters and the state observer gain vary individually in respective cases.

4.1.1 Low-pass Filter

(1) Low-pass Filter Order

A first-order low-pass filter as in Eq (3.44) with the passband gain equal to 1 is recommended in Section 3.3.3. To validate the choice, we generalise the low-pass filter in the following form:

$$G_f(s) = \frac{\sum_{i=0}^{p} a_{mi}(\tau s)^i}{(\tau s + 1)^m}, \tag{4.1}$$

where m and p denote the order of the denominator and numerator, respectively.

As mentioned, condition (b) in the *Theorem* in Section 3.3.2 is not satisfied when $p \geq 1$. Thus we only investigate cases where $m \geq 1$ and $p = 0$. In the simulations that follow, four low-pass filters ($m = 1,2,3,4$) are used, and the influence of different m is commented accordingly in every simulation scenario.

(2) Cutoff Frequency

Under the prerequisite that the natural frequency of unknown inputs is below the cutoff frequency ω_c of the low-pass filter, the sensitivity and stability robustness of the overall closed-loop system is affected when ω_c varies.

Following the guidelines in Section 3.3.3, the UIE-integrated LQG controller is designed using the weights in Table 4.1, with corresponding gains and remaining parameters listed in Table 4.2. Similar to a standard LQG design procedure, the weighting coefficients and matrixes are initially selected according to Bryson's rule (Bryson and Ho, 1969), and then some iteration is performed to yield appropriate gains for a trade-off between system sensitivity and stability robustness. Details of selecting the state observer gain $\boldsymbol{L}$ and the UIE gain K_d are demonstrated and explained later in Sections 4.1.2 and 4.1.3.

Table 4.1: Weights used in the UIE-integrated LQG controller design for actuator B according to the corresponding model in Category I

Standard LQG Controller					UIE	
Q_y	Q_w	R_η	$\boldsymbol{Q}_l$	R_l	$\boldsymbol{Q}_d$	R_d
3.5×10^{2}	1×10^{-3}	1	$\begin{bmatrix} 5\times10^{4} & 0 \\ 0 & 5\times10^{4} \end{bmatrix}$	1	$\begin{bmatrix} 2\times10^{8} & 0 \\ 0 & 2\times10^{8} \end{bmatrix}$	1

Table 4.2: Parameters of the UIE-integrated LQG controller for actuator B with the low-pass filter cutoff frequency ω_c as the variable of interest

Standard LQG Controller				UIE	
K_r	K_w	$\boldsymbol{K}_x$	$\boldsymbol{L}$	K_d	m
18.7115	−0.0316	$\begin{bmatrix} 18.7116 \\ 0.8689 \end{bmatrix}^T$	$\begin{bmatrix} 223.6386 \\ 7.1040 \end{bmatrix}$	52.1186	$1 \le m \le 4,$ $\forall m \in \mathbb{Z}$

The magnitude of system sensitivity $S(j\omega)$ at $\omega_d = 10$ (rad/s) versus the low-pass filter cutoff frequency $10^2 \le \omega_c \le 10^3$ (rad/s) is plotted in Figure 4.1. When the frequencies that characterise the unknown inputs are well below ω_c, raising ω_c yields reduced sensitivity. This is a straightforward result reflected by the characteristics of a real low-pass filter, since higher ω_c results in less power reduction to the same signals of frequency below ω_c. A 1st-order filter ($m = 1;\ p = 0$) demonstrates the smallest sensitivity among the four, because less phase shift is imposed to signals and higher accuracy in estimation is resulted.

The system stability robustness index β against $10^{-1} \leq \omega_c \leq 10^3$ (rad/s) is shown in Figure 4.2. Though higher ω_c contributes to lower sensitivity at a certain frequency below ω_c, it inevitably decreases the stability robustness of the close-loop system. In the meantime, a filter of lower order enables smaller system sensitivity by sacrificing the stability robustness.

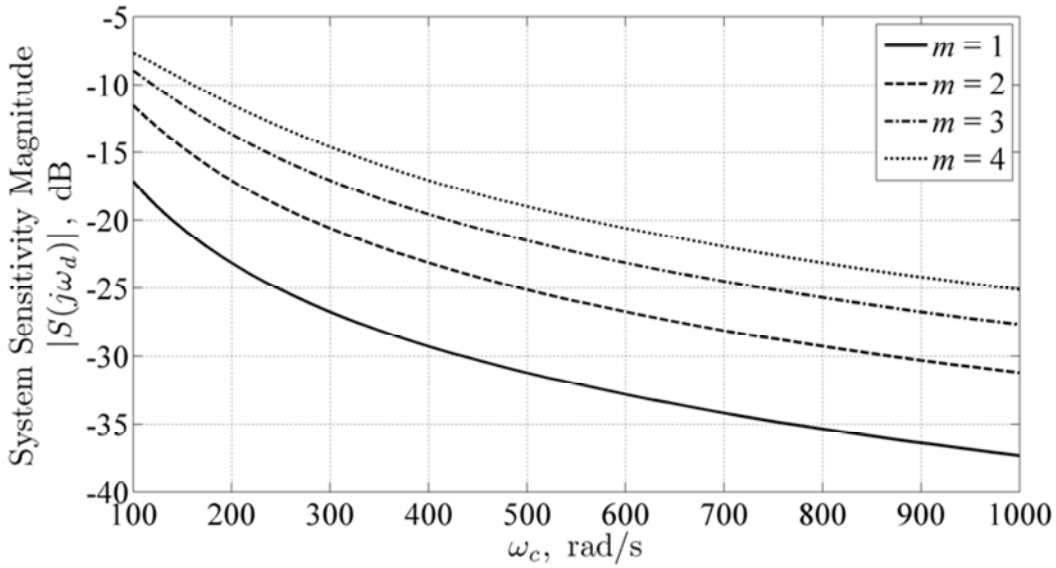

Figure 4.1: Magnitude of system sensitivity $S(j\omega)$ at $\omega_d = 5$ (rad/s) versus low-pass filter cutoff frequency ω_c

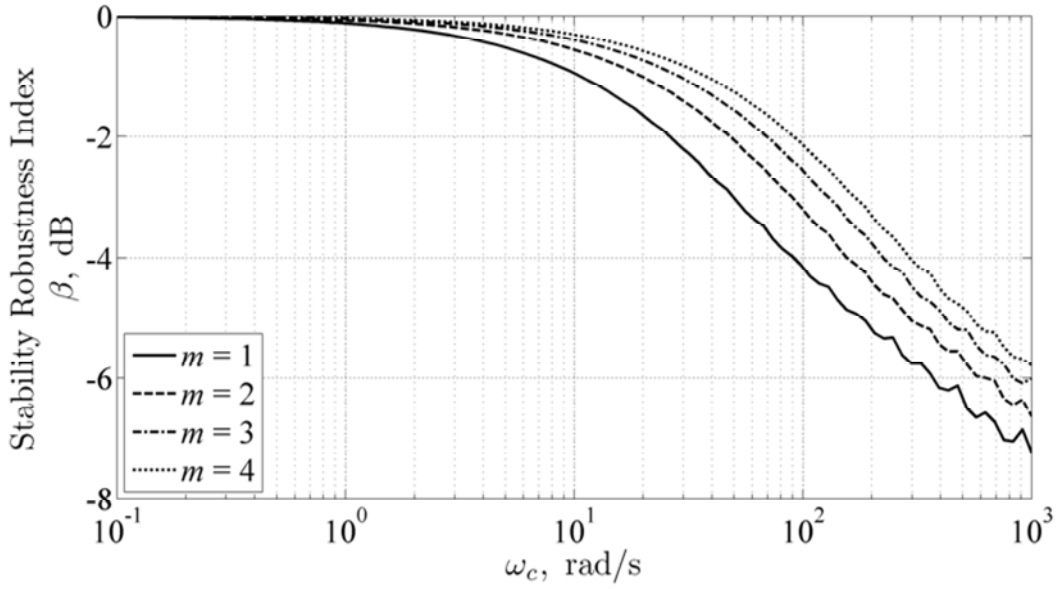

Figure 4.2: Stability robustness index β versus low-pass filter cutoff frequency ω_c

Although a low-pass filter of lower order with higher cutoff frequency is undesired in the interests of the closed-loop system stability robustness, it is nevertheless recommended in consideration of its critical role in reducing the system sensitivity for improved performance robustness to unknown inputs. The fact that the low-pass filter is not the only factor having an influence on the system stability robustness makes the preference feasible and applicable. Once the low-pass filter has been designed, the stability robustness of the closed-loop system can then be ensured by selecting an appropriate state observer gain, as proved in Section 3.3.2.

Given that the dynamic change of wind and wing-shape-induced air pressure lie in a low-frequency range, 100 rad/s can be a reasonable choice as the cutoff frequency of the low-pass filter for the UIE-integrated LQG controller used on an ATBMW. Accordingly, this frequency value is used in remaining simulations and throughout wind tunnel experiments in Chapter 5.

4.1.2 State Observer Gain

Using parameters in Table 4.3 (inherited from Table 4.2) and with the state observer gain $\boldsymbol{L}$ being the variable for investigation, the influence of the state observer gain to system sensitivity and stability robustness is illustrated in Figures 4.3 and 4.4, respectively.

Table 4.3: Parameters of the UIE-integrated LQG controller for actuator B with the state observer gain $\boldsymbol{L}$ as the variable of interest

Standard LQG Controller			UIE		
K_r	K_w	$\boldsymbol{K}_x$	K_d	m	ω_c (rad/s)
18.7115	−0.0316	$\begin{bmatrix} 18.7116 \\ 0.8689 \end{bmatrix}^T$	52.1186	$1 \leq m \leq 4,$ $\forall m \in \mathbb{Z}$	100

It can be seen in Figure 4.3 that smaller system sensitivity is achieved at a lower state observer gain. As the gain $\boldsymbol{L}$ increases, the disturbance compensation effect from the UIE continuously weakens until virtually having little influence on the overall system sensitivity when the standard LQG component becomes to dominate ($\|\boldsymbol{L}\|_2 > 10^6$ in Figure 4.3, where $\|\boldsymbol{L}\|_2$ denotes the Euclidean norm of the vector $\boldsymbol{L}$). In agreement with Figure 4.1, a 1st-oreder low-pass filter contributes to better

disturbance compensation effect, as indicated by the much smaller sensitivity compared with filters of a higher order.

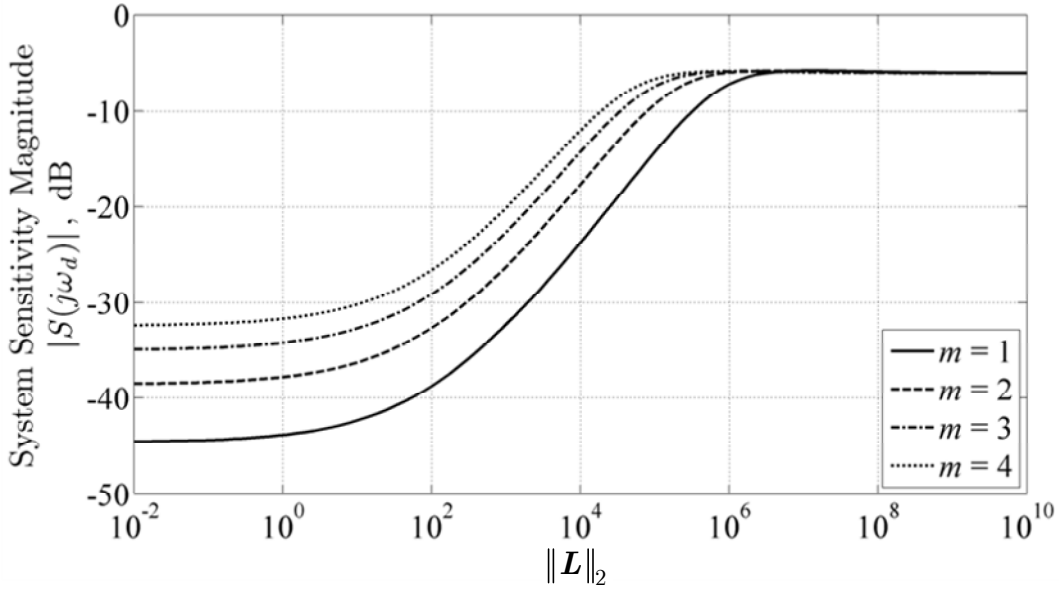

Figure 4.3: Magnitude of system sensitivity $S(j\omega)$ at $\omega_d = 5$ (rad/s) versus $\|\boldsymbol{L}\|_2$ of the state observer gain

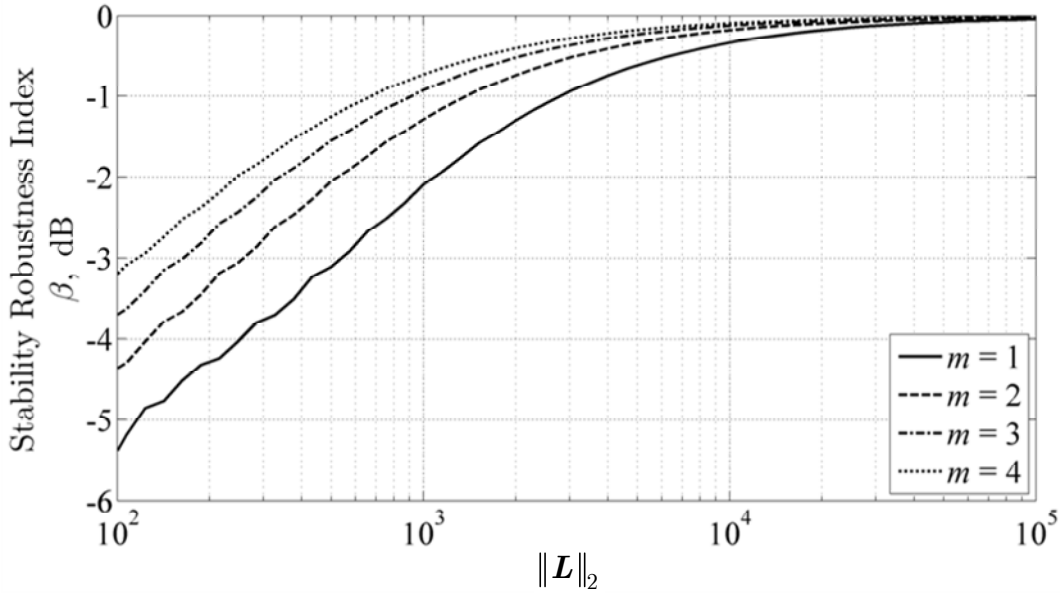

Figure 4.4: Stability robustness index β versus $\|\boldsymbol{L}\|_2$ of the state observer gain

On the contrary, Figure 4.4 shows improved stability robustness as a result of increasing $\boldsymbol{L}$. Similar to Figure 4.2, the stability robustness is sacrificed for smaller sensitivity when a low-pass filter of lower order is used. However, the difference in stability robustness becomes less sensitive to the low-pass filter order at higher $\boldsymbol{L}$, and hence it is a reasonable strategy to design $\boldsymbol{L}$ from the smallest acceptable value according to application requirements.

In the following examples of choosing an appropriate state observer gain $\boldsymbol{L}$, the model in Category II associated with actuator B is introduced to represent actual plant dynamics $P(s)$, with corresponding model in Category I being the nominal process $P_n(s)$. The perturbation $M_p(s)$ is then calculated according to $P(s)$ and $P_n(s)$. For better compensation of unknown inputs, a 1st-order low-pass filter is used.

As a conservative design in consideration of a reliable level of stability robustness, a moderate value of the state observer gain, $\boldsymbol{L}_1 = [223.6386 \quad 7.1040]^T$, is chosen (Note that this gain matrix is also used in Tables 4.2, 4.4, and 4.5). Other parameters of the UIE-integrated LQG controller remain the same as in Table 4.3. The magnitude of $\left\{1 + [H(j\omega)P_n(j\omega)]^{-1}\right\}$ and $M_p(s)$ in this case are plotted in Figure 4.5, which demonstrates that the closed-loop system remain stable across $\omega \in [0, +\infty)$ in the presence of un-modelled dynamics $M_p(s)$ since the robust stability criterion in Eq (3.35) is satisfied. The stability robustness index β is -4.1505 (dB), but the notch of $\left|1 + [H(j\omega)P_n(j\omega)]^{-1}\right|$ is actually 3.017 (dB) above $\left|M_p(s)\right|$ at the same frequency. It means a negative β does not necessarily indicate an unstable system and a value close to 0 is sufficient to provide a reliable level of stability robustness to parameter variations.

For a smaller gain of the state observer, $\boldsymbol{L}_2 = [22.3811 \quad 0.4567]^T$, with other parameters unchanged, corresponding plots in Figure 4.6 show that the robust stability inequality is not satisfied. The notch of $\left|1 + [H(j\omega)P_n(j\omega)]^{-1}\right|$ is 21.4169

(dB) below $\left|M_p(s)\right|$ at $\omega = 40.3702$ (rad/s), and the stability robustness index in this situation is $\beta = -23.9759$ (dB), which is much smaller and indicates instability.

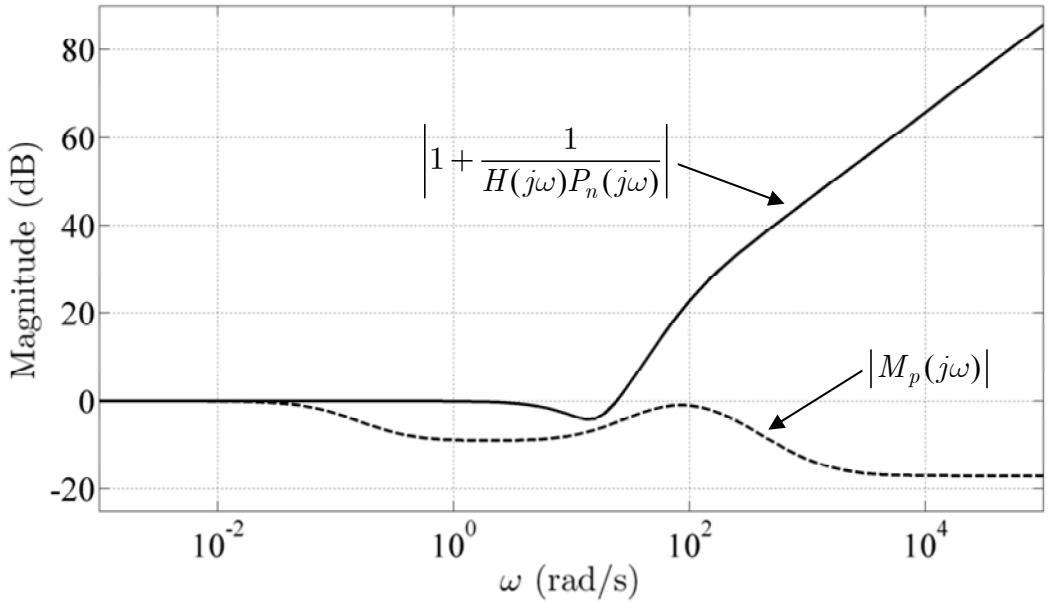

Figure 4.5: Closed-loop stability with $\boldsymbol{L}_1 = [223.6386 \quad 7.1040]^T$ in the presence of un-modelled dynamics $M_p(s)$

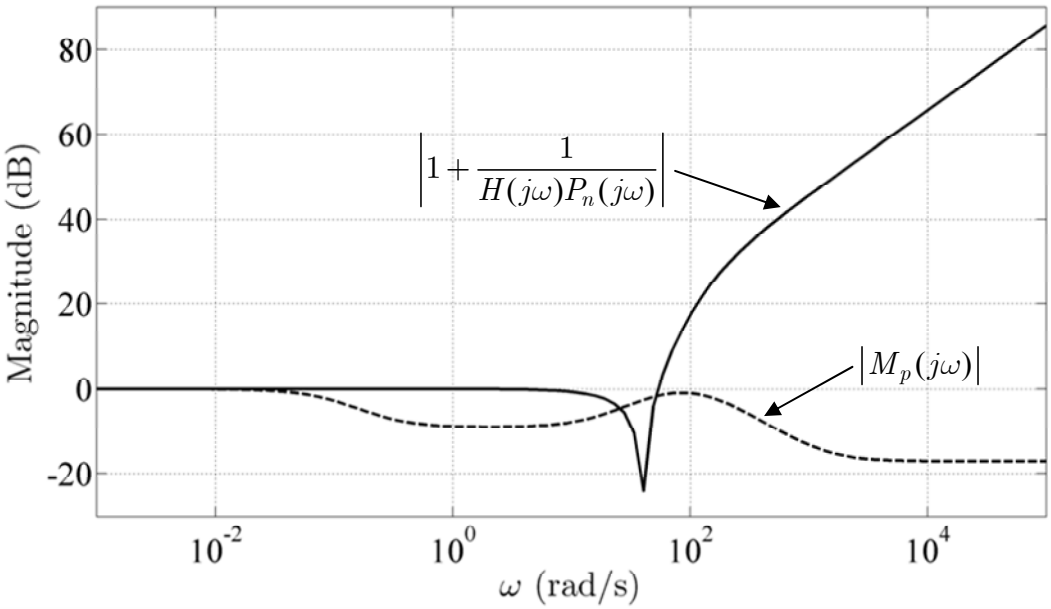

Figure 4.6: Closed-loop stability with $\boldsymbol{L}_2 = [22.3811 \quad 0.4567]^T$ in the presence of un-modelled dynamics $M_p(s)$

4.1.3 UIE Gain K_d

The effects of using different estimation gains and low-pass filters of different denominator order are investigated by means of the relative tracking error, with simulations based on actuator B. Firstly, a standard LQG controller is designed using the model of actuator B in Category I, with corresponding parameters summarised in Table 4.4. The standard LQG controller is tested as a reference without exogenous unknown inputs and assuming no modelling error or un-modelled dynamics (using the same model from Category I for both the controller and the plant). Next, a UIE is designed (see parameters in Table 4.4) and integrated into the existing standard LQG controller, with external disturbances and modelling errors added. The UIE-integrated LQG controller is tested against the varying gain K_d.

Exogenous unknown inputs are introduced as an equivalent disturbing voltage applied at the control input channel, simulated by compound sinusoids of time-varying frequency and amplitude mixed with random jumps (discontinuities) in voltage (Figure 4.7):

$$d_e(t) = c_1 \sin(\omega_1 t) + c_2 \sin(\omega_2 t) + w_d(t), \tag{4.2}$$

where $|w_d(t)| \leq 1$ is the function of bounded random numbers that change at every 0.1 second, and other sinusoidal parameters are:

$$\begin{cases} c_1 = \sqrt{t};\ \omega_1 = 0.1t + 1; \\ c_2 = \cos(\pi t/5);\ \omega_2 = 0.1\cos(\pi t/5). \end{cases}$$

Uncertainties other than exogenous unknown inputs are represented as modelling errors or un-modelled dynamics by using a different model, that is, the model of actuator B in Category II, for plant dynamics.

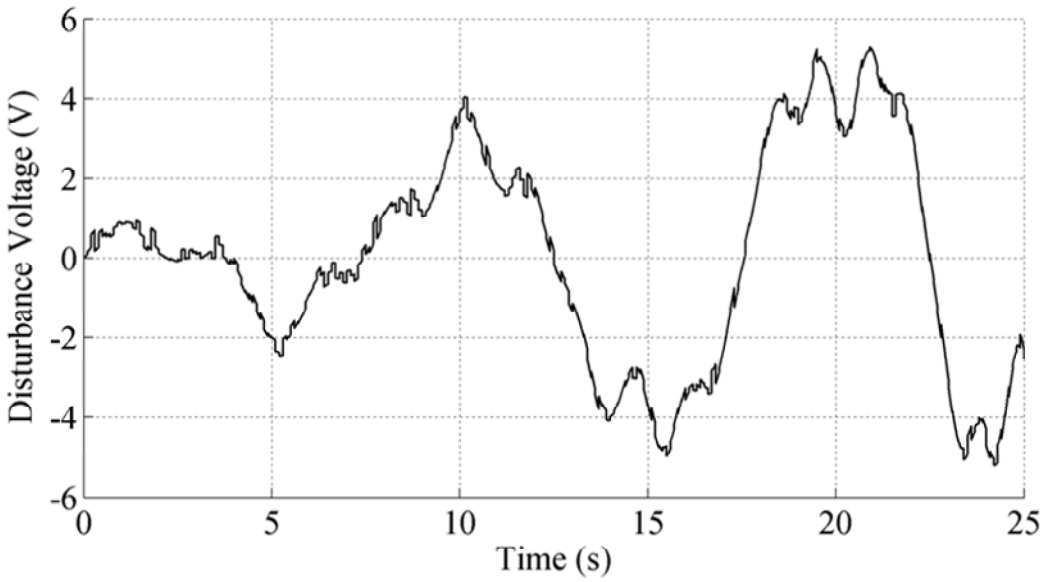

Figure 4.7: Equivalent exogenous disturbance in voltage at the control input channel simulated according to Eq (4.2)

The sample rate of simulation is set to 0.001 second. Results are analysed in terms of the deviation described by

$$\begin{cases} \alpha_1 = \left(\frac{1}{n} \sum_{i=1}^{n} \left(y_{LQG}^{(i)} - r^{(i)} \right)^2 \right)^{\frac{1}{2}} \\ \alpha_2 = \left(\frac{1}{n} \sum_{i=1}^{n} \left(y_{UIELQG}^{(i)} - y_{LQG}^{(i)} \right)^2 \right)^{\frac{1}{2}} \end{cases}, \tag{4.3}$$

where

$r^{(i)}$: The i^{th} point of the reference trajectory;

$y_{LQG}^{(i)}$: The i^{th} point of the tracking trajectory when using the standard LQG controller under no disturbances and modelling errors;

$y_{UIELQG}^{(i)}$: The i^{th} point of the tracking trajectory using the UIE-integrated LQG controller in the presence of disturbances and modelling errors;

α_1: Deviation of y_{LQG} from r;

α_2: Deviation of y_{UIELQG} from y_{LQG};

n: Number of samples.

Comparisons are made according to

$$\Delta = \frac{\alpha_2}{\alpha_1} \times 100\% . \tag{4.4}$$

The relative tracking error, as expressed in Eq (4.4), provides a measure of the disturbing effect of the unknown inputs, or in other words, a measure of how much the system is disturbed by unknown inputs, relative to the reference performance under no disturbing factors.

For a given reference tracking trajectory in Figure 4.8 and controller parameters in Table 4.4, simulation results are obtained, treated with Eqs (4.3) and (4.4), and plotted in Figure 4.9.

Table 4.4: Parameters of the UIE-integrated LQG controller for Actuator B with the UIE gain K_d as the variable of interest

Standard LQG Controller				UIE	
K_r	K_w	$\boldsymbol{K}_x$	$\boldsymbol{L}$	m	ω_c (rad/s)
18.7115	−0.0316	$\begin{bmatrix}18.7116\\0.8689\end{bmatrix}^T$	$\begin{bmatrix}223.6386\\7.1040\end{bmatrix}$	$1 \le m \le 4,$ $\forall m \in \mathbb{Z}$	100

From Figure 4.9, the following remarks can be drawn:

- The rejection of unknown inputs degrades when the order of the low-pass filter increases, although the phenomena are not significant for K_d of higher values ($K_d \ge 10^3$ in Figure 4.9).
- The curves are almost horizontal for $K_d \le 10^{-1}$ and $K_d \ge 10^3$, distinguishing a region in the middle within which the performance of unknown-input compensation is sensitive to K_d. It is therefore reasonable to select a K_d within this region in accordance with application requirements (Note that the same value of K_d, which falls within the region mentioned above, is selected for Tables 4.2, 4.3, and 4.5).
- The horizontal parts of the curves point to the same value around 280%, which is the relative tracking error of the standard LQG controller (without

UIE) in the presence of unknown inputs. As can be seen, a standard LQG controller alone cannot cope well with a broader class of un-modelled unknown inputs, whereas the problem is solved when the UIE is integrated into the controller, with tracking errors significantly reduced.

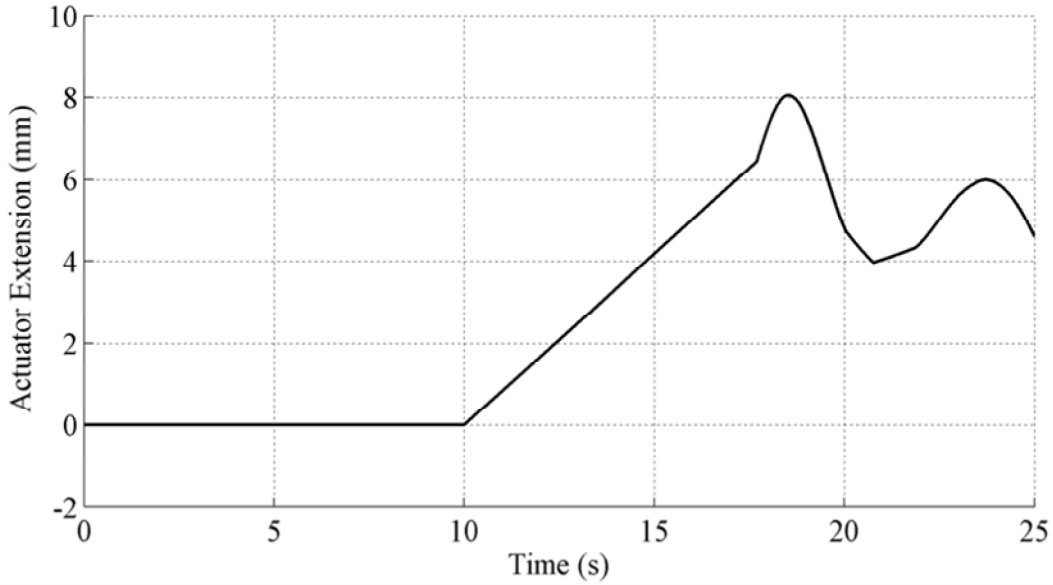

Figure 4.8: Reference tracking trajectory for actuator B

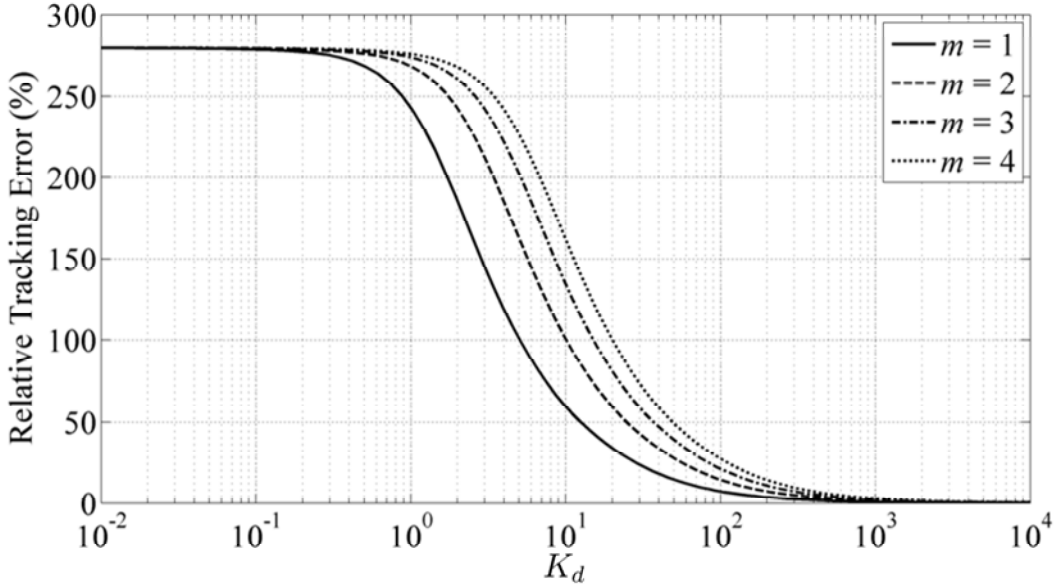

Figure 4.9: Relative tracking error Δ against K_d

4.2 Unknown-Inputs Estimation and Compensation

The previous section demonstrates the relation between relative tracking errors and UIE parameters (UIE gain and the order of the low-pass filter). Accordingly in this section a proper set of LQG and UIE parameters are determined for simulations to illustrate the mechanism of estimating and compensating (rejecting) unknown inputs.

As mentioned in Section 1.2, the term 'unknown inputs' used herein is referred to as a broader expression that includes both exogenous disturbances and internal uncertainties. In Sections 4.2.1 we look into the estimation and compensation of exogenous unknown inputs alone, while in Section 4.2.2 only internal uncertainties are assumed to exist.

4.2.1 Exogenous Disturbances Estimation and Compensation

With respect to the system as in Eqs (3.1) and (3.2), when exogenous disturbances enter the system at different channels $\boldsymbol{B}_d$, the estimate $\hat{d}_e(t)$ produced by our proposed UIE is an equivalent counteractive input required at the control input channel $\boldsymbol{B}$, which however does not necessarily reflect the actual magnitude of disturbances. For the purpose of demonstrating the unknown-input estimation mechanism, simulated exogenous disturbances are introduced as an equivalent quantity at the same input channel as the control effort.

Again, the model of actuator B in Category I is used in the following simulations of this subsection for both controller design and plant dynamics, that is, no internal uncertainties in the form of modelling errors are assumed. Since exogenous unknown loads exerted on an actuator are forces and affect the actuator as a disturbing voltage does, the corresponding resultant thrust or pull can be represented by an equivalent disturbing voltage.

Assume a linear relation

$$d_F(t) = K_M d_V(t), \tag{4.5}$$

where $d_F(t)$ and $d_V(t)$ are equivalent exogenous disturbances in force (N) and voltage (V), respectively, and K_M=2.92 (N/V) is the motor force constant.

Then the disturbance signal in Eq (4.2) has corresponding force representation as in Figure 4.10, which is for illustration only, to visualise the magnitude of the disturbance force. The quantity to be matched by the estimate in the simulation that follows is the disturbing voltage expressed in Eq (4.2) and shown in Figure 4.7.

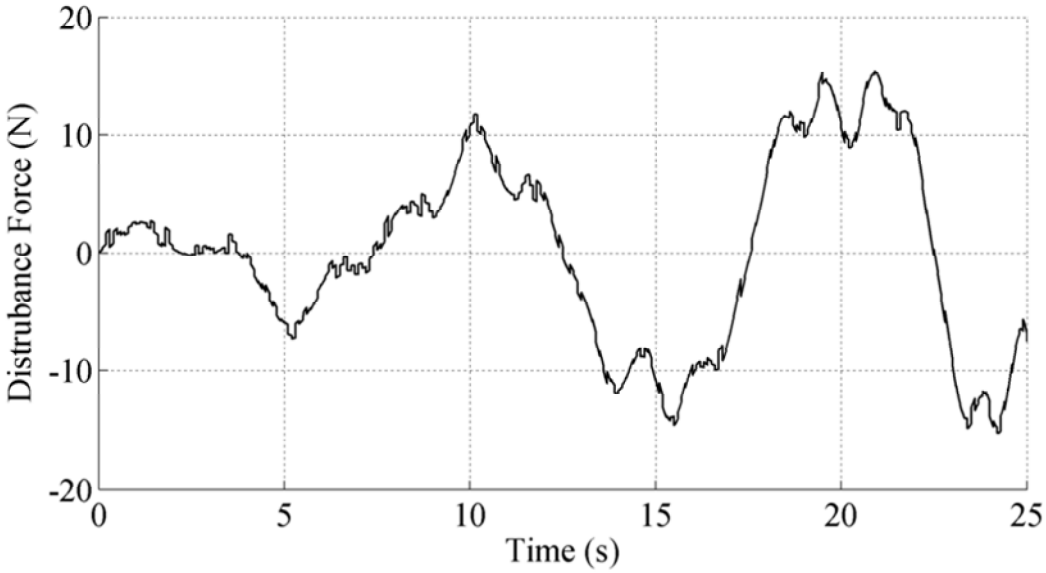

Figure 4.10: Simulated equivalent exogenous disturbance force

Parameters of the controller are listed in Table 4.5.

Table 4.5: Parameters of the UIE-integrated LQG controller for Actuator B

LQG				UIE	
K_r	K_w	$\boldsymbol{K}_x$	$\boldsymbol{L}$	K_d	$G_f(s)$
18.7115	-0.0316	$\begin{bmatrix}18.7116\\0.8689\end{bmatrix}^T$	$\begin{bmatrix}223.6386\\7.1040\end{bmatrix}$	52.1186	$\dfrac{1}{0.01s+1}$

For the standard LQG controller (without UIE), the real-time tracking is considerably disturbed by exogenous disturbances as shown in Figure 4.11, and the tracking trajectory after the equivalent disturbance is applied deviates from that of the disturbance-free case in a pattern of the disturbance signal (see Figure 4.14).

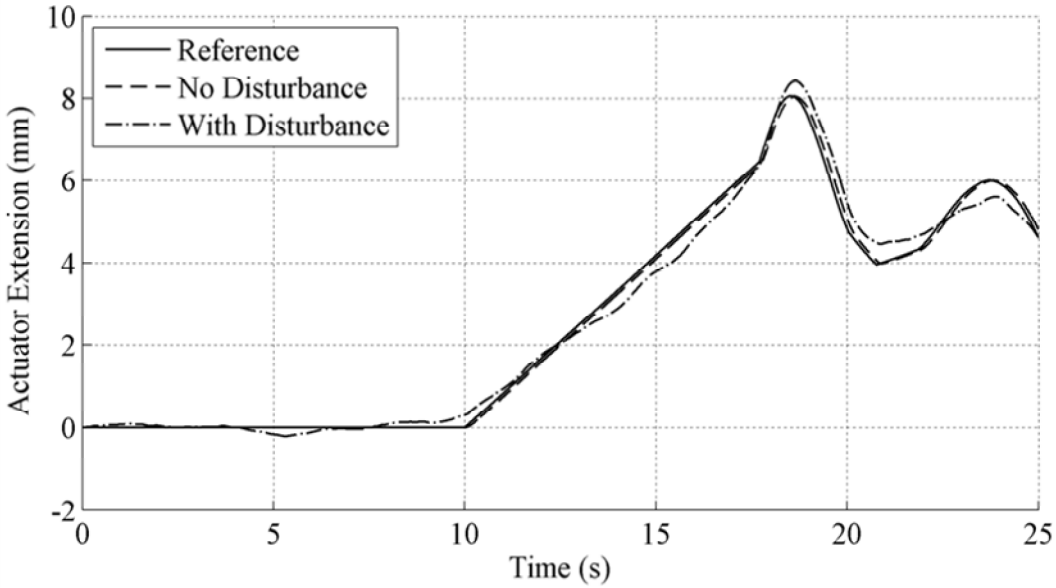

Figure 4.11: Tracking trajectories of the standard LQG controller before and after the exogenous disturbance is introduced

After the UIE is integrated into the controller, the simulated equivalent exogenous disturbance is successfully estimated with sufficient accuracy, as in Figure 4.12. The UIE component performs well despite the time-varying parameters and unpredictable discontinuities of the disturbance, and the estimate closely follows the disturbance signal with only minor deviations at random jumps. As a result, the tracking performance is significantly improved, with the difference between tracking trajectories barely identified in Figure 4.13. Now denote the difference between the tracking trajectory under unknown-input-free situation and the one subjected to the influence from unknown inputs by 'relative tracking deviation'. Plotting the relative tracking deviation of both the standard LQG controller and the UIE-integrated LQG controller produces Figure 4.14. It is apparent in Figure 4.14 that the UIE-integrated LQG controller outperforms the standard LQG controller.

Since the disturbance is substantially compensated by the UIE, leaving only traces of residuals, the LQG component in the UIE-integrated LQG controller is basically not affected by the disturbance. This can be indicated by the control effort $u_c(t)$ before and after the exogenous disturbance is introduced. It is clear in Figure 4.15 that two curves of $u_c(t)$ generally coincide with each other. The Spikes of $u_c(t)$ in the

presence of the exogenous disturbance are caused by the discontinuities $w_d(t)$ in Eq (4.2) because a transient phase is required for $\hat{d}_e(t) \rightarrow d_e(t)$. The fast response of the UIE is manifest as shown by the sharp spikes.

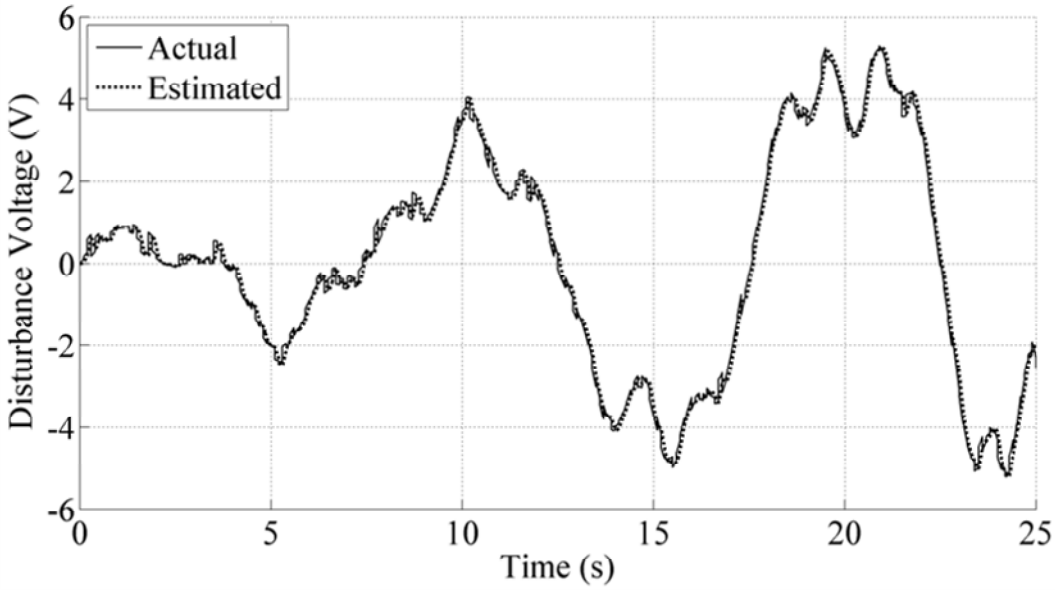

Figure 4.12: Estimation of the equivalent exogenous disturbance

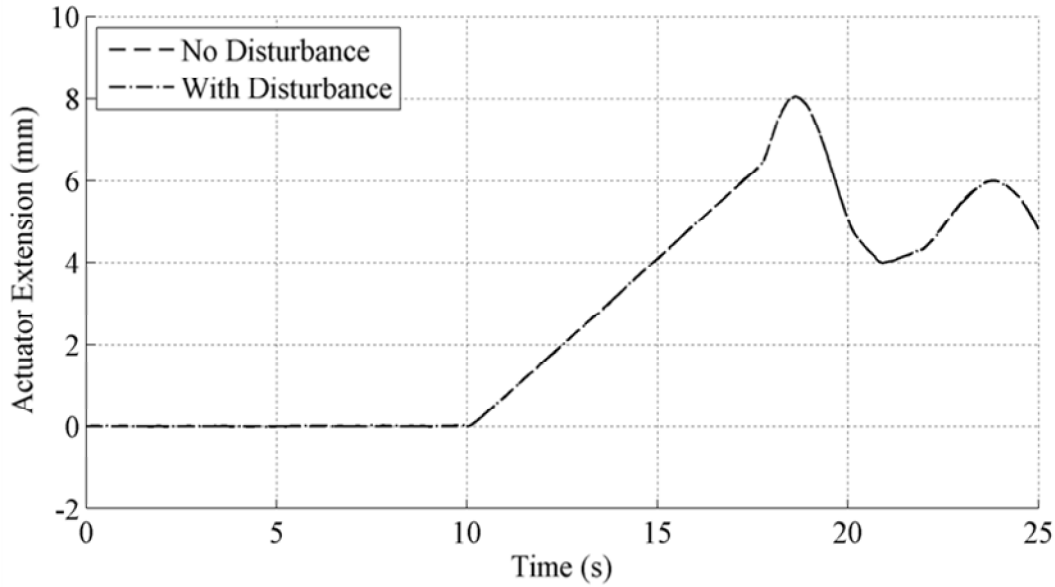

Figure 4.13: Tracking trajectories of the UIE-integrated LQG controller before and after the exogenous disturbance is introduced

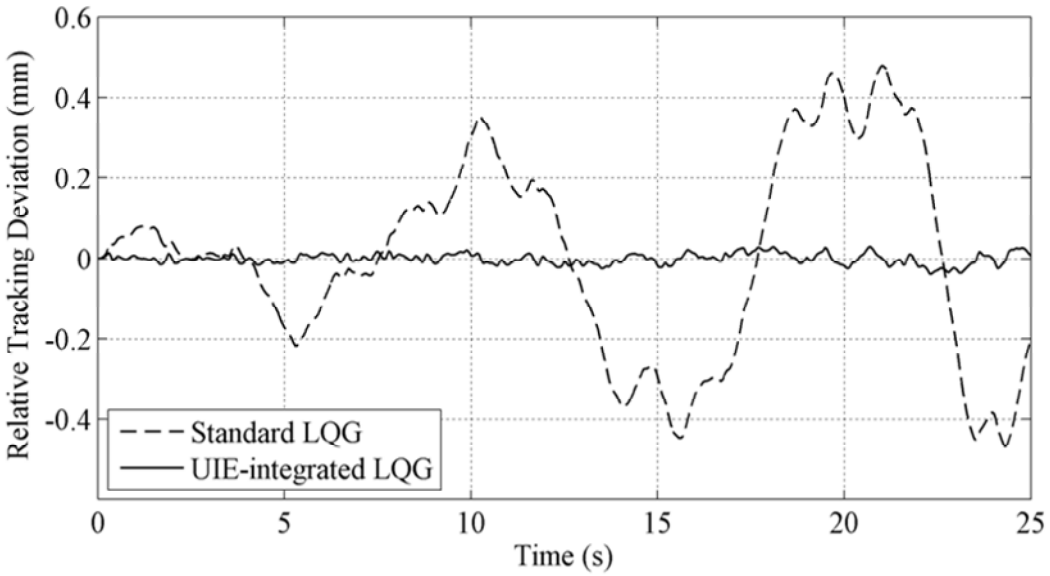

Figure 4.14: The relative tracking deviation of the standard LQG controller and the UIE-integrated LQG controller in the presence of the exogenous disturbance

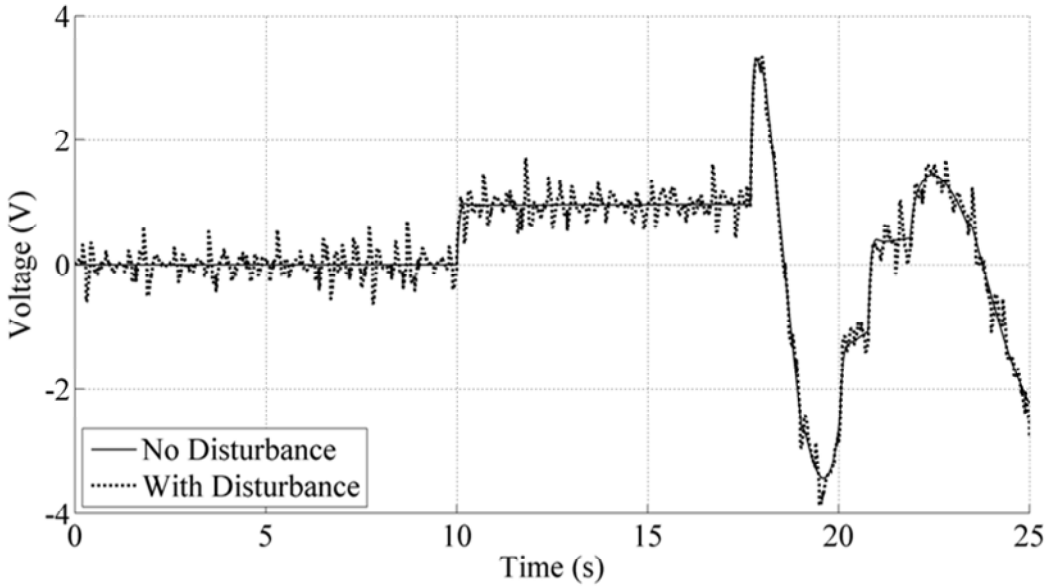

Figure 4.15: The control effort $u_c(t)$ produced by the LQG component of the UIE-integrated LQG controller before and after the exogenous disturbance is introduced

4.2.2 Compensation of Modelling Errors

In regard to internal uncertainties, mostly modelling errors due to neglected dynamics or parameters variations with time, the use of an equivalent quantity at the control input offers a reliable and easy solution to compensation. The corresponding

compensation effort can be identified by the change of the control signal before and after modelling errors are added, in the absence of exogenous disturbances. In the following simulations, the same reference trajectory as in Figure 4.8 is used, the simulated equivalent exogenous disturbance is removed, and the model of actuator B in Category II is used for plant dynamics while the controller design is based on the corresponding model in Category I.

The tracking results of the standard LQG controller in situations with and without modelling errors are shown in Figure 4.16, with the relative tracking deviation plotted in Figure 4.18. It can be seen in both figures that internal uncertainties in the form of modelling errors cause some apparent trajectory deviations from 18.5s. With regard to the UIE-integrated LQG controller, the counteractive compensation effort is generated accordingly, leaving the LQG component unaffected. By feeding back proper compensation efforts predicted by the UIE, the relative tracking deviation is effectively reduced as in Figures 4.17 and 4.18, with barely identifiable trajectory difference.

In Figure 4.19 are the control efforts $u_c(t)$ produced by the LQG component of the UIE-integrated LQG controller before and after modelling errors are introduced into the closed-loop system. Accordingly, the voltage curves of the other control effort $\hat{d}_e(t)$ in Eq (3.3), which comes from the UIE component, are plotted in Figure 4.20. Under the circumstance with no exogenous and no modelling errors, $\hat{d}_e(t)$ simply remains zero as in Figure 4.20, which means the corresponding $u_c(t)$ in Figure 4.19 is actually identical to the control effort $u(t)$ of a standard LQG controller in the same situation. After modelling errors are present, there is little change to $u_c(t)$ while $\hat{d}_e(t)$ shows considerable variation, revealing that the modelling errors are effectively handled by $\hat{d}_e(t)$. The large magnitude of $\hat{d}_e(t)$ after 18.5s means more efforts are required to compensate the modelling errors, and thus explains the relative tracking deviation of the standard LQG controller without UIE (see Figures 4.16 and 4.18).

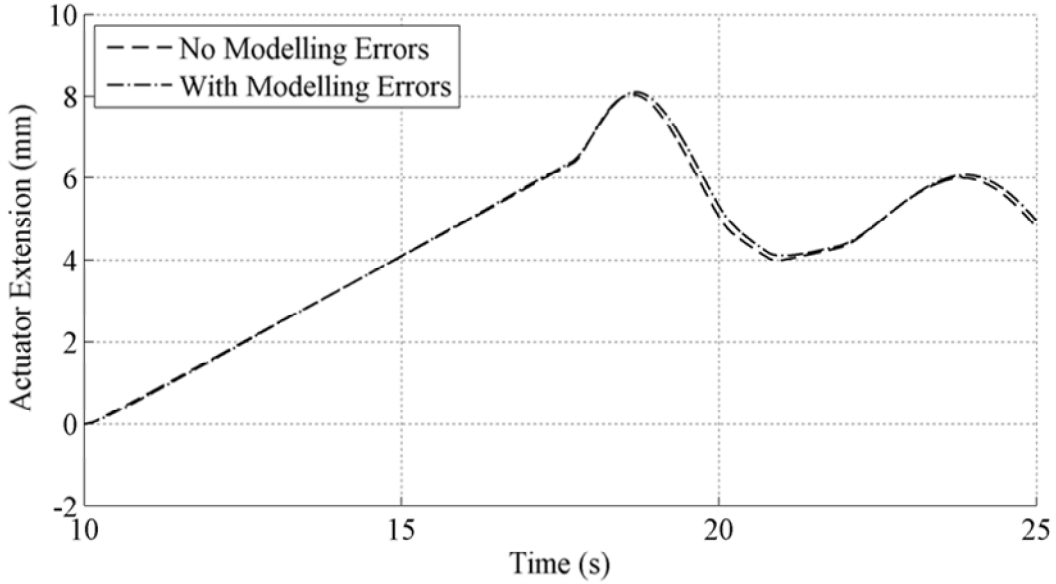

Figure 4.16: Tracking trajectories of the standard LQG controller with and without modelling errors

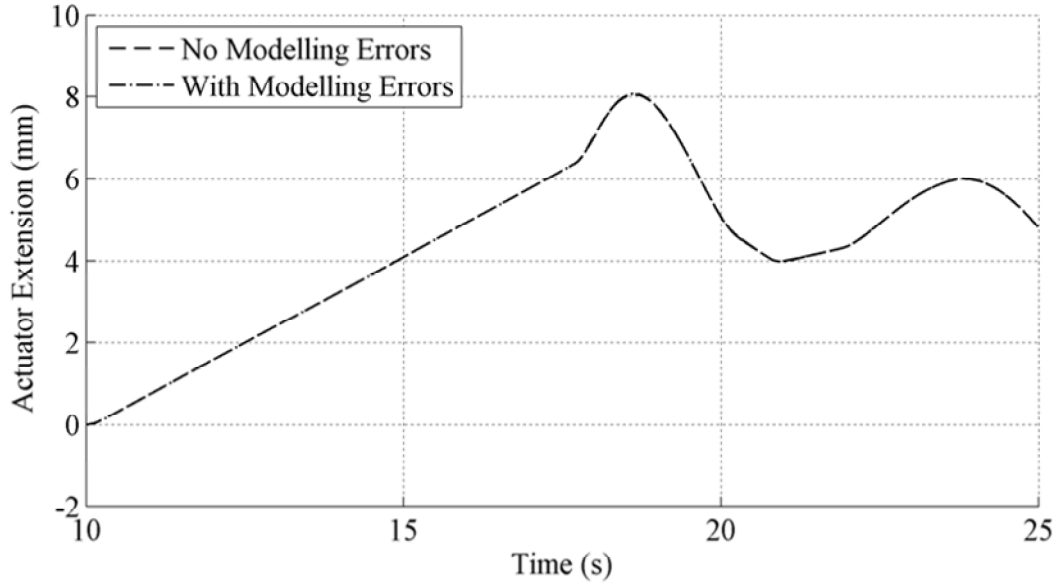

Figure 4.17: Tracking trajectories of the UIE-integrated LQG controller with and without modelling errors

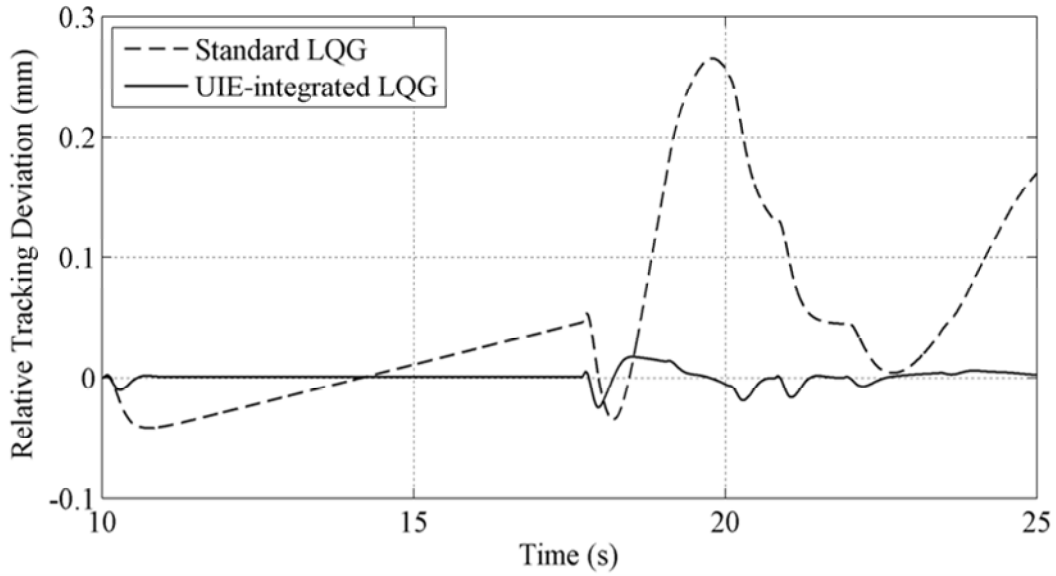

Figure 4.18: The relative tracking deviation of the standard LQG controller and the UIE-integrated LQG controller with modelling errors

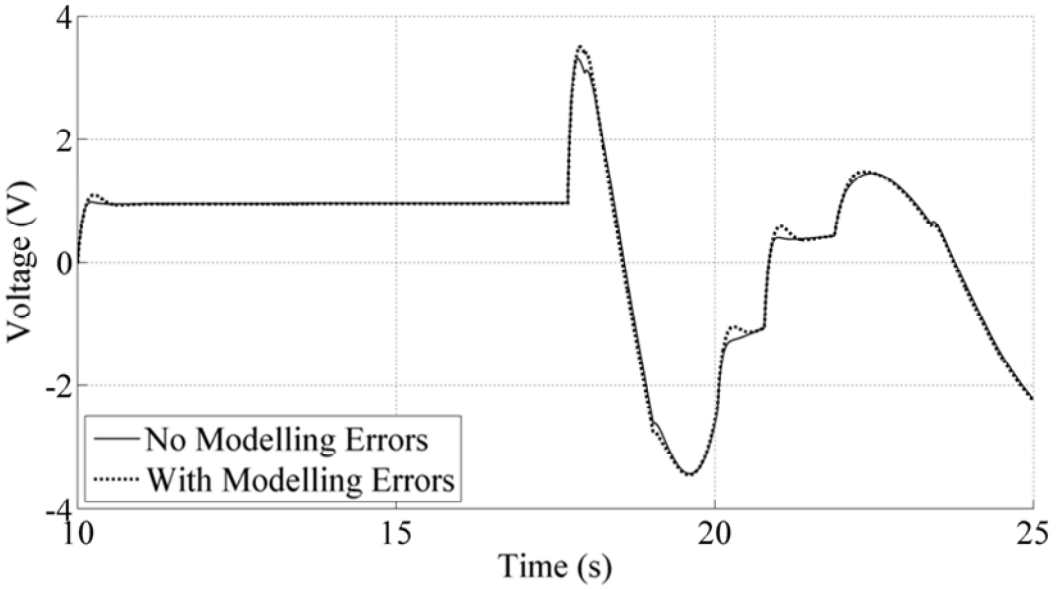

Figure 4.19: The control effort $u_c(t)$ from the LQG component of the UIE-integrated LQG controller with and without modelling errors

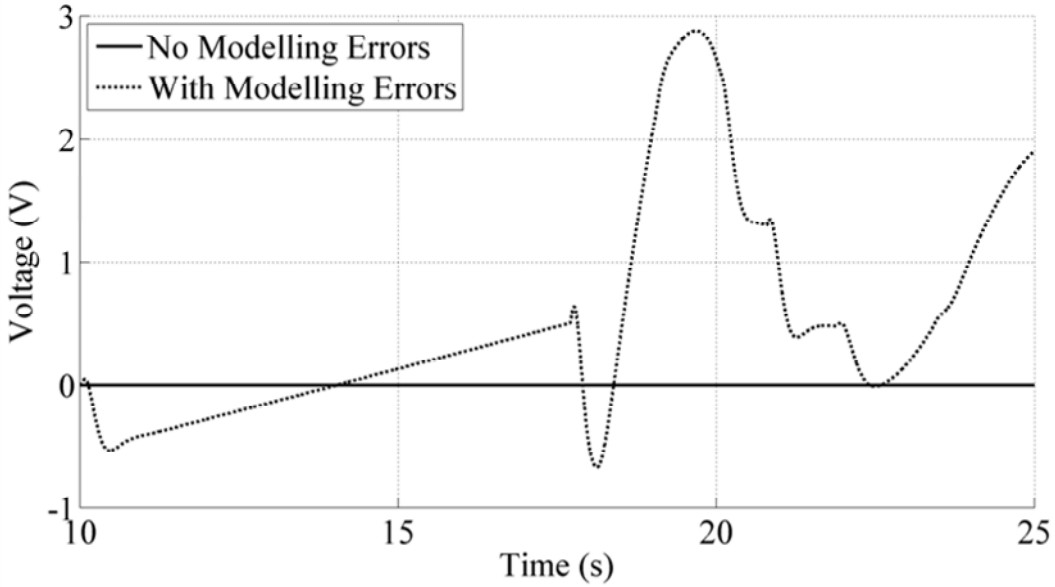

Figure 4.20: The control effort $\hat{d}_e(t)$ from the UIE component of the UIE-integrated LQG controller with and without modelling errors

4.3 Compensation of Un-modelled Wing Structural Dynamics

The previous section illustrates the mechanism of unknown-input estimation and compensation using the proposed UIE-integrated LQG control scheme and in the meantime validates its efficacy and advantages over a standard LQG counterpart. In this section, the proposed controller is employed on all five actuators of the ATBMW prototype for further validation with the focus on compensating un-modelled wing structural dynamics.

Wing structural dynamics consist of induced forces and torques from mechanically coupled linkages, frictions in joints and between sliding wing skin layers, and resistance due to elastic deformation of the wing skin, etc. It is of vital importance to take these factors into account to ensure consistent controller performance as designed, whereas the underlying problem remains at the difficulty to exactly model or measure these quantities. Since the uncertainties influence the overall system in different ways, using an equivalent quantity to counteract the resultant effect is simple and effective to handle most of the uncertainties in a unified way.

Details of the UIE-integrated LQG controller design are as follows:

- Actuator dynamics (Models in Category I) are used directly as the nominal plant dynamics for controller design.
- To assign a proper UIE gain K_d for each controller, the disturbed response of corresponding actuator around setpoint zero is evaluated according to Eq (3.22). The unknown inputs possibly encountered by individual controllers on an ATBMW in motion are supposed to have the dominant frequency at $\omega_d = 0.4\pi$ (rad/s). Since the linear actuator used on the ATBMW prototype is driven by a DC motor which works within the range of ± 12 V (see Table A.1 in Appendix A), a maximum magnitude of 10V is assumed for the equivalent unknown input $d_e(j\omega_d)$. The actuator response $|y(j\omega_d)|$ subjected to $|d_e(j\omega_d)|$ is expected to be less than 0.1mm, given the 0.1mm positioning precision of the linear actuator (see Table A.1 in Appendix A).
- To select the state observer gain $\boldsymbol{L}$, the stability robustness index $\beta > -5$ is desired as explained in Section 4.1.2. After some iteration the weighting coefficients and matrixes in Table 4.6 yield satisfactory parameters in Table 4.7 for each actuator controller, with corresponding disturbed responses $|y(j\omega_d)|$ and stability robustness index β given in Tables 4.8 and 4.9, respectively.

For comparison, the proportional-integral-derivative (PID) controller is designed and tested in addition to the proposed UIE-integrated LQG controller given the fact that a majority of commercial aircraft wing control surfaces rely on PID controllers. The PID controller used here has a parallel structure with a 1st-order low-pass filter for the derivative term (Figure 4.21). The setpoint weightings, b_1 and b_2 for respective proportional and derivative terms, are set to 1 for better real-time trajectory tracking performance (Åström and Hägglund, 2006). Other parameters (as in Table 4.10) are optimally designed and tuned using MATLAB R2010b® PID tuner. The design is based on actuator dynamics (Models in Category I) and has a target phase margin over 60° to allow for modelling errors or variations in system dynamics.

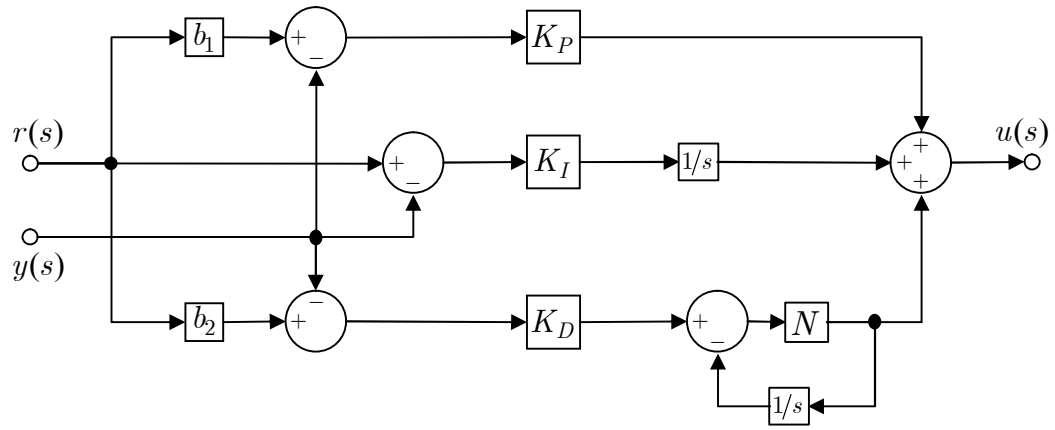

Figure 4.21: Schematic of the PID controller used for comparison

Table 4.6: Weights used for the UIE-integrated LQG controller design based on actuator dynamics

	Q_y	Q_w	$\boldsymbol{Q}_l$	$\boldsymbol{Q}_d$
Actuator B	3.5×10^{2}	1×10^{-3}	$\begin{bmatrix}5\times10^{4} & 0\\ 0 & 5\times10^{4}\end{bmatrix}$	$\begin{bmatrix}2\times10^{8} & 0\\ 0 & 2\times10^{8}\end{bmatrix}$
Actuator L	2×10^{2}	1×10^{-3}	$\begin{bmatrix}5\times10^{4} & 0\\ 0 & 5\times10^{4}\end{bmatrix}$	$\begin{bmatrix}2\times10^{9} & 0\\ 0 & 2\times10^{9}\end{bmatrix}$
Actuator M	2.1×10^{2}	1×10^{-3}	$\begin{bmatrix}5\times10^{4} & 0\\ 0 & 5\times10^{4}\end{bmatrix}$	$\begin{bmatrix}1\times10^{9} & 0\\ 0 & 1\times10^{9}\end{bmatrix}$
Actuator N	2×10^{2}	1×10^{-3}	$\begin{bmatrix}5\times10^{4} & 0\\ 0 & 5\times10^{4}\end{bmatrix}$	$\begin{bmatrix}4\times10^{9} & 0\\ 0 & 4\times10^{9}\end{bmatrix}$
Actuator O	3.5×10^{2}	1×10^{-3}	$\begin{bmatrix}5\times10^{4} & 0\\ 0 & 5\times10^{4}\end{bmatrix}$	$\begin{bmatrix}3\times10^{8} & 0\\ 0 & 3\times10^{8}\end{bmatrix}$

(R_η, R_l, and R_d used in the design of each actuator controller are all set to 1.)

Table 4.7: Parameters of the UIE-integrated LQG controller designed according to actuator dynamics

	Actuator B	Actuator L	Actuator M	Actuator N	Actuator O
K_r	18.7115	14.1452	14.4950	14.1452	18.7112
K_w	−0.0316	−0.0316	−0.0316	−0.0316	−0.0316
$\boldsymbol{K}_x$	$\begin{bmatrix}18.7116\\ 0.8689\end{bmatrix}^T$	$\begin{bmatrix}14.1462\\ 0.4549\end{bmatrix}^T$	$\begin{bmatrix}14.4973\\ 0.5016\end{bmatrix}^T$	$\begin{bmatrix}14.1610\\ 0.4084\end{bmatrix}^T$	$\begin{bmatrix}18.7327\\ 0.7414\end{bmatrix}^T$
K_d	52.1186	37.8907	37.4643	64.0588	72.7574
$\boldsymbol{L}$	$\begin{bmatrix}223.6386\\ 7.1040\end{bmatrix}$	$\begin{bmatrix}223.6250\\ 4.0704\end{bmatrix}$	$\begin{bmatrix}223.6261\\ 4.3152\end{bmatrix}$	$\begin{bmatrix}223.6245\\ 3.9588\end{bmatrix}$	$\begin{bmatrix}223.6357\\ 6.4713\end{bmatrix}$
$G_f(s)$	$1/(0.01s+1)$				

Table 4.8: Disturbed response $|y(j\omega_d)|$ of actuator extension (mm) from the setpoint when subjected to the equivalent disturbing input $|d_e(j\omega_d)|$

	Actuator B	Actuator L	Actuator M	Actuator N	Actuator O
$\|y(jw_d)\|$	0.0579	0.0760	0.0896	0.0445	0.0366

Table 4.9: Stability robustness index β (dB) of the individual SISO closed-loop system for each actuator

	Actuator B	Actuator L	Actuator M	Actuator N	Actuator O
β	-4.1505	-3.2773	-2.9813	-2.7267	-3.2234

Table 4.10: Parameters of the PID controller based on actuator dynamics

	Actuator B	Actuator L	Actuator M	Actuator N	Actuator O
K_P	10.5681	9.7584	10.6623	9.3291	11.8064
K_I	0.8014	0.8118	0.8107	0.7075	1.0048
K_D	0.2580	-0.0108	0.0835	-0.1027	0.1627
N	18.4316	9.5057	8.6948	90.8428	16.7530

K_P – Proportional gain; K_I – Integral gain; K_D – Derivative gain; N – Filter coefficient

Figure 4.22 illustrates a high-lift scenario, in which the real-time trajectory for each actuator to follow so as to complete the morphing process is calculated according to Eq (2.19) in Section 2.1 and is each plotted in Figure 4.23.

Tests are divided into two groups:

- **Group 1**: Using Category I models as plant dynamics
  This simulates the situation free from wing structural dynamics. That is, actuators are not assembled onto the wing rib body framework.
- **Group 2**: Using Category II models as plant dynamics
  This simulates the situation that actuators are assembled onto the wing rib body framework with skin on (Figure 2.3 (c)). In other words, the actuators are subjected to wing structural dynamics.

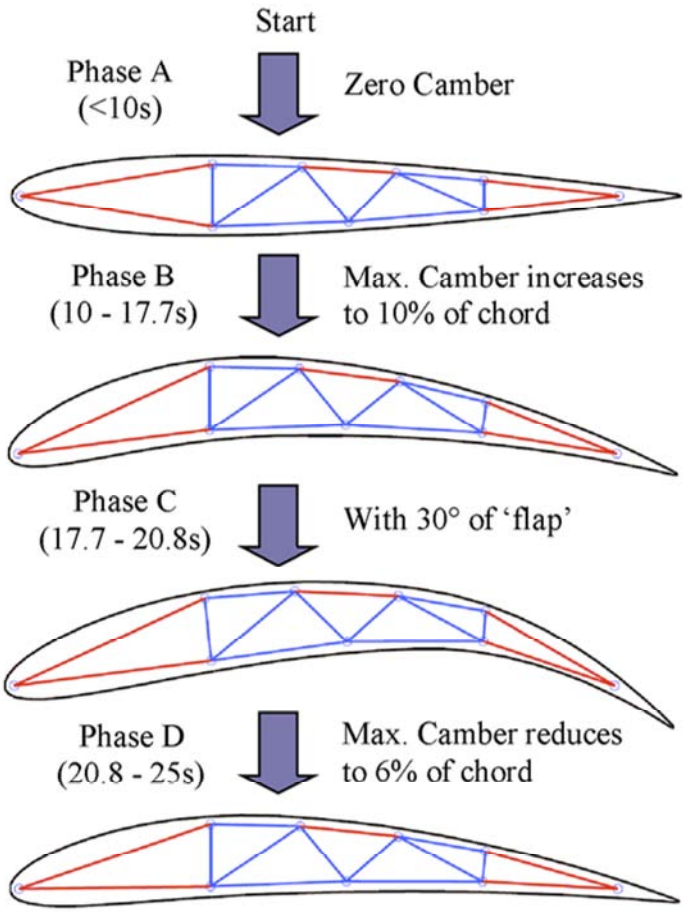

Figure 4.22: ATBMW morphing process in a high-lift scenario

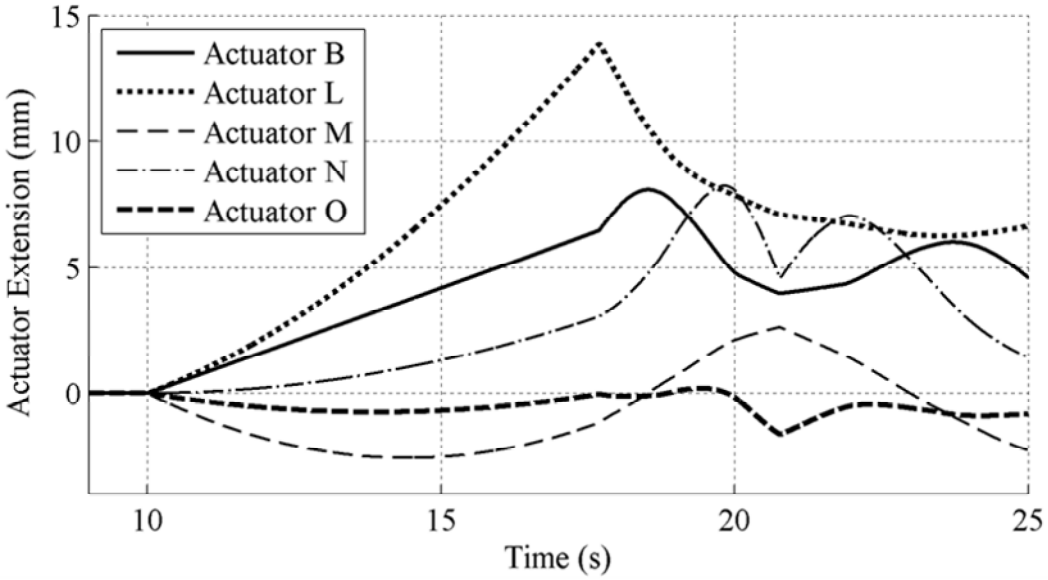

Figure 4.23: Reference length trajectory of actuators for accomplishing the ATBMW morphing process in a high-lift scenario

Similar to Section 4.1.3, the sampling rate in simulation is set to 0.001 second, and results are analysed in terms of the deviation described by

$$\begin{cases} \alpha_I = \left(\frac{1}{n} \sum_{i=1}^{n} \left(y_I^{(i)} - r^{(i)} \right)^2 \right)^{\frac{1}{2}} \\ \alpha_{II} = \left(\frac{1}{n} \sum_{i=1}^{n} \left(y_{II}^{(i)} - y_I^{(i)} \right)^2 \right)^{\frac{1}{2}} \end{cases}, \tag{4.6}$$

where

$r^{(i)}$: The i^{th} point of the reference trajectory;

$y_I^{(i)}$: The i^{th} point of Group 1 tracking trajectory;

$y_{II}^{(i)}$: The i^{th} point of Group 2 tracking trajectory;

α_I: Deviation of Group 1 tracking trajectory from the reference trajectory;

α_{II}: Deviation of Group 2 tracking trajectory from Group 1 tracking trajectory;

n: Number of samples.

Comparisons are made according to the relative tracking error

$$\Delta = \frac{\alpha_{II}}{\alpha_I} \times 100\% . \tag{4.7}$$

As can be seen from the results summarised in Table 4.11, un-modelled wing structural dynamics have substantial influence on the actuator response, resulting in relative tracking errors of various extents when using the PID controller. However, the UIE-integrated LQG controller has better performance with little difference between Group 2 and Group 1 tracking trajectories in spite of the mismatch between models used by the controller and those used as plant dynamics.

Figures in Table 4.11 also vary among different actuators in a similar pattern with regard to both the PID controller and the UIE-integrated LQG controller. Actuators L and M appear to suffer minor impacts from induced wing structural dynamics, while the other actuators are each in a position subjected to more uncertainties, especially

actuator B. This phenomenon implies the complexity and uncertainty of wing structural dynamics, which are thus difficult to accurately model, especially when the ATBMW structure becomes more complicated.

Table 4.11: Relative tracking errors under the PID controller and the UIE-integrated LQG controller designed according to actuator dynamics

	Actuator B	Actuator L	Actuator M	Actuator N	Actuator O
Δ_1	64.43%	39.99%	11.60%	53.41%	36.48%
Δ_2	4.87%	3.66%	0.82%	5.78%	4.25%

Subscript "1": PID controller based on actuator dynamics
Subscript "2": UIE-integrated LQG controller based on actuator dynamics

Therefore, the results suggest:

- The un-modelled wing structural dynamics can be effectively estimated and properly treated using the UIE-integrated LQG controller designed according to actuator dynamics, which performs consistently as designed despite the variation of plant dynamics.
- With the UIE-integrated LQG controller, the difficulties in acquiring sophisticated models of wing structural dynamics for actuator controller design can be avoided. As a result, the implementation of the actuator controller for ATBMWs can be simplified.

Chapter 5

WIND TUNNEL EXPERIMENTS

It is shown in Section 4.3 that the un-modelled wing structural dynamics are well compensated by the UIE-integrated LQG controller based on actuator dynamics, the real-time trajectory tracking performance of which is better than the PID controller. In addition to the induced dynamics from the wing structure, aerodynamic loads during flight are another major factor influencing the actuator response. In order to investigate the performance of the UIE-integrated LQG controller in flight environments, wind tunnel tests were conducted. The arrangement of laboratory apparatus is introduced in Section 5.1, followed by descriptions in Section 5.2 on the tests conducted. The results of wind tunnel experiments are presented and discussed in Section 5.3.

5.1 Experiment Setup

In experiments, controllers were designed in Matlab®, realised via Simulink®, and implemented through dSPACE®. As mentioned in Section 3.1, each actuator is controlled by an individual controller. The corresponding SISO control system is implemented with the hardware setup illustrated in Figure 5.1 (see detailed technical information in Table A.1 of Appendix A). The overall experiment setup with a wind tunnel is shown in Figure 5.2. The prototype was vertically mounted in the wind tunnel duct (Figure 5.3 (a)) with the other end of its spar fixed to the JR3® Multi-Axis Force-Torque Sensor (Figure 5.3 (b)). Forces and torques data collected by the

sensor receiver was then converted into lift and drag forces. The wind speed was measured by a Pitot tube connected to a flow meter.

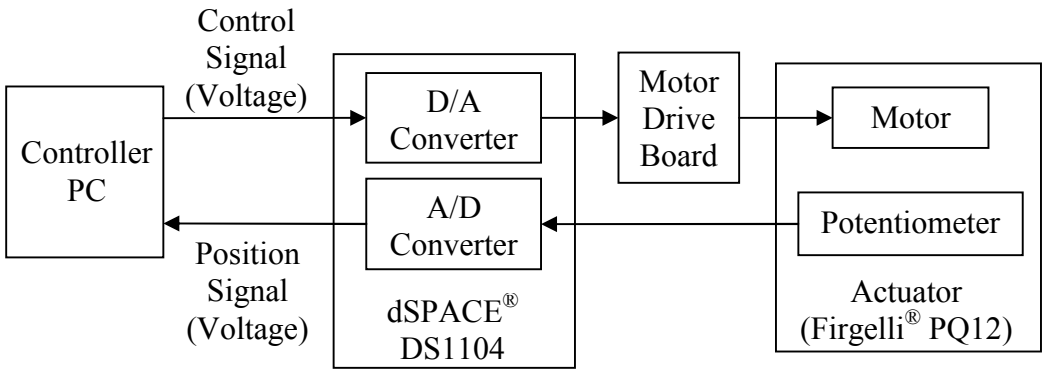

Figure 5.1: Schematic of the hardware setup for controller implementation

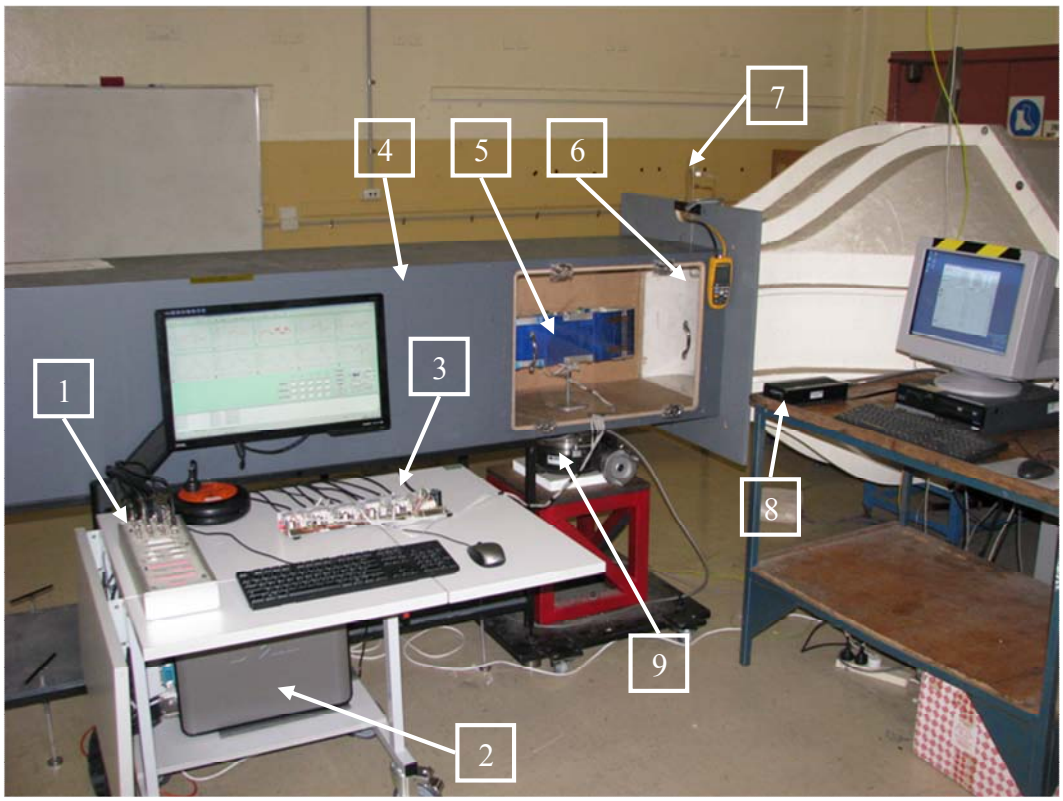

1, dSPACE® DS1104 R&D Controller Board; 2, Controller PC; 3, Motor Drive Board; 4, Wind Tunnel Duct; 5, ATBMW Prototype; 6, Flow Meter; 7, Pitot Tube; 8, JR3® Multi-Axis Force-Torque Sensor; 9, JR3® Serial Force-Torque Sensor Receiver

Figure 5.2: Setup for wind tunnel tests

Though equipped with instruments to measure lift and drag forces generated by the ATBMW prototype, the setup was not used to investigate differences in the

aerodynamic performance resulted from the use of different control schemes, and did not provide force feedback to the controller. Therefore, aerodynamic loads remain unknown to the controller. Instead, measured force data is used to visualise the time-varying dynamic pressure change which the ATBMW prototype was subjected to, and to help identify how actuator responses are affected by the wind.

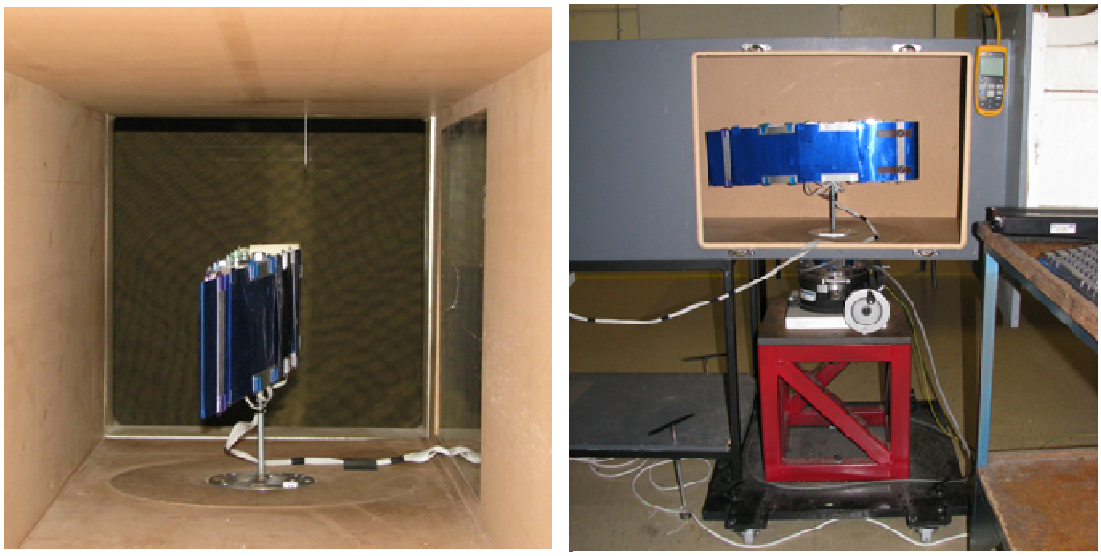

(a) ATBMW prototype in the wind tunnel duct

(b) ATBMW prototype mounted on the JR3® Multi-Axis Force-Torque Sensor

Figure 5.3: ATBMW installation in the wind tunnel

The reason for this arrangement is as follows. The flexible skin for ATBMWs is still one of the unsolved research questions among various types of the morphing wing technology, and to the best of our knowledge, there is not a completely feasible solution for the ATBMW. The sliding aluminium skin used on our prototype enables it to undergo wind tunnel tests but is not able to maintain consistent aerodynamic characteristics (Thill et al., 2008). As a result, the measured lift and drag forces generated from the ATBMW prototype may not genuinely distinguish one controller from another when the wind speed is not high enough. However, simply raising the wind speed to higher levels is impractical within the scope of the project documented herein, as the skin used cannot sustain the quadratically increased dynamic pressures at high wind speeds. According to Austin et al. (1994), significant improvements in aerodynamic performance may result from tiny shape changes of the wing, or in other words, minor length variations of ATBMW actuators, during a transonic flight.

Therefore, robust real-time trajectory tracking in the presence of unpredicted and unmeasured aerodynamic loads is of vital importance, and the tracking trajectory of actuators, as an alternative to aerodynamic measurements, can be examined directly to evaluate controller performance. In this way, controllers can be compared in terms of performance robustness at relatively low wind speeds.

5.2 Tests Arrangement

In experiments, there exist unknown inputs of various types, with their corresponding equivalent representation at the control input not available for measurement. As a result, looking into the estimated equivalent of unknown inputs gives few indications of the effect of unknown-input compensation. The same as simulations, and also as explained in the foregoing section, relative tracking errors provide a straightforward alternative for performance evaluation, and thus are used as a major measure in experiments as well.

Two scenarios were assumed:

- **Case 1**: The same high-lift scenario as in Figure 4.22
- **Case 2**: Worst-case scenario
  According to Table 4.11 and Figure 2.3 (a), actuator B is believed to be most sensitive to internal uncertainties of the structure and external loads on the wing given its location in the entire framework. To further investigate the disturbance rejection capacity of the proposed control scheme, actuators N and O were commanded to flap the trailing edge at a rate of 0.4π (rad/s) to generate fluctuating lift forces, while actuator B extended to 6mm and then retracted back to its original length following the trajectory of $6\sin(\pi t/15-\pi/2)$ within 30 seconds. This scenario simulates the situation that an aircraft is operating in severe weather conditions and needs to respond fast enough to unpredictable gust wind in order to maintain stable flight (the corresponding reference trajectories for actuators to follow could be more complicated than the formulation herein).

For each scenario, tests were divided into two groups:

- **Group 1**: no wind
- **Group 2**: room temperature, 8° angle of attack, and 20m/s wind speed

Each group consists of three sets of tests:

- **Test A**: Using the UIE-integrated LQG controller designed according to actuator dynamics

  Parameters in Table 4.7 were used directly in tests without further tuning.
- **Test B**: Using the UIE-integrated LQG controller designed according to wing structural dynamics

  When wing structural dynamics are taken into account in controller design, fewer control efforts are needed to compensate internal uncertainties, and more stability margins are available to allow for unmeasured aerodynamics loads. The results from this controller therefore give a reliable reference to evaluate the performance of the UIE-integrated LQG controller designed purely according to actuator dynamics in Test A.

  The same requirements on the disturbed response $|y(j\omega_d)|$ and stability robustness index β as the designs based on actuator dynamics are followed. With the weighting coefficients and matrixes in Table 5.1, corresponding gains are obtained and listed in Table 5.2. Note that the disturbed responses in Table 5.3 are comparable to those in Table 4.8, while Table 5.4 indicates better stability robustness of every individual SISO closed-loop system than Table 4.9 does.
- **Test C**: Using the PID controller based on wing structural dynamics

  The PID controller based on actuator dynamics was not used in wind tunnel experiments, because it has been shown not able to cope well with modelling errors compared with the UIE-integrated LQG controller. Instead, an optimised and well-tuned design (see Table 5.5) considering wing structural dynamics underwent tests to provide a solid reference for comparison.

Table 5.1: Weights used in the UIE-integrated LQG controller design based on wing structural dynamics

	Q_y	Q_w	$\boldsymbol{Q}_l$	$\boldsymbol{Q}_d$
Actuator B	4×10^{2}	1×10^{-3}	$\begin{bmatrix}5\times10^{4} & 0\\ 0 & 5\times10^{4}\end{bmatrix}$	$\begin{bmatrix}1.2\times10^{10} & 0\\ 0 & 1.2\times10^{10}\end{bmatrix}$
Actuator L	2.8×10^{2}	1×10^{-3}	$\begin{bmatrix}5\times10^{4} & 0\\ 0 & 5\times10^{4}\end{bmatrix}$	$\begin{bmatrix}5\times10^{10} & 0\\ 0 & 5\times10^{10}\end{bmatrix}$
Actuator M	2.5×10^{2}	1×10^{-3}	$\begin{bmatrix}5\times10^{4} & 0\\ 0 & 5\times10^{4}\end{bmatrix}$	$\begin{bmatrix}7\times10^{9} & 0\\ 0 & 7\times10^{9}\end{bmatrix}$
Actuator N	4×10^{2}	1×10^{-3}	$\begin{bmatrix}5\times10^{4} & 0\\ 0 & 5\times10^{4}\end{bmatrix}$	$\begin{bmatrix}1.8\times10^{10} & 0\\ 0 & 1.8\times10^{10}\end{bmatrix}$
Actuator O	3.7×10^{2}	1×10^{-3}	$\begin{bmatrix}5\times10^{4} & 0\\ 0 & 5\times10^{4}\end{bmatrix}$	$\begin{bmatrix}2.5\times10^{8} & 0\\ 0 & 2.5\times10^{8}\end{bmatrix}$

(R_η, R_l, and R_d used in the design of each actuator controller are all set to 1.)

Table 5.2: Parameters of the UIE-integrated LQG controller designed according to wing structural dynamics

	Actuator B	Actuator L	Actuator M	Actuator N	Actuator O
K_r	20.0039	16.7363	15.8148	20.0032	19.2388
K_w	–0.0316	–0.0316	–0.0316	–0.0316	–0.0316
$\boldsymbol{K}_x$	$\begin{bmatrix}20.1627\\ 0.3058\end{bmatrix}^T$	$\begin{bmatrix}16.8125\\ 0.2721\end{bmatrix}^T$	$\begin{bmatrix}15.8884\\ 0.3466\end{bmatrix}^T$	$\begin{bmatrix}20.0181\\ 0.4462\end{bmatrix}^T$	$\begin{bmatrix}19.2489\\ 0.7318\end{bmatrix}^T$
K_d	51.6267	37.4112	33.4911	70.7653	89.8030
$\boldsymbol{L}$	$\begin{bmatrix}223.6328\\ 5.8186\end{bmatrix}$	$\begin{bmatrix}223.6258\\ 4.2595\end{bmatrix}$	$\begin{bmatrix}223.6262\\ 4.3431\end{bmatrix}$	$\begin{bmatrix}223.6190\\ 2.7283\end{bmatrix}$	$\begin{bmatrix}223.6312\\ 5.4577\end{bmatrix}$
$G_f(s)$	$1/(0.01s+1)$				

Table 5.3: Disturbed response $|y(j\omega_d)|$ of actuator extension (mm) from the setpoint when subjected to the equivalent disturbing input $|d_e(j\omega_d)|$

	Actuator B	Actuator L	Actuator M	Actuator N	Actuator O
$\lvert y(j\omega_d)\rvert$	0.0571	0.0726	0.0884	0.0421	0.0348

Table 5.4: Stability robustness index β (dB) of the individual SISO closed-loop system for each actuator

	Actuator B	Actuator L	Actuator M	Actuator N	Actuator O
β	-1.6970	-2.0248	-2.2069	-2.3581	-2.4643

Table 5.5: Parameters of the PID controller based on wing structural dynamics

	Actuator B	Actuator L	Actuator M	Actuator N	Actuator O
K_P	18.6129	13.2856	12.9677	15.6642	14.9403
K_I	1.5578	1.1327	1.0769	1.2336	1.1524
K_D	-0.2937	-0.1657	-0.1369	-0.2079	-0.0016
N	9.5523	9.7332	9.4826	8.9909	8.8148

K_P – Proportional gain; K_I – Integral gain; K_D – Derivative gain; N – Filter coefficient

Every single test were repeated for 4 times to ensure data consistency, and results are averaged accordingly for subsequent treatments that use Eqs (4.6) and (4.7). Most importantly, all actuators were ensured to work within the nominal capacity in all tests.

5.3 Results and Discussions

5.3.1 Case 1: High-lift Scenario

(1) Main Results

Table 5.6 summarises the results from the high-lift scenario tests. The UIE-integrated LQG controllers used in Tests A and B both outperform the PID controller of Test C, with the relative tracking error several times smaller than that of PID. Though PID controllers were optimally designed using Category II models and further finetuned on board, there are nevertheless considerable performance downgrades caused by aerodynamic loads. In addition, the tracking performance of the UIE-integrated LQG controller designed using actuator dynamics (Δ_A) is closely comparable to that of its congener based on wing structural dynamics (Δ_B). Two main implications can be drawn from the results. Firstly, unmeasured aerodynamic loads can be effectively compensated under the UIE-integrated LQG controller; Secondly, using only the actuator dynamics for the UIE-integrated LQG controller design suffices, with the influences from wing structural dynamics effectively suppressed. It is worth emphasis that although the PID controller used in experiments for each actuator has already taken induced structural dynamics into account, there are nonetheless

considerable relative tracking errors. Furthermore, it is difficult to acquire models as in Category II via system identification or direct mathematical modelling due to highly interacted mechanical components, when the ATBMW has a sophisticated framework as in the work of Baker and Friswell (2009). Therefore, the advantages of using the UIE-integrated LQG controller for ATBMWs are manifest.

Table 5.6: Relative tracking errors in Tests A, B, and C of Case 1

	Actuator B	Actuator L	Actuator M	Actuator N	Actuator O
Δ_A	7.9%	2.7%	5.8%	5.9%	11.3%
Δ_B	7.3%	2.9%	5.5%	4.3%	11.3%
Δ_C	79.1%	16.1%	18.5%	31.8%	65.1%

Subscript "*A*": UIE-integrated LQG controller based on actuator dynamics
Subscript "*B*": UIE-integrated LQG controller based on wing structural dynamics
Subscript "*C*": PID controller based on wing structural dynamics

From Table 5.6 we can see that the resultant equivalent inputs from aerodynamic loads and modelling errors have less influence on actuators L, M, and N, but have more impact on actuators B and O. The figures in the table thus once again provide concrete evidence of the complicated structural dynamics on ATBMWs, besides the facts in Table 4.11.

With the measurements in the wind tunnel, the lift coefficient C_L of the ATBMW prototype can be obtained according to

$$C_L = \frac{2F_L}{\rho v_a^2 a_w}, \tag{4.8}$$

where F_L is the lift force, ρ is the density of air, v_a is the velocity of air, and a_w is the planform area of the ATBMW prototype.

Figure 5.4 shows a lift coefficient curve of the ATBMW prototype during the shape morphing process illustrated in Figure 4.22 (Case 1 scenario), reflecting a common pattern of the lift force resulted from the actuator trajectories in Figure 4.23.

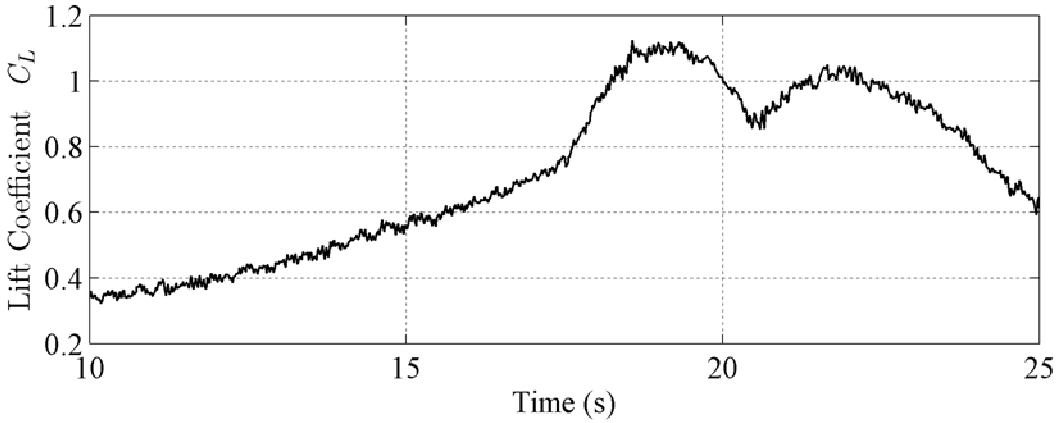

Figure 5.4: Lift coefficient of the ATBMW prototype in Case 1 tests

By referring to the framework of the ATBMW prototype (see Figure 2.3 (a)) from the perspective of mechanics and according to Figure 5.4, some connections between the lift force and actuator action are identified as follows:

- Actuators L and M at the leading edge contribute little to the variation in lift force because of the particular position of the spar and the fixed angle of attack in wind tunnel tests. The nose-down movement of the leading edge increases the overall camber and plays a major role in redirecting and smoothing the flow, but induces little rise of the lift force at the fixed angle of attack (8°) in tests. As a result, the air pressure exerted on the two actuators is much lower compared with actuator B, and has less disturbing effect on actuator trajectory tracking.
- The rear half of the prototype is supported by actuator B and hinge 6 (Node 6), and hence actuator B has to sustain a considerable portion of the lift force, especially at a large camber. For instance, the second peak of the lift coefficient curve is not as high as the first one in Figure 5.4, but the resultant axial push on actuator B is stronger according to mechanics analysis.
- The two times of length increase of actuator B does not exactly match the rises of lift force in terms of the time, and in particular the second peak of the lift coefficient happens earlier than the extending of actuator B. This is because another significant portion of the lift force is contributed by the motion of the trailing edge, powered by actuators N and O. As can be seen in Figures 4.23 and 5.4, the curve of lift coefficient appears in a similar pattern

to the trajectory of actuators B and N. The highest lift force results when the trajectories of actuators B and N intersect at around 19.2s. As actuator B gradually extends during the period between 20.8s and 21.9s, the coordinated action of actuators N and O further bends down the trailing edge at a faster rate. Accordingly, the overall camber continues to increase, once again raising the lift coefficient to a second peak before actuator B reaches 6mm.

- Regardless of the considerable contribution from the trailing edge on lift force generation, the aerodynamic pressure supported by actuators N and O is relatively low compared with actuator B because the former two actuators are located near the end of the wing rib.

In the following, the lift coefficient curve is used as an aid to qualitatively analyse the trajectory tracking results of actuators B and O (Figures 5.5 to 5.12), the two actuators subjected to greater impact from aerodynamic loads and modelling errors as mentioned before.

In Figure 5.5 are two tracking trajectories of actuator B under PID control designed according to wing structural dynamics, with one recorded in a no-wind environment (Group 1 test) and the other obtained in wind (Group 2 test). The relative tracking deviation (see the definition on page 72) is plotted accordingly in Figure 5.8. There is no significant deviation between the two trajectories when actuator B gradually extends at small cambers (Phase B) or retracts following the axial push from the lift force (19s to 20.8s in Phase C), whereas evident response delays of actuator B occur under high lift forces at large cambers (16.5s to 19s in Phase C, and throughout Phase D). Similarly, lags of actuator O are observed after 17.7s (the lift force becomes higher) when the actuator needs to overcome the aerodynamic load to retract (Figures 5.9 and 5.12).

Under the UIE-integrated LQG controller designed on actuator dynamics, actuator B had consistent performance in spite of the presence of unmeasured and time-varying aerodynamic loads, with the corresponding tracking trajectory (Group 2 test) closely coinciding with the one obtained in a no-wind condition (Group 1 test), as shown in Figure 5.6. Using wing structural dynamics for the UIE-integrated LQG controller design, as a reference, yielded similar results (see Figure 5.7). The same conclusion

can be drawn on the performance of actuator O, as shown in Figures 5.10 and 5.11. The results imply that the performance of the UIE-integrated LQG controller based on actuator dynamics is satisfactory, and more importantly, at the same level of that of its congener using wing structural dynamics (see Figures 5.8 and 5.12).

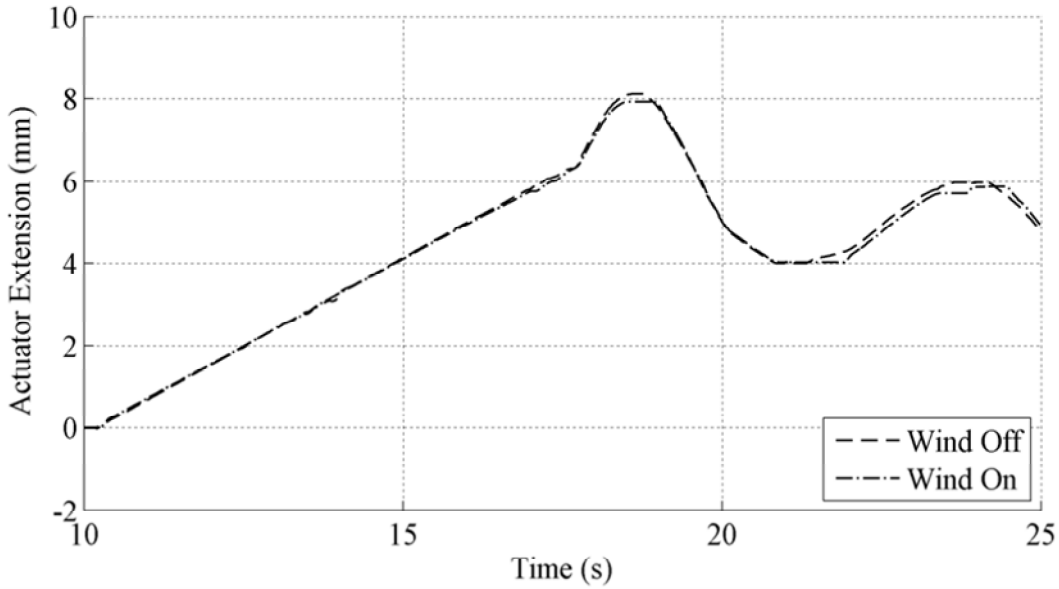

Figure 5.5: Tracking trajectories of actuator B in Case 1 using the PID controller based on wing structural dynamics (Test C)

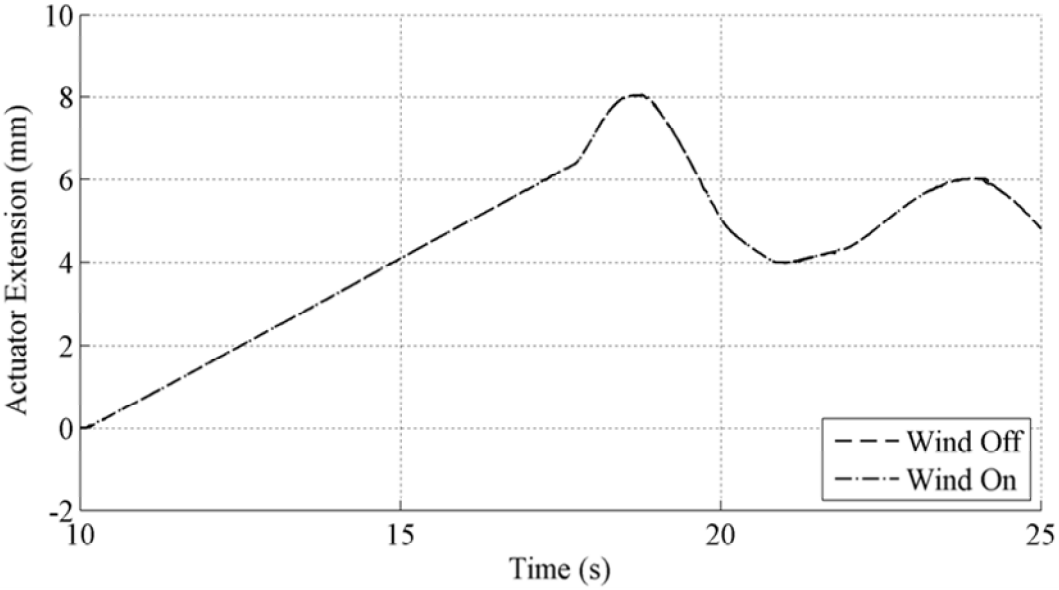

Figure 5.6: Tracking trajectories of actuator B in Case 1 using the UIE-integrated LQG controller based on actuator dynamics (Test A)

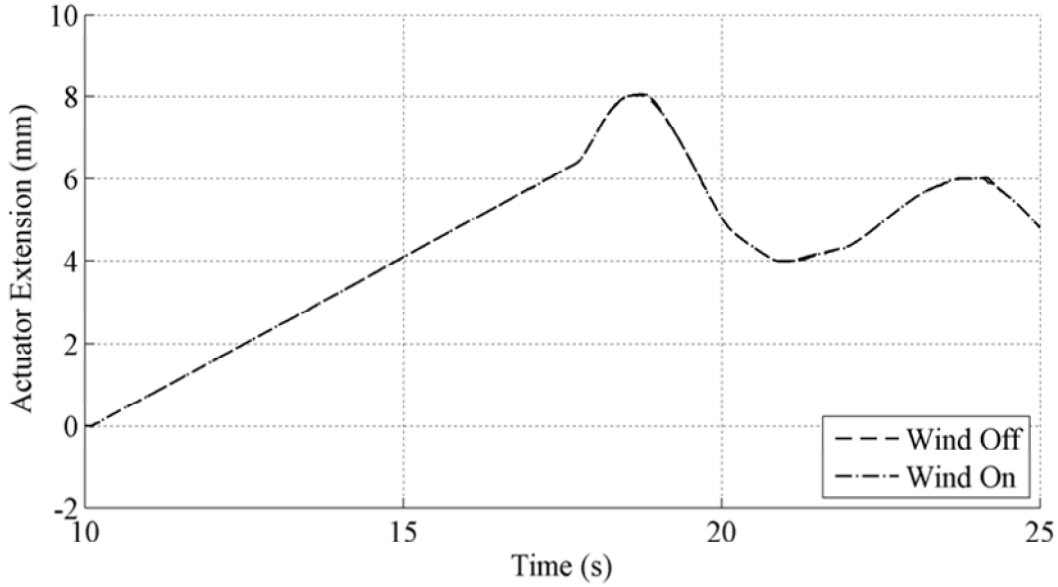

Figure 5.7: Tracking trajectories of actuator B in Case 1 using the UIE-integrated LQG controller based on wing structural dynamics (Test B)

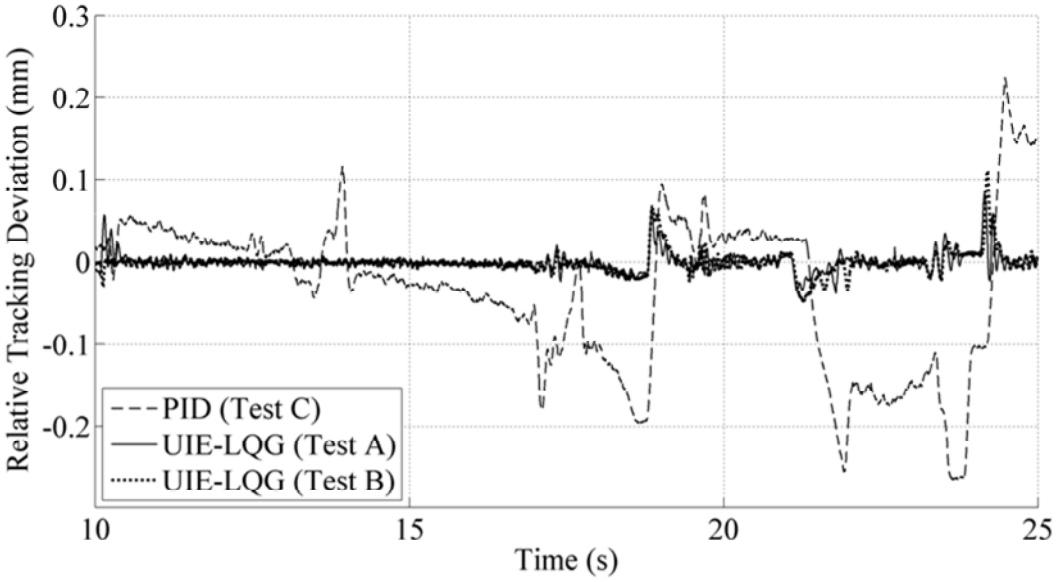

Figure 5.8: Relative tracking deviations in Tests A, B, and C

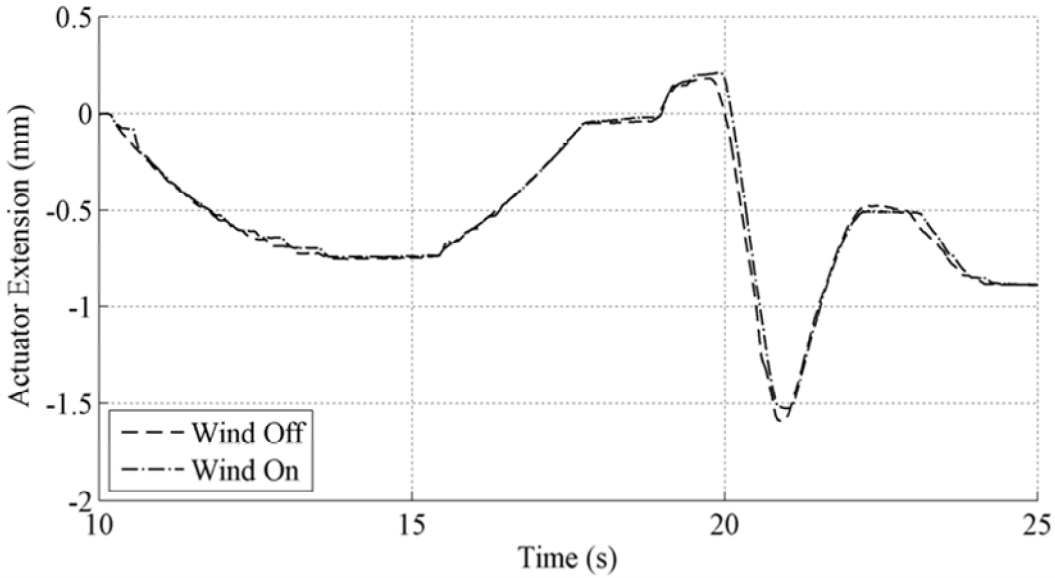

Figure 5.9: Tracking trajectories of actuator O in Case 1 using the PID controller based on wing structural dynamics (Test C)

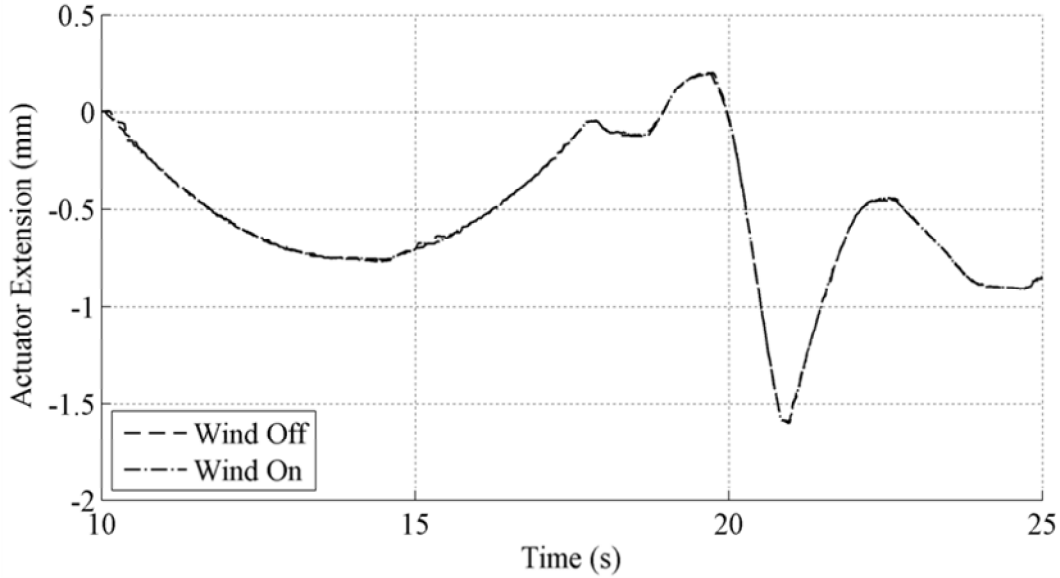

Figure 5.10: Tracking trajectories of actuator O in Case 1 using the UIE-integrated LQG controller based on actuator dynamics (Test A)

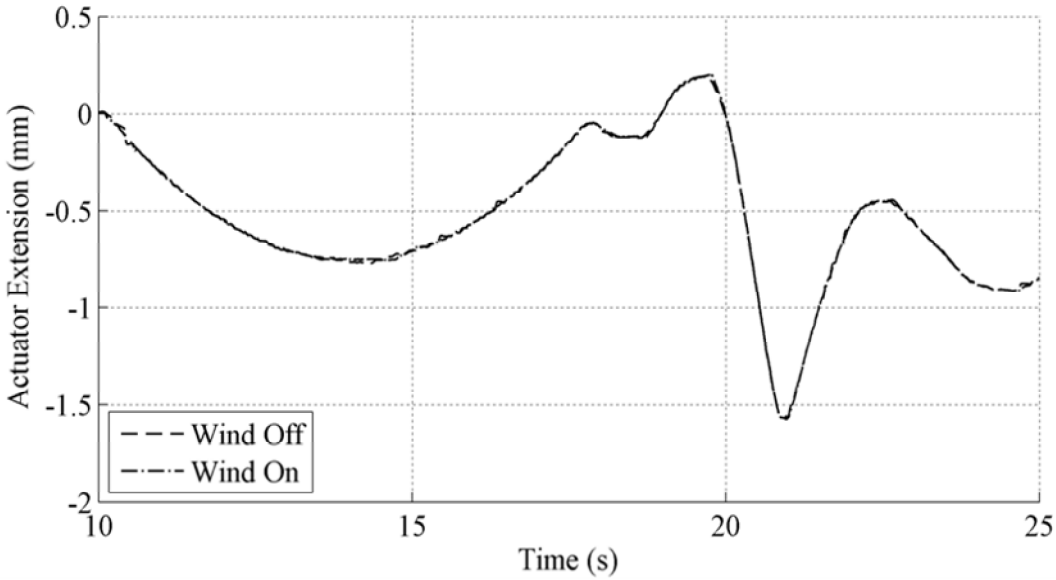

Figure 5.11: Tracking trajectories of actuator O in Case 1 using the UIE-integrated LQG controller based on wing structural dynamics (Test B)

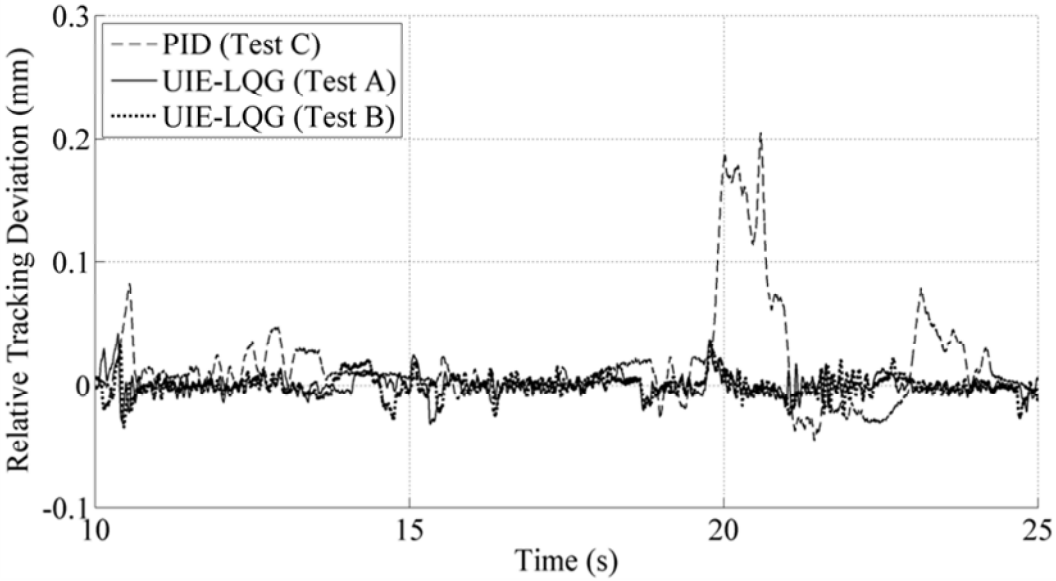

Figure 5.12: Relative tracking deviations in Tests A, B, and C

(2) Actuator Precision Influence on Tracking Errors

The actuators used on the ATBMW prototype each has an embedded potentiometer for linear position feedback, the positioning precision of which is limited to 0.1mm as claimed by the manufacturer (see Table A.2 in Appendix A). In order to evaluate the effects of actuator precision on experiment results, any two of the four runs, $4!/(4-2)!=12$ pairs in total in every single test, are compared by following the same treatment using Eqs (4.6) and (4.7), with results averaged and listed in Table 5.7.

As can be seen in Table 5.7, the relative tracking errors of each actuator due to the limited actuator positioning precision are consistent in spite of different controllers used. In addition, reference trajectories also have an impact on the relative tracking error, which becomes larger when the range of a trajectory is getting smaller. For instance, actuator O has the largest relative tracking error among the five actuators while actuator L has the smallest. This is because the total length variation (range of trajectory) of actuator O is only 2mm, merely 20 times of the rated positioning precision of the actuator. As a direct consequence, the trajectory discretization of actuator O is much coarser than that of actuator L, and some unsmooth stair-like sections can be observed along the trajectories of actuator O under both the PID and UIE-integrated LQG controllers (Figures 5.9 to 5.11) when the speed of length variation is low. Nevertheless, the UIE-integrated LQG controller demonstrates better capability in mitigating the impact from the limited actuator precision, with smoother tracking trajectories than those under the PID controller.

Table 5.7: Relative tracking errors due to limited actuator positioning precision

	Actuator B	Actuator L	Actuator M	Actuator N	Actuator O
Δ'_A	3.4%	2.3%	5.0%	3.3%	11.0%
Δ'_B	3.3%	2.4%	4.7%	3.1%	10.9%
Δ'_C	3.8%	2.6%	5.2%	3.6%	11.2%

Subscript "*A*": UIE-integrated LQG controller based on actuator dynamics
Subscript "*B*": UIE-integrated LQG controller based on wing structural dynamics
Subscript "*C*": PID controller based on wing structural dynamics

By examining and comparing the corresponding values in Tables 5.6 and 5.7 in pairs (for example, Δ_A and Δ'_A of actuator B forms a pair, and so forth), we can see that actuator B is relatively more sensitive to exogenous unknown inputs than the other actuators, with its relative tracking errors Δ_A and Δ_B approximately twice of the one caused purely by the limited actuator precision while little differences are found in the other pairs. The finding agrees with our statement regarding the critical position of actuator B when describing Case 2 scenario in Section 5.2. And it is acceptable that actuator O has relative tracking errors (Δ_A and Δ_B) around 11% when using UIE-integrated LQG controllers, given the achievable minimum relative tracking error around 11% in Table 5.7.

5.3.2 Case 2: Worst-case Scenario

In tests, the commanded shape morphing of the ATBMW prototype has its lift coefficient in the pattern shown in Figure 5.13. The action of actuator B contributes to the major change in lift while fluctuating waves are caused by the flapping of the trailing edge.

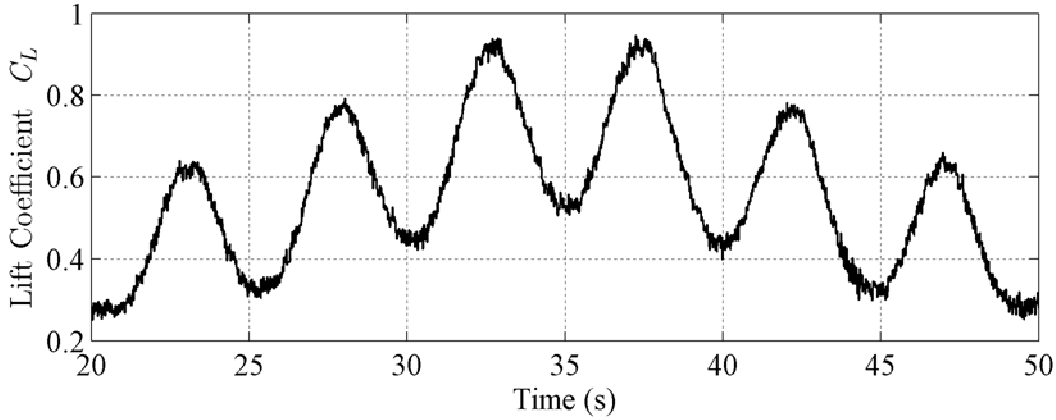

Figure 5.13: Lift coefficient of the ATBMW prototype in Case 2 tests

The tracking results under different controllers are plotted in Figures 5.14, 5.15, and 5.16, respectively, with the relative tracking deviations (see the definition on page 72) shown in Figure 5.17. We can see that the tracking performance of the PID controller is affected by the disturbances generated by the trailing edge when the lift coefficient is rising ($t < 35\,\mathrm{s}$). The three times of significant trajectory deviations accompany

the three consecutive peaks of the lift coefficient curve. However, such phenomena can be barely identified in the results of the UIE-integrated LQG controller designed according to actuator dynamics (see Figure 5.15) which are again closely comparable to those of its congener design based on wing structural dynamics (Figure 5.16).

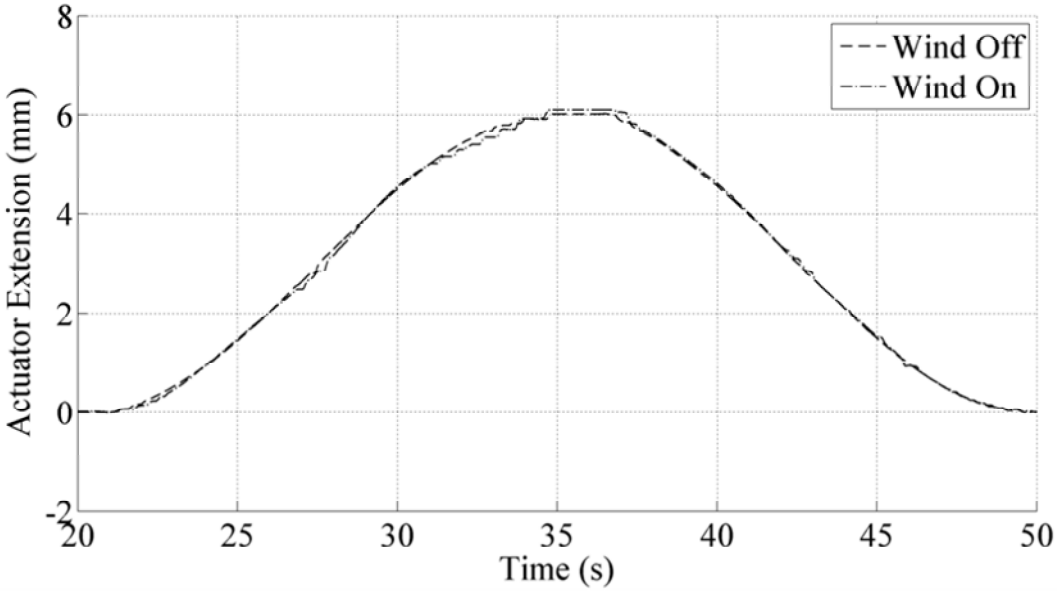

Figure 5.14: Tracking trajectories of actuator B in Case 2 using the PID controller based on wing structural dynamics (Test C)

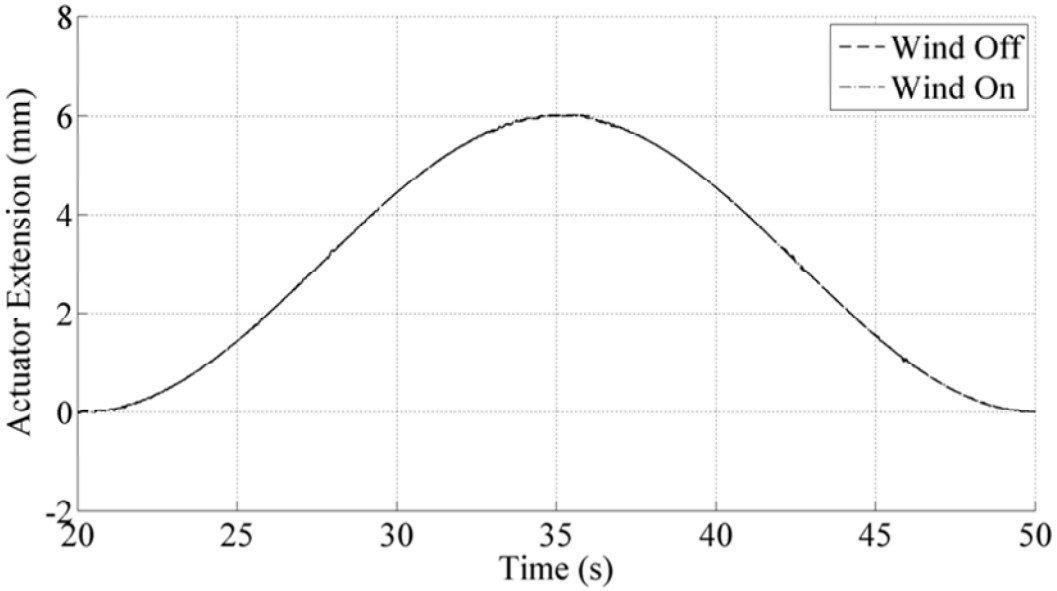

Figure 5.15: Tracking trajectories of actuator B in Case 2 using the UIE-integrated LQG controller based on actuator dynamics (Test A)

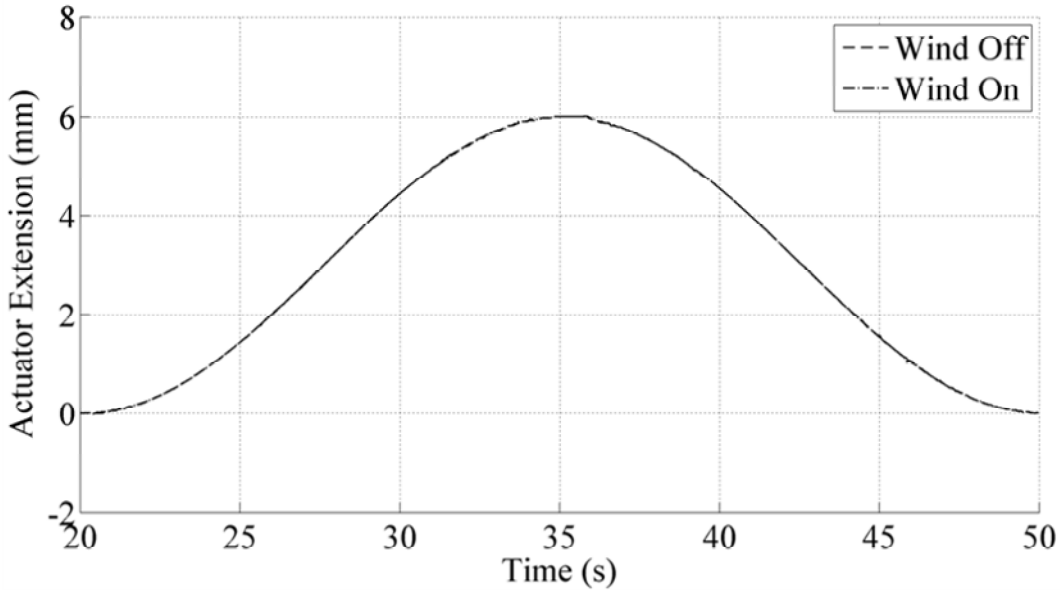

Figure 5.16: Tracking trajectories of actuator B in case 2 using the UIE-integrated LQG controller based on wing structural dynamics (Test B)

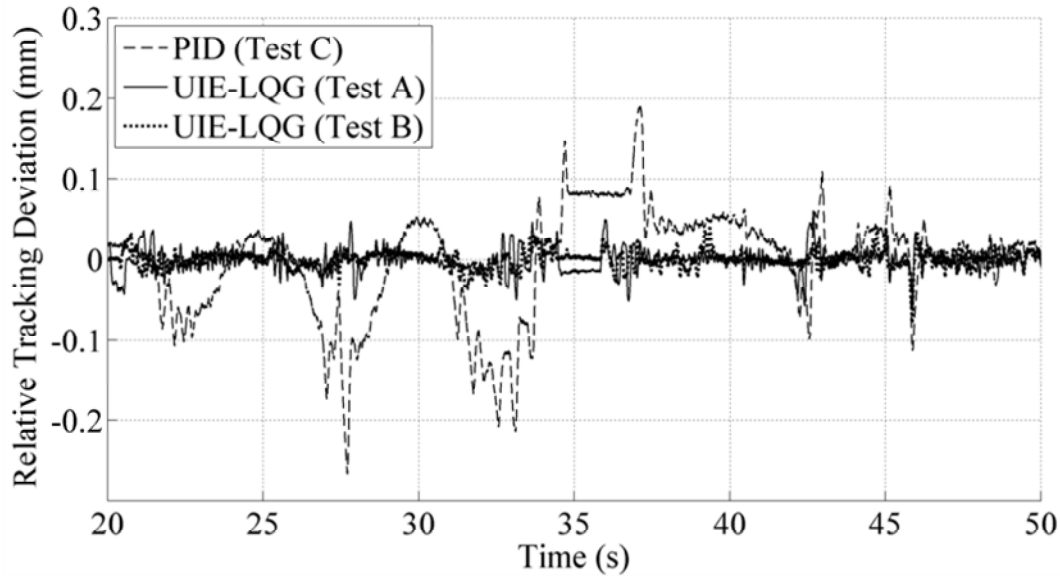

Figure 5.17: Relative tracking deviations in Tests A, B, and C

Chapter 6

CONCLUSIONS

6.1 Outcomes of the Research

A robust actuator controller for ATBMWs is proposed, developed, and studied. The proposed UIE-integrated LQG controller, as validated in both simulations and wind tunnel experiments, is an effective solution to simplifying the implementation of actuator controllers on ATBMWs.

- Firstly, the UIE-integrated LQG controller is robust to a wide class of unknown inputs, including exogenous disturbances, and most importantly, internal uncertainties. As a result, there is no need to obtain wing structural dynamics for controller design, and the model of the actuator can be used instead. This is convenient because actuator dynamics are readily available from either the actuator manufacturer or via system identification methods. The actuator can then be tuned directly before it is installed on the ATBMW, and no further tuning is required for the controller after the actuator becomes part of the ATBMW framework, despite the fact that the dynamics of the overall structure is not covered in the actuator model used in controller design. It is thus of great significance to cases where on-board tuning of controllers is difficult due to highly interacted actuators on a sophisticated ATBMW framework.
- Secondly, the UIE-integrated LQG controller is simple in structure and straightforward in design. Well established rules for the standard LQG controller remain unchanged regardless of the incorporation of the UIE, and the separation principle still holds for the full-state feedback law and observer

design. As a new approach for estimating and compensating unknown inputs, the proposed UIE component integrated with the standard LQG controller works in a way that does not require detailed knowledge on unknown inputs, derivatives of measured outputs, inversion of plant dynamics, and parameter optimisation for stabilising purpose. It is worth emphasis that the UIE component itself has a simple framework, parameters of which have direct physical indications and can be finetuned intuitively according to the actual performance of the actuator.

Beyond the above merits, our proposed controller has broader significance in the following two aspects: (1) It provides a unified solution to simplifying actuator controller implementation on ATBMWs despite the variations and complexity of ATBMW structures, and is therefore significant to successful realisations of a wide range of promising ATBMW concepts; (2) The enhanced capacity of disturbance rejection is crucial to aerodynamic improvements achieved by ATBMWs as it ensures reliable performance of wing morphing in the presence of unmeasured and unpredictable exogenous loads.

6.2 Future Work

Within the scope of the research project documented herein, the development and implementation of the UIE-integrated LQG controller is focused on an SISO basis. However, as mentioned in Section 3.3.3, the formulae for the UIE component are not limited to SISO cases but also have potentials in MIMO situations, and the LQG algorithm is particularly suitable for MIMO circumstances as well. Given the above facts, the generalisation of the UIE-integrated LQG controller to MIMO applications is recommended for future work.

Appendix A

Table A.1: Hardware and software configuration of the PC-based control

Hardware	**Computer**	CPU: Intel® Core™2 Quad Processor Q9400 @ 2.66GHz RAM: 3.46GB
	D/A & A/D Converter	dSPACE DS1104 R&D Controller Board
	Motor Drive Board	Control Input Signal: -10V to +10V Control Output: -10V to +10V @300mA
Software	**Matlab**	7.5.0.342 (R2007b)
	dSPACE	dSPACE ControlDesk Developer Version 3.2.1
	RTI	Real-Time Interface to Simulink (RTI1104) 6.0
	MDBS	MotionDesk Blockset 1.3.9
	MLIB/MTRACE	MATLAB-dSPACE Interface Libraries 4.6.4
	DSSIMULINK	ControlDesk to Simulink Interface 3.2.1

Table A.2: Specifications of Firgelli® miniature linear actuator PQ12

Peak Power Point	27N @ 4mm/s
Peak Efficiency Point	14N @ 7mm/s
Max Speed (no load)	9mm/s
Max Force (lifted)	35N
Max Side Load	15N
Back Drive Force	60N
Stroke	20mm
Input Voltage	12 VDC
Stall Current	220mA @ 12V
Mass	15g
Operating Temperature	-10°C to +50°C
Positional Accuracy	±0.1mm
Lifetime	20,000 strokes, 20% Duty Cycle
Ingress Protection	IP-54
Feedback Potentiometer	1/8W Non - Buffered 10kΩ Potentiometer

(Data obtained from Firgelli Technologies Inc., Canada)

Bibliography

ANDERSON, J. D., JR. (2008) *Introduction to Flight*, McGraw-Hill.

ÅSTRÖM, K. J. & HÄGGLUND, T. (2006) *Advanced PID Control,* Research Triangle Park, NC, Instrumentation, Systems, and Automation Society.

AUSTIN, F., ROSSI, M. J., NOSTRAND, W. V., KNOWLES, G. & JAMESON, A. (1994) Static shape control for adaptive wings. *AIAA journal,* 32**,** 1895-1901.

BAKER, D. & FRISWELL, M. I. (2009) Determinate structures for wing camber control. *Smart Materials and Structures,* vol. 18**,** pp. 1-13.

BARNARD, R. H. & PHILPOTT, D. R. (2003) *Aircraft Flight*, Pearson Education Limited.

BOLONKIN, A. & GILYARD, G. B. (1999) Estimated benefits of variable-geometry wing camber control for transport aircraft. *NASA technical memorandum; 206586.* Edwards, Calif., Springfield, VA, National Aeronautics and Space Administration, Dryden Flight Research Center; National Technical Information Service, Distributor.

BORIA, F., STANFORD, B., BOWMAN, S. & IFJU, P. (2009) Evolutionary optimization of a morphing wing with wind-tunnel hardware in the loop. *AIAA JOURNAL,* Vol. 47**,** 399-409.

BRYSON, A. E. & HO, Y. C. (1969) *Applied Optimal Control: Optimization, Estimation, and Control*, Blaisdell Pub. Co.

BURL, J. B. (1998) *Linear Optimal Control*, Prentice Hall.

BUTT, J. R. (2005) A study of morphing wing effectiveness in fighter aircraft using exergy analysis and global optimization techniques. *Mechanical Engineering.* Blacksburg, Virginia, Virginia Polytechnic Institute and State University.

CHANG, J.-L. (2006) Applying discrete-time proportional Integral observers for state and disturbance estimations. *Automatic Control, IEEE Transactions on,* 51**,** 814-818.

CHENG, G. & PENG, K. (2007) Robust composite nonlinear feedback control with application to a servo positioning system. *Industrial Electronics, IEEE Transactions on,* 54**,** 1132-1140.

CHOI, Y., YANG, K., CHUNG, W. K., KIM, H. R. & SUH, I. H. (2003) On the robustness and performance of disturbance observers for second-order systems. *Automatic Control, IEEE Transactions on,* 48**,** 315-320.

COLE, J. B. (1981) Airplane wing trailing-edge flap-mounting mechanism. United States, The Boeing Company (Seattle, WA).

CORLESS, M. & TU, J. A. Y. (1998) State and input estimation for a class of uncertain systems. *Automatica,* 34**,** 757-764.

DADONE, P., LACARBONARA, W., NAYFEH, A. H. & VANLANDINGHAM, H. F. (2003) Payload pendulation reduction using a variable-geometry-truss architecture with LQR and fuzzy controls. *Journal of Vibration and Control,* 9**,** 805-837.

DAROUACH, M., ZASADZINSKI, M. & XU, S. J. (1994) Full-order observers for linear systems with unknown inputs. *Automatic Control, IEEE Transactions on,* 39**,** 606-609.

DAVISON, E. (1972) The output control of linear time-invariant multivariable systems with unmeasurable arbitrary disturbances. *Automatic Control, IEEE Transactions on,* 17**,** 621-630.

DAVISON, E. (1975) A generalization of the output control of linear multivariable systems with unmeasurable arbitrary disturbances. *Automatic Control, IEEE Transactions on,* 20**,** 788-792.

DIETZ, S. G. & SCHERER, C. W. (2010) Robust output feedback control against disturbance filter uncertainty described by dynamic integral quadratic constraints. *International Journal of Robust and Nonlinear Control,* 20**,** 1903-1919.

DOYLE, J. C., GLOVER, K., KHARGONEKAR, P. P. & FRANCIS, B. A. (1989) State-space solutions to standard H2 and H∞ control problems. *Automatic Control, IEEE Transactions on,* 34**,** 831-847.

DU, C., LI, H., THUM, C. K., LEWIS, F. L. & WANG, Y. (2010) Simple disturbance observer for disturbance compensation. *Control Theory & Applications, IET,* 4**,** 1748-1755.

FRANCIS, B. A. & WONHAM, W. M. (1975) The internal model principle for linear multivariable regulators. *Applied Mathematics & Optimization,* 2**,** 170-194-194.

FRANKLIN, G. F., POWELL, J. D. & EMAMI-NAEINI, A. (2010) *Feedback Control of Dynamic Systems*, Pearson.

GILBERT, W. W. (1981) Mission adaptive wing system for tactical aircraft. *Journal of Aircraft,* 18**,** 597-602.

GUAN, Y. & SAIF, M. (1991) A novel approach to the design of unknown input observers. *Automatic Control, IEEE Transactions on,* 36**,** 632-635.

HARA, S., YAMAMOTO, Y., OMATA, T. & NAKANO, M. (1988) Repetitive control system: a new type servo system for periodic exogenous signals. *Automatic Control, IEEE Transactions on,* 33**,** 659-668.

HETRICK, J. A., OSBORN, R. F., KOTA, S., FLICK, P. M. & PAUL, D. B. (2007) Flight testing of mission adaptive compliant wing. *48th AIAA/ASME/ASCE/AHS/ASC Structures, Structural Dynamics, and Materials Conference.* Waikiki, HI, United states, American Institute of Aeronautics and Astronautics Inc.

HOU, M. & MULLER, P. C. (1992) Design of observers for linear systems with unknown inputs. *Automatic Control, IEEE Transactions on,* 37**,** 871-875.

HOU, M. & MULLER, P. C. (1994) Disturbance decoupled observer design: a unified viewpoint. *Automatic Control, IEEE Transactions on,* 39**,** 1338-1341.

HOU, M. & PATTON, R. J. (1998) Optimal filtering for systems with unknown inputs. *Automatic Control, IEEE Transactions on,* 43**,** 445-449.

HUANG, W.-S., LIU, C.-W., HSU, P.-L. & YEH, S.-S. (2010) Precision control and compensation of servomotors and machine tools via the disturbance observer. *Industrial Electronics, IEEE Transactions on,* 57**,** 420-429.

HUTCHINSON, R. G., WICKS, N., EVANS, A. G., FLECK, N. A. & HUTCHINSON, J. W. (2003) Kagome plate structures for actuation. *International Journal of Solids and Structures,* 40**,** 6969-6980.

JOHNSON, C. (1971) Accommodation of external disturbances in linear regulator and servomechanism problems. *Automatic Control, IEEE Transactions on,* 16**,** 635-644.

JOHNSON, C. (1972) Comments on "The output control of linear time-invariant multivariable systems with unmeasurable arbitrary disturbances". *Automatic Control, IEEE Transactions on,* 17**,** 836-838.

KEMPF, C. J. & KOBAYASHI, S. (1999) Disturbance observer and feedforward design for a high-speed direct-drive positioning table. *Control Systems Technology, IEEE Transactions on,* 7**,** 513-526.

KOMADA, S., MACHII, N. & HORI, T. (2000) Control of redundant manipulators considering order of disturbance observer. *Industrial Electronics, IEEE Transactions on,* 47**,** 413-420.

KOTA, S., HETRICK, J., OSBORN, R., PAUL, D., PENDLETON, E., FLICK, P. & TILMANN, C. (2003) Design and application of compliant mechanisms for morphing aircraft structures. San Diego, CA, United states, SPIE.

KUDVA, P., VISWANADHAM, N. & RAMAKRISHNA, A. (1980) Observers for linear systems with unknown inputs. *Automatic Control, IEEE Transactions on,* 25**,** 113-115.

LEE, S.-H., KANG, H. J. & CHUNG, C. C. (2012) Robust fast seek control of a servo track writer using a state space disturbance observer. *Control Systems Technology, IEEE Transactions on,* 20**,** 346-355.

LIU, C.-S. & PENG, H. (2000) Disturbance observer based tracking control. *Journal of Dynamic Systems, Measurement, and Control,* 122**,** 332-335.

LIU, C.-S. & PENG, H. (2002) Inverse-dynamics based state and disturbance observers for linear time-invariant systems. *Journal of Dynamic Systems, Measurement, and Control,* 124**,** 375-381.

LJUNG, L. (1999) *System Identification: Theory for the User,* Upper Saddle River, NJ, Prentice-Hall PTR.

LUCATO, S. L. D. S. E., WANG, J., MAXWELL, P., MCMEEKING, R. M. & EVANS, A. G. (2004) Design and demonstration of a high authority shape morphing structure. *International Journal of Solids and Structures,* vol. 41**,** pp. 3521-3543.

LUENBERGER, D. G. (1964) Observing the state of a linear system. *IEEE Transactions on Military Electronics,* 8**,** 74-80.

MAXWELL, J. C. (1864) On the calculation of the equilibrium and stiffness of frames. *Philosophical Magazine Series 4,* 27**,** 294-299.

MCFARLANE, D. & GLOVER, K. (1988) An H∞ design procedure using robust stabilization of normalized coprime factors. *Decision and Control, 1988., Proceedings of the 27th IEEE Conference on.*

MITSANTISUK, C., OHISHI, K. & KATSURA, S. (2012) Control of interaction force of twin direct-drive motor system using variable wire rope tension with

multisensor integration. *Industrial Electronics, IEEE Transactions on,* 59**,** 498-510.

MOHAMMADZAHERI, M. & CHEN, L. (2010a) Double-command fuzzy control of a nonlinear CSTR. *Korean Journal of Chemical Engineering,* 27**,** 19-31.

MOHAMMADZAHERI, M. & CHEN, L. (2010b) Intelligent predictive control of a model helicopter's yaw angle. *Asian Journal of Control,* 12**,** 667-679.

MOORHOUSE, D., SANDERS, B., SPAKOVSKY, M. V. & BUTT, J. (2006) Benefits and design challenges of adaptive structures for morphing aircraft. *THE AERONAUTICAL JOURNAL***,** 157-162.

OHISHI, K., NAKAO, M., OHNISHI, K. & MIYACHI, K. (1987) Microprocessor-controlled DC motor for load-insensitive position servo system. *Industrial Electronics, IEEE Transactions on,* IE-34**,** 44-49.

OHNISHI, K. (1987) A new servo method in mechatronics. *Trans. Japanese Soc. Elect. Eng.,* 107 D**,** 83-86.

PARK, Y. & STEIN, J. L. (1988) Closed-loop state and input observer for systems with unknown inputs. *International Journal of Control,* 48**,** 1121-1136.

RAMRAKHYANI, D. S., LESIEUTRE, G. A., FRECKER, M. & BHARTI, S. (2005) Aircraft structural morphing using tendon-actuated compliant cellular trusses. *Journal of Aircraft,* vol. 42**,** pp. 1615-1621.

RAO, S. S. (2004) *The Finite Element Method in Engineering* Butterworth-Heinemann.

SCHRIJVER, E. & VAN DIJK, J. (2002) Disturbance observers for rigid mechanical systems: equivalence, stability, and design. *Journal of Dynamic Systems, Measurement, and Control,* 124**,** 539-548.

SCHUHMANN, T., HOFMANN, W. & WERNER, R. (2012) Improving operational performance of active magnetic bearings using kalman filter and state feedback control. *Industrial Electronics, IEEE Transactions on,* 59**,** 821-829.

SHAHRUZ, S. M. (2009) Active vibration suppression in multi-degree-of-freedom systems by disturbance observers. *Journal of Vibration and Control,* 15**,** 1207-1228.

SHE, J.-H., FANG, M., OHYAMA, Y., HASHIMOTO, H. & WU, M. (2008) Improving disturbance-rejection performance based on an equivalent-input-disturbance approach. *Industrial Electronics, IEEE Transactions on,* 55**,** 380-389.

SHE, J.-H., OHYAMA, Y. & NAKANO, M. (2005) A new approach to the estimation and rejection of disturbances in servo systems. *Control Systems Technology, IEEE Transactions on,* 13**,** 378-385.

SHE, J.-H., XIN, X. & PAN, Y. (2011) Equivalent-input-disturbance approach — analysis and application to disturbance rejection in dual-stage feed drive control system. *Mechatronics, IEEE/ASME Transactions on,* 16**,** 330-340.

SOFLA, A. Y. N., ELZEY, D. M. & WADLEY, H. N. G. (2009) Shape morphing hinged truss structures. *Smart Materials and Structures,* vol. 18**,** 8.

SPILLMAN, J. J. (1992) The use of variable camber to reduce drag, weight and costs of transport aircraft. *AERONAUTICAL J.,* 96**,** 1-9.

SUN, B. & GAO, Z. (2005) A DSP-based active disturbance rejection control design for a 1-kW H-bridge DC-DC power converter. *Industrial Electronics, IEEE Transactions on,* 52**,** 1271-1277.

TAN, K. K., LEE, T. H., DOU, H. F., CHIN, S. J. & ZHAO, S. (2003) Precision motion control with disturbance observer for pulsewidth-modulated-driven permanent-magnet linear motors. *Magnetics, IEEE Transactions on,* 39**,** 1813-1818.

THILL, C., ETCHES, J., BOND, I., POTTER, K. & WEAVER, P. (2008) Morphing skins. *Aeronautical Journal,* 112**,** 117-139.

UMENO, T. & HORI, Y. (1991) Robust speed control of DC servomotors using modern two degrees-of-freedom controller design. *Industrial Electronics, IEEE Transactions on,* 38**,** 363-368.

UMENO, T., KANEKO, T. & HORI, Y. (1993) Robust servosystem design with two degrees of freedom and its application to novel motion control of robot manipulators. *Industrial Electronics, IEEE Transactions on,* 40**,** 473-485.

VALENZUELA, M. A., BENTLEY, J. M., AGUILERA, P. C. & LORENZ, R. D. (2007) Improved coordinated response and disturbance rejection in the critical sections of paper machines. *Industry Applications, IEEE Transactions on,* 43**,** 857-869.

VIDYASAGAR, M. (1978) *Nonlinear Systems Analysis,* Englewood Cliffs, Prentice Hall.

WANG, S. H., DAVISON, E. J. & DORATO, P. (1975) Observing the states of systems with unmeasurable disturbances. *Automatic Control, IEEE Transactions on,* 20**,** 716-717.

WHITE, M. T., TOMIZUKA, M. & SMITH, C. (2000) Improved track following in magnetic disk drives using a disturbance observer. *Mechatronics, IEEE/ASME Transactions on,* 5**,** 3-11.

WRIGGERS, P. (2008) *Nonlinear Finite Element Methods*, Springer Berlin Heidelberg.

XIONG, Y. & SAIF, M. (2003) Unknown disturbance inputs estimation based on a state functional observer design. *Automatica,* 39**,** 1389-1398.

YANG, F. & WILDE, R. W. (1988) Observers for linear systems with unknown inputs. *Automatic Control, IEEE Transactions on,* 33**,** 677-681.